uOttawa

L'Université canadienne
Canada's university

FACULTÉ DES ÉTUDES SUPÉRIEURES ET POSTOCTORALES

u Ottawa

L'Université canadienne
Canada's university

FACULTY OF GRADUATE AND POSDOCTORAL STUDIES

Janet Gaskin

AUTEUR DE LA THÈSE / AUTHOR OF THESIS

M.A.Sc. (Civil Engineering)

GRADE / DEGREE

Department of Civil Engineering

FACULTÉ, ÉCOLE, DÉPARTEMENT / FACULTY, SCHOOL, DEPARTMENT

Intensive aDcp Survey of a Gravel-Bed River Confluence

TITRE DE LA THÈSE / TITLE OF THESIS

Colin Rennie

DIRECTEUR (DIRECTRICE) DE LA THÈSE / THESIS SUPERVISOR

CO-DIRECTEUR (CO-DIRECTRICE) DE LA THÈSE / THESIS CO-SUPERVISOR

Ousmane Seidou

Majid Mohammadian

Paul Van Geel

Gary W. Slater

Le Doyen de la Faculté des études supérieures et postdoctorales / Dean of the Faculty of Graduate and Postdoctoral Studies

Intensive aDcp Survey of a Gravel-Bed River Confluence

Janet Gaskin

Thesis submitted to the
Faculty of Graduate and Postdoctoral Studies
in partial fulfillment of the requirements
for the MASc degree in Civil Engineering

The Ottawa-Carleton Institute for Civil Engineering
Department of Civil Engineering
Faculty of Engineering
University of Ottawa

Janet Gaskin, Ottawa, Canada, August, 2010

Your file Votre référence
ISBN: 978-0-494-73818-4
Our file Notre référence
ISBN: 978-0-494-73818-4

Table of Contents

List of Figures

List of Tables

Abstract

An intensive survey of the high angle asymmetric gravel-bed confluence of the Fraser River Main Channel with Minto Side Channel, downstream of a mid-channel island, was conducted using an acoustic Doppler current profiler (aDcp) during the freshet in June, 2008 at a combined discharge of 7 500 m^3/s. The confluence was characterized by a vertical mixing interface, with the Minto high velocity core being advected downwards in the upstream part of the scour zone; weaker helical flow is evident in the main channel flow as it confines the strongly helical left bank flow. Apparent bed velocity generally followed the thalweg, with the highest values near 0.15 m/s occurring at the edges of the scour zone and along the elongated bed step. In plotted spatial distributions, the areas of high primary bed velocity matched areas of high shear velocity and/or strongly upward vertical flow velocity.

Objectives

The objective of this study is to analyse the flow and sediment dynamics at the confluence of the main Fraser River channel and Minto side channel, near Chilliwack, BC, Canada, where deep scour and rapid bank recession has occurred. The spring freshet was selected as the period of measurement, as it is the annual period of highest bed and bank mobility.

Flow patterns will be characterized from measured flow velocities, and the shear forces applied by these patterns will be investigated. Downstream, cross-stream, and vertical flow velocities will be examined at progressive cross-sections in the downstream direction to evaluate the complex secondary flow patterns, mixing layer position, and scour zone through the confluence. Apparent bed velocity will be used as a measure of bed-load sediment transport and compared to the shear forces applied by the flow patterns. Bed morphology is determined from measured flow depths, and the characteristic bed surface particle size patterns will be assessed using the bed roughness estimates calculated along with shear velocity from the measured vertical profiles of streamwise velocity.

This study of the confluence of the Fraser River main channel with Minto side channel, is the first study of a large gravel-bed river confluence at channel forming flow. The study of confluences of large rivers at high discharges has only recently been made possible by moving boat aDcp measurement, and those published have been of sand-bed confluences along the Parana River, in Argentina. This study is also the first to map apparent bed velocity, a rapid non-intrusive measure of the bed-load transport, in order to better understand the morphodynamics of the confluence.

The introduction presents a literature review of confluence studies and a review of acoustic measurement theory and recent studies. The methodology of this field study is outlined and the Fraser River confluence site near Chilliwack, BC, is described. The

flow dynamics are presented at successive downstream cross-sections in the interpolated flow volume. Maps of interpolated apparent bed velocity, shear velocity, near-bed vertical velocity and bathymetry are examined to identify the interactions of flow, sediment transport and bed morphology. The discussion includes an investigation into different methods of applying the log-law to the vertical velocity profiles to calculate shear velocity, estimates of D84 through the reach, and the deep scour hole and bank erosion along the left bank of the confluence. The conclusions present the key features of this large gravel-bed confluence at channel forming flow and similarities/differences to other large river confluence studies.

Introduction

Confluence Review

Confluence Basics

River confluences adjust to convey the mixing flows and sediment loads. They have been described through measurement of the interdependent flow velocities, sediment transport, and bed morphology. These interactions depend on the momentum ratio of the mixing flows, differences in their densities and temperatures, and the confluence angle, topography and bed materials.

Improved understanding of river confluence adjustments is very important for engineers. Changes in bed morphology and sediment transport patterns through a confluence area can adversely affect channel depth for shipping lanes, and integrity of structures such as bridge piers and underground pipelines. Bank stability is also of concern for the conservation of riverfront property and structures. Changes in channel flow conveyance and bank stability are important for assessing the extent of potential flooding. River confluence morphodynamics also affect the downstream reach, with complete flow mixing occurring at a distance downstream ranging from that equal to several channel widths to over a hundred channel widths. Habitat for fish and wildlife depends on water depth, sediment size distribution, and flow velocities. Engineers are often required to consider integrated river management plans that include fish and wildlife habitat assessment.

The first confluence study was conducted in the laboratory by Mosley (1976) for comparable tributary and main channel flows at a symmetric concordant bed confluence in cohesive sediment. The classic features reported were a central scour hole, with avalanche faces at the upstream end of the shear layer, a vertical mixing layer with flows forming back-to-back helical cells, a stagnation zone at the apex, and one or two downstream bars where the flow diverges. A sketch of a symmetric

confluence is shown in figure 1, with the flow pattern shown in the photo in figure 2. Ashmore and Parker (1983) conducted laboratory tests of confluence scour at braid anabranches in non-cohesive sediment, for both a well-sorted and poorly sorted sand, and a field study of braided gravel bed anabranch confluences in the Sunwapta river, in Alberta. Asymmetric confluences are characterised by an offset mixing layer and scour hole. A sketch of an asymmetric confluence is shown in figure 3, and the offset mixing layer is clearly visible in the photo of an anabranch confluence in the Sunwapta River in figure 4. Scour depth was found to correlate most strongly with the confluence angle, and to a lesser extent with the momentum ratio (see equation 1), as long as the momentum of the main channel is not more than twice that of the tributary. The maximum scour depth was found to be nearly six times the channel depth.

Momentum ratio is defined as the momentum, ρQv, of the tributary to the main channel:

$$M_r = \rho_t Q_t v_t / \rho_m Q_m v_m \quad , \tag{1}$$

where t-tributary, m-main channel, ρ-density, Q-flowrate, v-velocity.

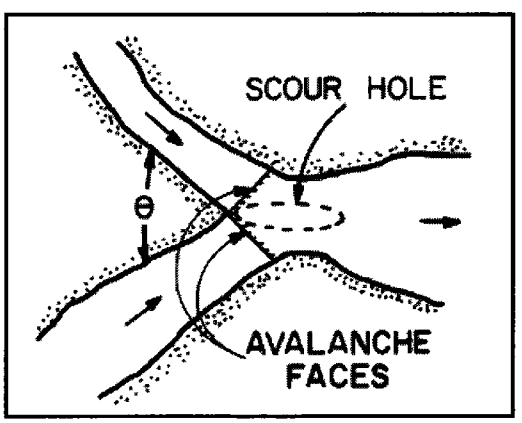

Figure 1 – Symmetric Confluence
(Ashmore & Parker, 1983)

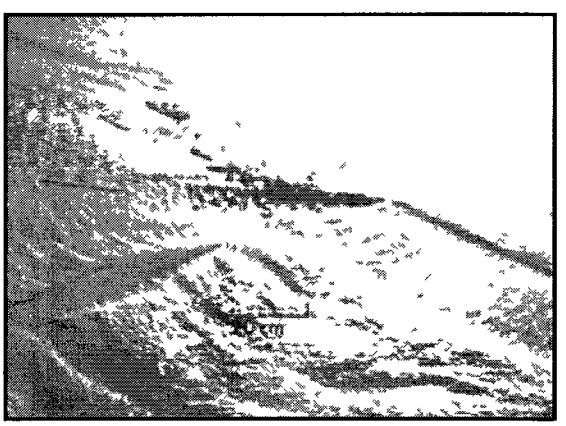

Figure 2 – Symmetric Confluence Flow
(Ashmore & Parker, 1983)

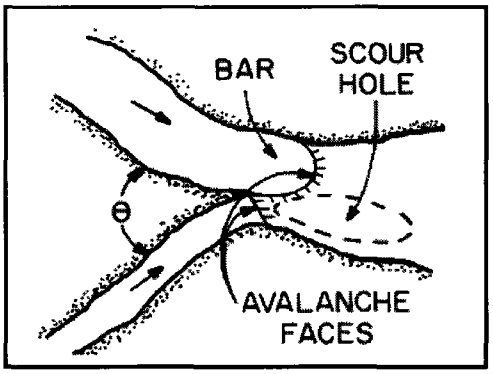

Figure 3 - Asymmetric Confluence (Ashmore & Parker, 1983)

Figure 4 - Asymmetric Anabranch Confluence (Ashmore & Parker, 1983)

Best and Reid (1984) performed flume experiments to document changes in scour hole dimensions with changing confluence angle. Scour hole length and width were both found to increase with increasing confluence angle, accompanied by flow acceleration through the confluence and separation of flow from the bank. From flume and field studies, Best (1988) observed that an increase in momentum ratio and confluence angle resulted in the segregation of the sediment loads entering the confluence, associated with a retreat of the main channel avalanche face, an increase in scour depth and in the downstream bar.

Natural confluences tend to adjust to minimize confluence angles, in the absence of topographic forcing such as bedrock outcrops, where flow mixing occurs much more slowly. A shallow scour hole resulting from the acceleration of flow through the confluence was documented by Roy et al (1988) and Roy & Bergeron (1990) for a low angle confluence for a gravel bed river, and by Bridge & Gabel (1992) for a sand bed river. The potential complexity of the flow field at confluences has been revealed through studies of asymmetric field sites, both for concordant and discordant beds.

During particular flow conditions, complete helical flow cells have been identified for concordant bed confluences. No complete helical flow cells have been identified at discordant bed confluences, where mixing tends to occur due to a tilted mixing layer. Large river confluences, with high width to depth ratios, have been characterized by partial helical cells limited to the flow above the scour zone in both cross-stream and downstream extent. The development of turbulent structures generated from the shear layer at the upstream end of the mixing layer was found to promote mixing only over a distance of less than half a channel width in the downstream direction, due to rapid dissipation (de Serres et al, 1999, Boyer et al, 2006, Sukholodov and Rhoads, 2001, Rhoads and Sukholodov, 2004, and Lane et al, 2008). Numerical modelling of the complex geometries of natural confluences has not been possible. These studies are discussed in detail in the following sections.

Secondary Circulation Definition

Secondary circulation, or the existence of helical cells, at confluences has been examined according to three definitions of the downstream direction: Rozovskii, zero net cross-stream discharge, and zero net downstream discharge (figure 5). The downstream direction for the Rozovskii method is determined as the direction of the depth averaged velocity vector at each vertical in the flow. As a result, the direction of downstream flow can vary across the section and there is no accounting for any acceleration through the confluence. The zero net cross-stream discharge definition involves rotating the section until the net cross-stream discharge for that section is zero. The zero downstream discharge definition involves rotating the sections until the downstream discharges of the two sections are equal. The definition of zero net cross-stream and downstream discharge does account for flow acceleration but ignores the separation of the flow by the mixing layer into two cells, each of which could contain helical flow. It has been suggested that this drawback could be solved by applying the definition to each section of channel, but unless temperature or

turbidity was found to be different in each tributary it would be difficult to determine the location of the mixing layer. The difference in downstream velocities dissipates much faster than the mixing layer, and differences in turbulence can only identify the upstream section or shear layer. The Rozovskii definition is the only method suitable for scarce data.

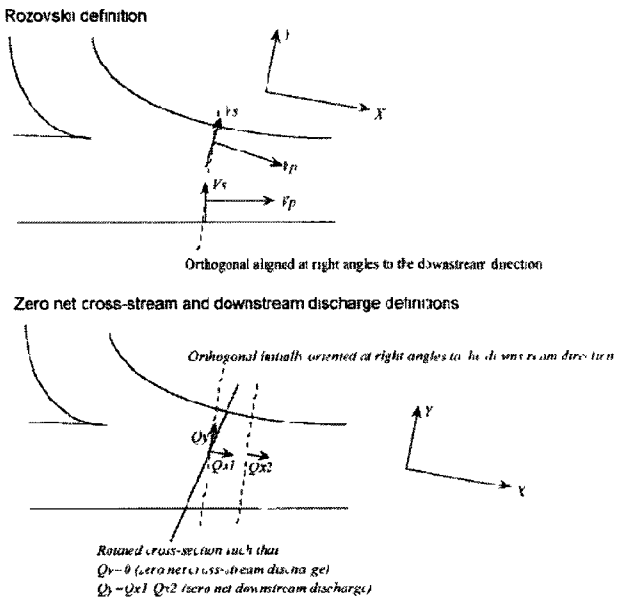

Figure 5 – Definitions of downstream direction determining secondary circulation (Lane et al, 2000)

The definition of secondary flow according to Rozovskii was derived from the study of the development of a single helical flow cell through a meander bend. It is based on a 2D analysis of the flow in the downstream and cross-stream directions. Simplified flow descriptions were necessary because flow could, until recently, only be measured simultaneously in 2D, generally in the downstream and cross-stream directions with an electromagnetic current meter (ECM), and at a limited number of locations. The

vertical velocities characteristic of helical flow were not measured directly, but inferred from the patterns of cross-stream direction at successive cross-sections. Determination of the downstream direction is straightforward for a single channel, but cannot be consistent through a confluence. The cross-stream direction is defined as that perpendicular to the downstream direction. The existence of helical flow is defined as being a consistent pattern through successive cross-sections in addition to across a particular cross-section, and so the directions of the downstream and cross-stream flow for the post-confluence channel have been extended upstream through the confluence area. The cross-stream direction is therefore not perpendicular to the local flow path in the channels entering the confluence. The definition of flow skew, as the difference in angle between the local flow path and the downstream direction defined according to the post-confluence flow, allowed the distinction of cross-stream flow resulting from flow skew and actual helical motion. Identification of helical flow should be relatively straightforward where spatial distributions can be mapped from measurement of 3D velocities.

The Rozovskii definition is based on the assumption of zero lateral discharge at each vertical in the cross-section. The local downstream direction is defined as that of the depth-averaged velocity vector. Where the velocity vector at a specific depth is at a different angle to the depth-averaged vector, it can be separated into a component in the primary (local downstream) direction and a component in the secondary (local cross-stream) direction, given in equations (2) and (3). In order to relate the local primary and secondary velocities back to the overall confluence downstream and cross-stream directions, the primary and secondary velocities can be further separated into their downstream and cross-stream components, given in equations (4) and (5). Please refer to figure 6.

Depth-averaged Local velocity at a specific depth

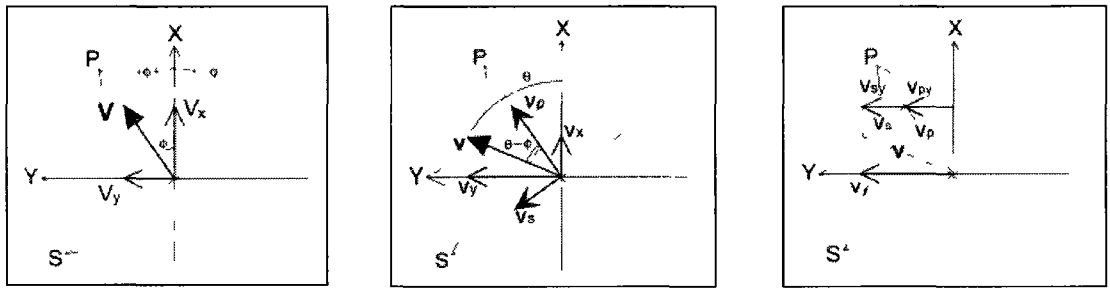

$$v_p = v\cos(\theta - \varphi) \quad (2) \qquad v_{py} = v_p \sin\varphi \quad (4)$$

$$v_s = v\sin(\theta - \varphi) \quad (3) \qquad v_{sy} = v_s \cos\varphi \quad (5)$$

Figure 6 – Secondary Flow: Rozovskii definition

(Rhoads and Kenworthy, 1998)

Asymmetrical Confluences with Helical Flow

Helical flow cells have been identified at high angle asymmetric confluences with concordant bed heights where the mixing layer is vertical. Two cores of high velocity fluid from the channels entering the confluences are initially separated by a region of slower-moving or recirculating flow. When the high velocity cores converge, fluid is advected strongly downwards towards the scour zone and the difference in streamwise velocity between the two dissipates. These secondary currents result in rapid mixing of the flows entering the confluence. Curvature in either the entry or in the post-confluence channel, or in the entering flow due to deflection around a confluence entry bar when the flow stage is below bankfull, can enhance any secondary flow patterns that develop.

Helical cells were first traced using dye in the laboratory (Mosley, 1976), and were most developed for high confluence angles. In a field study of braided gravel bed anabranch confluences in the Sunwapta river, ripples in abruptly abandoned scour holes were observed at various angles, some approaching perpendicular, to the downstream flow direction (Ashmore and Parker, 1983). The most intensive examination of the existence of helical flow cells was conducted for the Kaskaskia River-Copper Slough confluence, in Illinois, by Rhoads and Kenworthy (1995 & 1998) and Rhoads and Sukhodolov (2001). Flow in the downstream (sections A to E) and central portions of the confluence (sections A3-A) were analysed using 2D ECMs, in 1995 and 1998 respectively (figure 7). In 2001, flow in both portions at this confluence and two nearby confluences were analysed using 3D ADVs. Kaskaskia River has a sand bed, while Copper Slough has a fine gravel bed, and they meet at a confluence angle of 60°. The momentum ratio of the flows entering the confluence varied widely, because the catchment area for the Copper Slough is urban and therefore flashier in response to precipitation than the agricultural catchment area for Kaskaskia River. The flowrate was about 1.5 m^3/s and the velocities ranged between 0.3-0.5 m/s.

Flow velocities for three events were measured by Rhoads and Kenworthy in 1995, with momentum ratios of 3.64, 3.47 and 0.55, with no changes in bed morphology. Depth averaged velocity showed a consistent pattern of flow convergence and acceleration just downstream of the confluence (sections A-B), separation of flow from the inner bank (sections B-C), and divergence as the flow leaves the confluence region (sections C-E). The existence of a large entry bar on the Copper Slough side of the confluence influenced the flow pattern strongly at lower stages. The first two events were characterized by a single core of high velocity fluid entering the confluence from Copper Slough, whereas for the third event, two cores of high velocity entered, one from each channel. Cross-stream velocities, separated into their primary and secondary components, showed the existence of secondary circulation for all three events. For the first two events, a strong counterclockwise cell developed in the Copper Slough flow and dominated the downstream confluence, pushing the

mixing layer towards the Kaskaskia River side of the confluence. For the third event, weak back-to-back helical cells existed on both sides of the centrally located mixing layer.

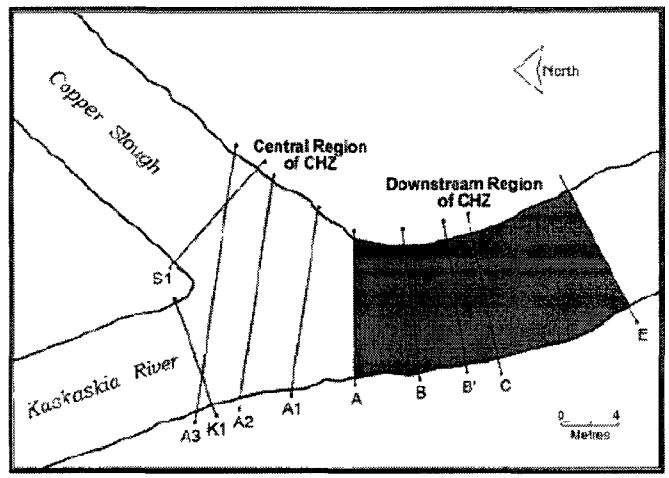

Figure 7 – Kaskaskia River-Copper Slough Confluence

(Rhoads and Kenworthy, 1998)

In 1998, Rhoads and Kenworthy focussed their study of the central section of the confluence, just downstream from the junction apex (see figure 7). Flow velocities were measured with ECMs for three events, with momentum ratios of 0.64, 1.43 and 3.18. Using measurements of water temperature, the mixing layer was determined to be vertical. Depth averaged velocity vectors showed the existence of a stagnation zone at the apex of the junction (section A3), with convergence of flows strongest at the upstream end of the confluence and decreasing as the flows deflected off each other. The degree of flow deflection and the position of the mixing layer depended on the momentum ratio and the bed morphology. Plots of downstream velocity showed very different flow patterns for the three events. The two cores of high velocity stayed separate through the central confluence zone for both the first and second event, but the Kaskaskia River flow was subsumed by the dominant Copper Slough flow in the

third event, yielding a single high velocity core. The dominant flow also extended into the scour hole for each event. Plots of cross-stream velocities, v_y, v_{py} and v_{sy}, showed that for all three events, v_y consisted mostly of v_{py} and therefore most of the cross-stream velocities resulted from the convergence of the skewed flows. However, significant secondary velocities in the cross-stream direction did exist, with the magnitude of v_{sy} sometimes equalling that of v_{py}. Secondary velocity in the cross-stream direction was shown to be directed towards the mixing layer at the surface and away from the mixing layer at the bed at specific verticals, initially only near the mixing layer and extending further towards the bank with distance downstream. Similar patterns over depth at adjacent verticals and in subsequent cross-sections downstream were evidence of coherent helical cells. For the first event, with momentum ratio of 0.64, back to back helical cells started to develop at section A2 and persisted through the central confluence. For the second event, with momentum ratio of 1.43, a single helical cell on the dominant Copper Slough side developed. For the third event, with momentum ratio of 3.18, back to back helical cells started to develop at section A2 but resolved into a single helical cell on the dominant Copper Slough side of the confluence by section A. These results are consistent with those from 1995, which only showed development of a single helical cell on the dominant side for momentum ratios over one for this confluence. Plots of depth averaged velocity, downstream velocity and cross-stream velocity for the first event, with momentum ratio of 0.64 occurring on June 7th, are shown in figures 8, 9, and 10 respectively.

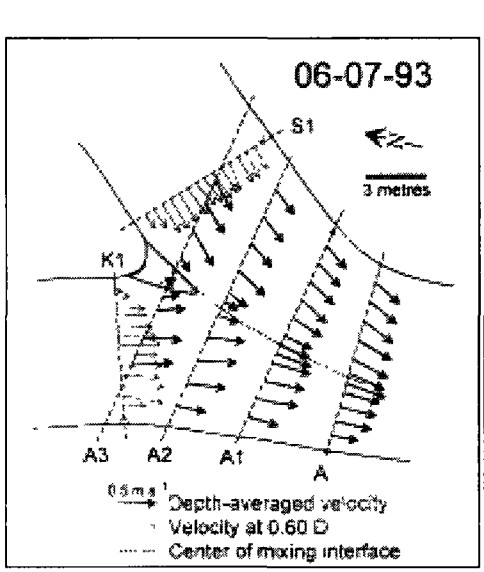

Figure 8 – Depth Averaged Velocity

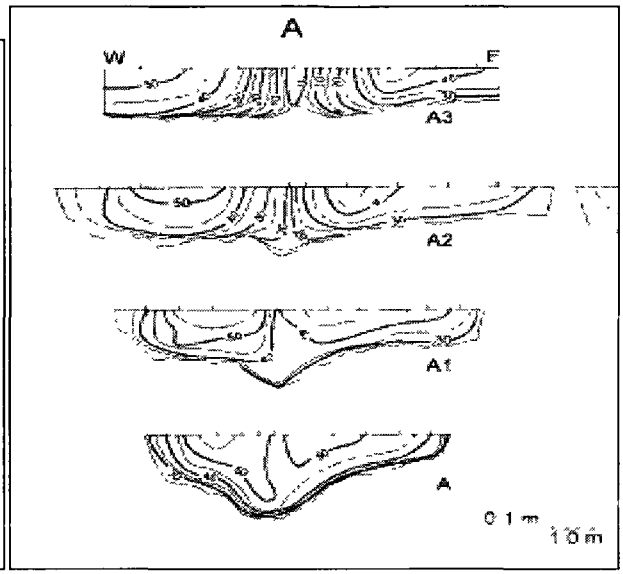

Figure 9 – Downstream Velocity

(06/06/93, Mr=0.64, Rhoads and Kenworthy, 1998)

Further study of secondary circulation was conducted by Rhoads and Sukholodov in 2001, at this asymmetric confluence and two nearby symmetric concordant bed confluences, with momentum ratios of 1, 1, and 0.35 respectively. Temperature measurements showed that the mixing layer at all three locations was vertical at the beginning of the confluence area, and remained vertical through the two symmetric confluences, showing that little thermal mixing was occurring. Three dimensional flow velocities were recorded using ADVs, and an alternate method of documenting helical flow was introduced using the angles between the streamwise and cross-stream, θ_{xy}, and streamwise and vertical directions, θ_{xz} (see equations 6 and 7):

$$\theta_{xy}=\tan^{-1}(v/u) \qquad (6)$$

$$\theta_{xz}=\tan^{-1}(w/u) \qquad (7)$$

{with u-streamwise velocity, v-cross-stream velocity, and w-vertical velocity}

The standard confluence features of stagnation at the apex, and flow convergence and deflection were observed at all three confluences. Significant helical motion was only detected at the asymmetric confluence (see figure 11), associated with downwelling of fluid over the scour hole and upwelling along the outer flanks of the cells. The tributary cell extended and subsumed the main channel cell through the downstream confluence zone, with distortion of the mixing layer, resulting in a single helical cell. One of the symmetric confluences had a high confluence angle, and the lack of helical flow may have resulted from the bank irregularities that impeded formation of any coherent flow patterns.

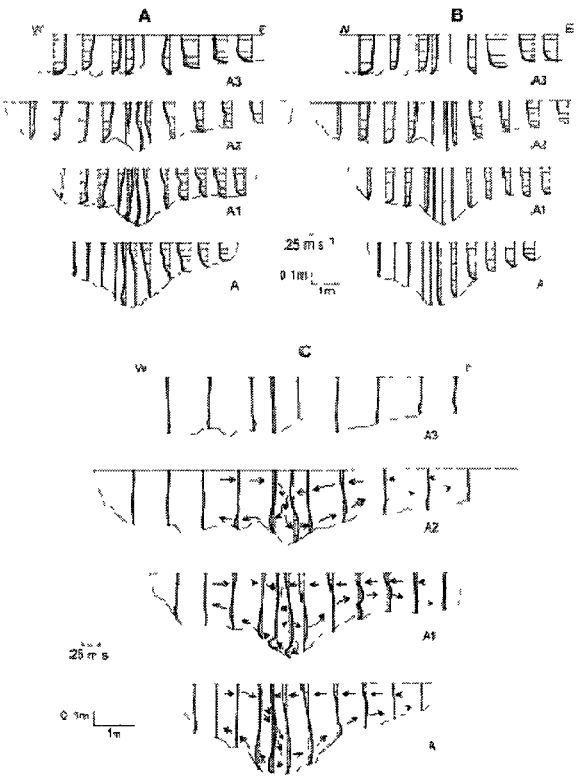

Figure 9 (A) Cross-stream velocities (v_n), (B) cross-stream component of primary velocities (v_{py}) and (C) cross-stream component of secondary velocities (v_{sy}) and patterns of secondary circulation (marked by arrows – see text for details). 7 June 1993 Horizontal lines at each vertical indicate the magnitude of the velocity component at measurement positions in the flow column

Figure 10 – Cross-stream Velocities

(06/06/93, Mr=0.64, Rhoads and Kenworthy, 1998)

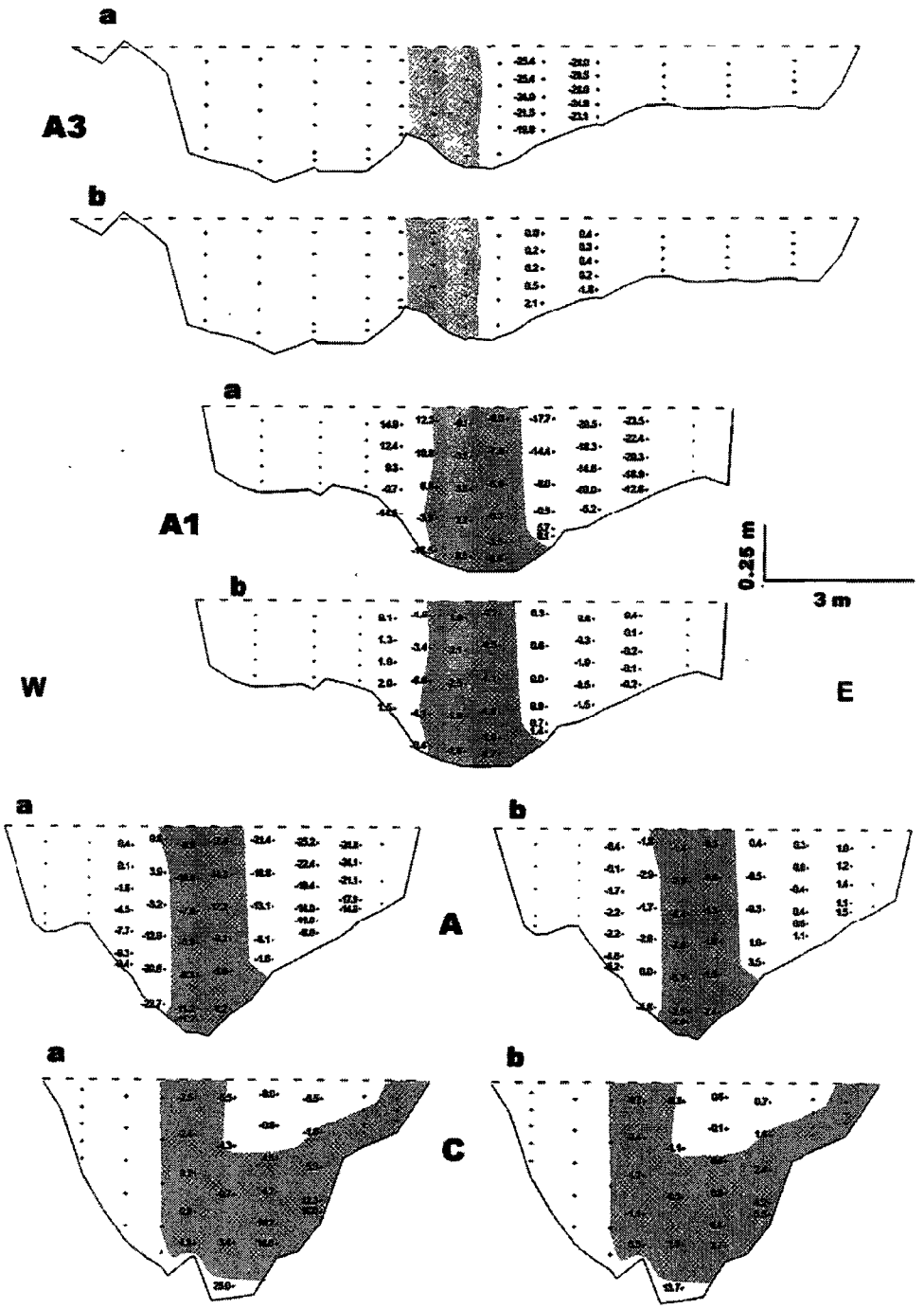

Figure 11 – Velocity vector angles for helicity at Kaskaskia River-Copper Slough

a)horizontal angles, b)vertical angles, (shaded areas indicate mixing interface)

(Rhoads and Sukholodov, 2001)

Asymmetrical Confluences with Discordant Bed Heights

The first studies of discordant bed confluences were performed in laboratory flumes by Best and Roy (1991) and Biron et al (1996 a). Field studies of asymmetric high angle discordant bed confluences have focussed on measurements at the Berthier-Bayonne confluence, in Quebec (Biron et al, 1993, de Serres et al, 1999, Biron et al, 2002, and Boyer et al, 2006), and confluences along the Parana River, in Argentina (Lane et al, 2008, Szupiany et al, 2009). The Berthier/Bayonne confluence is a small sand bed confluence, with flowrates less than 5 m^3/s and velocities of 15 to 48 cm/s. At the Berthier-Bayonne confluence (see figure 12), the tributary bed has the higher bed height, and a single avalanche face formed at a shallow scour hole, where the flow velocities and bed shear are found to be highest; the avalanche face at the bed discordance lead to flow separation, and subsequent downwelling of fluid over the scour hole. Erosion of the upstream tributary bar has been found to be more extensive when Mr<1 (Boyer et al, 2006).

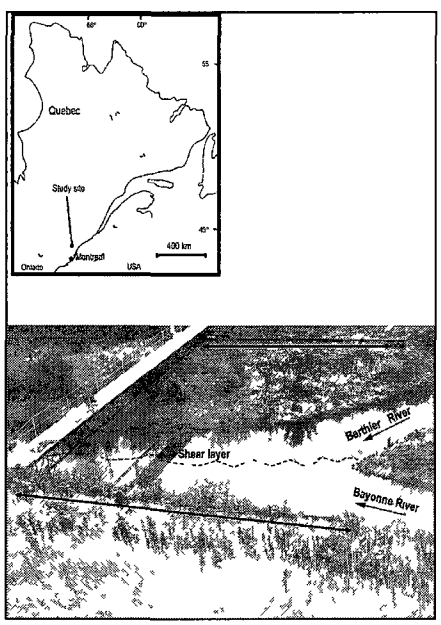

Figure 12 – Berthier-Bayonne Confluence

(Boyer et al, 2006)

Two studies of the Berthier-Bayonne confluence examined the common features present through various flow stages as evidenced by bed morphology and sediment size (Biron et al, 1993) and water surface elevations (Biron et al, 2002). An elevated water surface and finer sediment characterized the area of flow stagnation at the apex of the confluence. The mixing layer was also characterized by an elevated water surface, the edge of which exhibited a lateral tilt at this discordant confluence. The location of the mixing layer varied with the momentum ratio, and was consistent with the measured bed feature variations. The tributary mouth bar was eroded and the position of the avalanche face retreated at lower flow momentum ratios, and the area of maximum depth (no marked scour zone at this confluence) was characterized by coarser particles. A third area with a periodic elevated water surface was at the downstream junction corner on the tributary side, where the sediment deposited was also finer than average. No zone of flow separation was observed in the downstream confluence zone at this discordant bed site. These bed morphology and sediment features were also observed at two nearby similar confluences.

Mean flow velocity patterns at several flow stages and momentum ratios for a discordant bed confluence, where the tributary channel has the higher bed elevation, were examined at the Berthier-Bayonne confluence by de Serres et al (1999) and Boyer et al (2006). Velocity measurements taken at several depths for each vertical in a cross-section were analyzed in the first study, while in the second, the flow measurements taken closest to the bed were compared to physical bed-load samples. Flow velocity was measured using ECMs and bed-load using a modified Helley-Smith sampler. A stagnation zone existed at the apex of the junction. The upstream end of the mixing layer was characterized by lower mean velocity fluid with strong upwelling, in between the two cores of high velocity, accelerating, and moderately downwelling fluid entering the confluence (see figures 13 and 14). The mixing layer at this discordant bed confluence was determined to be tilted, with flow deflection highest in the tributary flow and the upwelling of fluid strongest in the mixing layer after the flow passed over the tributary avalanche face (see figures 14 and 15). Some

flow deflection, shown by the difference in direction between the surface and bed flow, was observed in the tributary flow in the confluence, and to a much lesser degree prior to entering the confluence. Flow velocities decreased at the downstream junction bar though no horizontal flow separation was observed. The tributary mouth bar was found to extend further into the confluence when the momentum ratio was larger than one, with the shear layer located closer to the main channel side of the confluence and a narrower and elongated zone of maximum depth. When the momentum ratio was smaller than one, the tributary mouth bar retreated, the shear layer was in the centre of the confluence and the zone of maximum depth was shorter and wider. The highest measured bed-load transport rates were found to be located further downstream in the confluence zone when momentum ratio was larger than one, which was consistent with the changes in bed morphology, and were largest at the edges of the mixing layer (see figure 16).

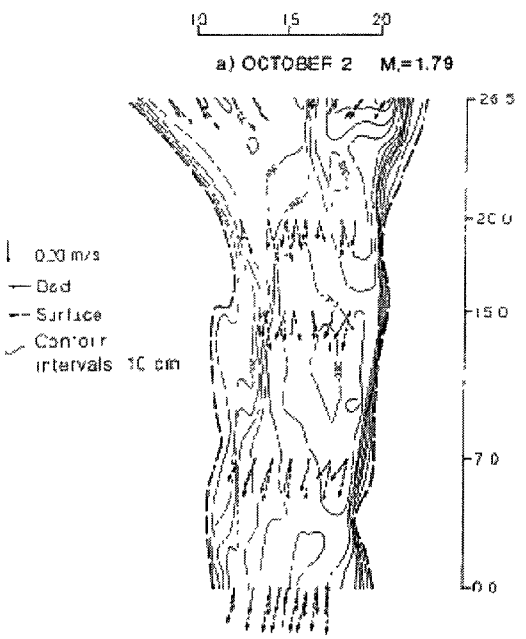

Figure 13 – Mean horizontal velocity vectors at bed and surface (Mr=1.79, de Serres, 1999)

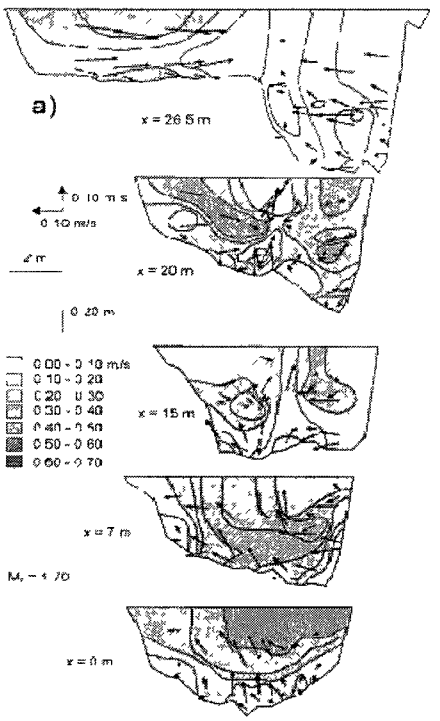

Figure 14 – Mean streamwise velocity contours with 2D vel. vectors at X-sections (Mr=1.79, de Serres, 1999)

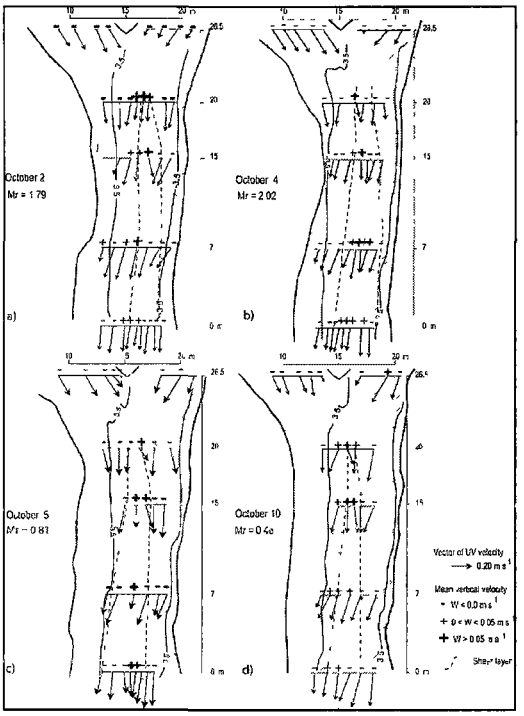

Figure 15 – Mean horizontal vel.(arrows) and vertical vel.(+/-) at cross-sections
(4 events, Boyer et al, 2006)

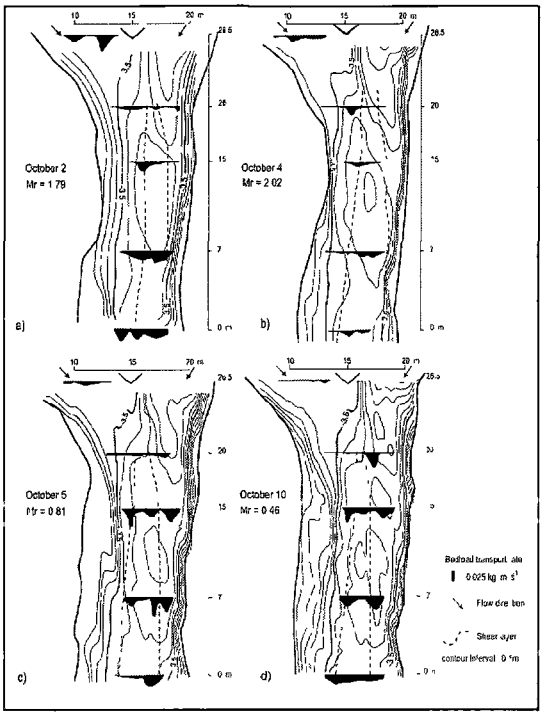

Figure 16 – Bed-load transport rates at cross-sections
(4 events, Boyer et al, 2006)

Large Rivers with Asymmetric Confluences

The high angle asymmetric confluences along the Parana River include both discordant bed, at the confluence of the Parana/Paraguay Rivers (Lane et al, 2008) and confluence A downstream of a mid-channel island (Szupiany et al, 2009), and concordant bed, confluence B downstream of a mid-channel island (Szupiany et al, 2009). The large Parana confluences have sand beds, with flowrates of 1200 to 1500 m/s and velocities up to 1.5 m/s. At the Parana-Paraguay confluence (see figure 17), the main channel has the higher bed height, and instead of a typical avalanche face there was a steep elongated bed step. Two confluences downstream of mid-channel islands along the Parana River were examined by Szupiany et al (2009), one having

similar channel depths upstream but a deep scour hole along the tributary side of the confluence, and the other having a deeper main channel with shallower scour at the confluence. Vertical flow mixing resulting from a tilted mixing layer has been observed in the laboratory by Best and Roy (1991) and at the Parana/Paraguay confluence by Lane et al (2008), with flow from the deeper channel having moved under the flow from the shallower channel but not forming a complete helical flow pattern. Incomplete helical flow, limited to the flow adjacent to the mixing layer, was also identified at the high angle confluences downstream of mid-channel islands along the Parana River (Szupiany et al, 2009). A low angle confluence-diffluence downstream of a mid-channel island along the Parana River was investigated by Parsons et al (2007) and found to have a weak secondary flow pattern at the confluence, with flow moving towards the left bank at the surface and towards the right bank at the bed.

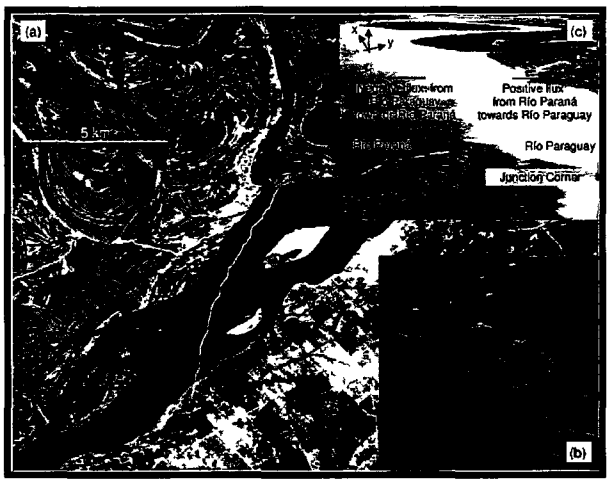

Figure 17 – Parana-Paraguay Confluence

Figure 18 – Parana/Paraguay morphology (Lane et al, 2008)

Mean flow velocity patterns were examined at the discordant bed Parana-Paraguay confluence, where the tributary channel has the lower bed elevation (see figures 17 and 18), for two different flow events by Lane et al (2008). Rapid mixing of flows in

the confluence occurred during the first event, with a momentum ratio of 0.56, while only very slow mixing occurred during the second event, with a momentum ratio of 0.28. (The momentum ratio presented by Lane et al (2008) was defined as that of the main channel to the tributary, which is the opposite of the standard definition, and to maintain consistency the values reported here are those of the classic definition). The position of the mixing layer was clearly visible due to the contrast between the turbid Paraguay flow and the clear Parana flow (see figure 17). During the first flow event, the tributary flow had enough momentum for the near bed flow to move up and over the bed step towards the Parana side of the confluence, while the shallower Parana flow moved towards the Paraguay side of the confluence near the surface (see figure 19). The resulting tilted mixing layer allowed rapid mixing of flows due to a partial channel-scale circulation pattern, which was not considered a true helical cell because it was not fully developed. During the second event, the Paraguay flow had less momentum and was constrained by the bed topography (see figure 18). The mixing layer remained vertical, and the two flows mixed very slowly. Flow mixing was complete after a distance downstream of 3.3 channel widths with the rapid mixing of the first event, but only after a distance downstream of 128 channel widths with the slow mixing of the second event.

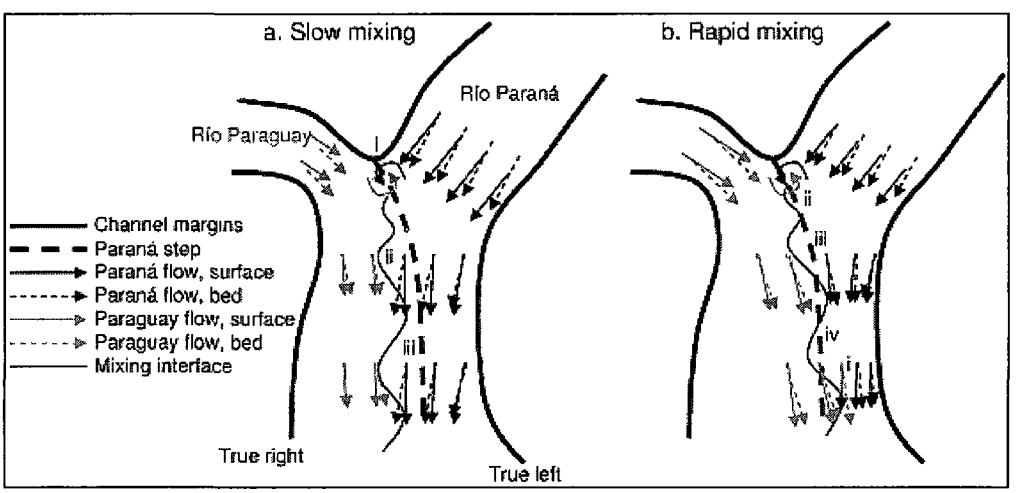

Figure 19 – Flow velocities at surface and bed through Parana/Paraguay confluence

(Lane et al, 2008)

The morphologies of the two sand bed confluences downstream of mid-channel islands along the Parana River studied by Szupiany et al (2009) are shown in figure 20. The confluence angles were 77° and 70° for A and B respectively, and the corresponding momentum ratios were 0.15 and 0.43, with total flow discharge about 15 000 m/s for both. The confluence scour for B is extensive and reaches a depth of 23 m, while that for A, where the main channel thalweg stays near the right bank and away from the mixing interface, is smaller with a maximum depth of 15 m.

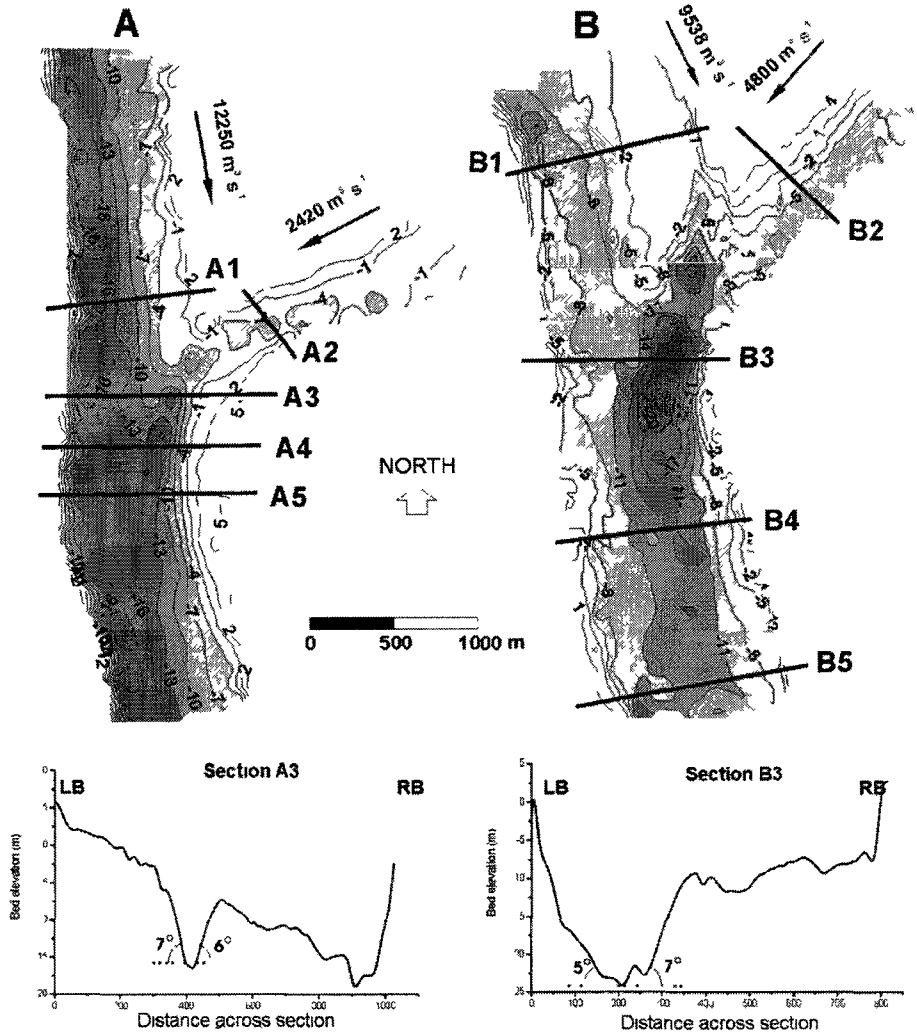

Figure 20 – Morphology of Mid-Channel Parana Confluences
(Szupiany et al, 2009)

Downstream and cross-stream velocity components were calculated according to the Rozovskii method for confluences A and B (Szupiany et al, 2009). The plots of primary velocity, with secondary velocity superimposed, for confluences A and B are shown in figure 21.

Scour is limited in confluence A because the main channel thalweg stays next to the right bank (section A1), and away from the mixing interface (section A3), and the tributary flow is not accelerating through the confluence area. The scour is much deeper and extended in the downstream direction in confluence B (figure 20); both high velocity cores entering the confluence meet at the mixing interface and the tributary flow is accelerated through the confluence, being confined against the left bank by the main channel flow (section B3). Weak, back to back, counter-rotating secondary flow cells exist on both sides of a vertical mixing interface at both confluences, being spatially limited to about one fifth of the cross-section for A and about one third for B (sections A3 and B3). The secondary cells dissipate in the downstream direction, with a single cell existing for the merged high velocity cores for B (sections B4 and B5) and the tributary cell persisting for A (sections A4 and A5). Vertical velocities were found to be consistent with the secondary flow cells identified from the secondary velocities in Fig 21. It was proposed that the limited extent and decreasing coherence of the secondary cells at these confluences is due to the Parana River's high width to depth ratios, around 200, and the flow resistance provided by the developed dune field. Suspended sediment was measured from aDcp backscatter, calibrated by physical samples. The greatest suspended sediment transport occurred around the edges of the scour holes, and was not found to correlate well with shear velocity calculated from applying the log law of the flow to the entire flow profile.

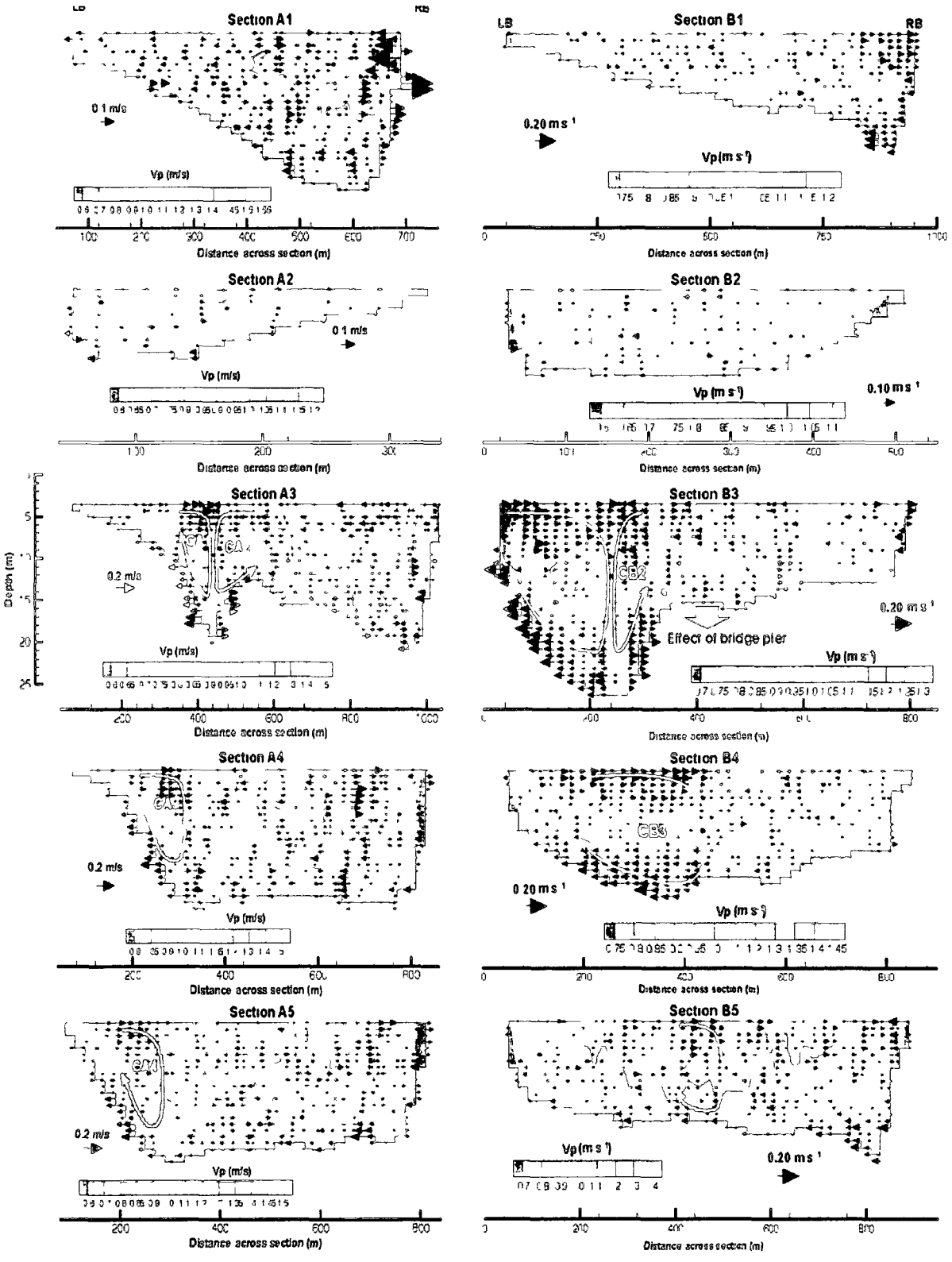

Figure 21 – Primary Vel. with Secondary Vel. Superimposed for Confluences A and B

(Szupiany et al, 2009)

Shear Layer Turbulence

High frequency velocity measurements at a specific location have been analysed according to the time averaged component and the fluctuation component. Spatial distributions of turbulence intensity, turbulent kinetic energy, Reynolds shear stresses, normal stresses, and cross-stresses have all been calculated using the fluctuation velocity component to characterize turbulence in confluence flows. The time averaged velocity distributions were described in the previous section. The upstream part of the mixing layer, or shear layer, has been found to be characterised by significantly higher turbulent kinetic energy than the ambient fluid, with the shear generated turbulence decaying rapidly despite the persistence of the mixing layer (de Serres et al, 1999, Boyer et al, 2006, Lane et al, 2008, Sukholodov and Rhoads, 2001, and Rhoads and Sukholodov, 2004). Differences in turbulence characteristics of the shear layer depended strongly on the bed morphology and momentum ratios of the confluences and flow events studied.

The turbulence was analysed throughout the depth of the flow at the high angle discordant bed Berthier-Bayonne confluence by de Serres et al (1999). The zone of maximum turbulent kinetic energy in the mixing layer was shown for all flow events to extend from the bed to the surface in the upstream section, but moved away from the bed towards the surface further downstream as the turbulence dissipated. The zone of higher turbulent kinetic energy widens downstream partially due to vortex stretching in the mixing layer, but also due to oscillations in the position of the mixing layer. The results for the flow event on October 2nd with a momentum ratio of 1.79 are shown in figure 22. The position of the mixing layer for the flow events measured varied according to momentum ratio, but was consistently reported to be tilted, with the location of the peak turbulent kinetic energy at the surface flow located closer to the Bayonne side and that the of the bed flow located closer to the Berthier side of the confluence (although this is not obvious in the kriged plots of figure 22).

At the Parana-Paraguay confluence, suspended sediment concentration was used to identify the mixing layer between the turbid Paraguay river and the clearer Parana river by Lane et al (2008). Stationary measurements were taken using an aDcp at intervals along the upstream part of the mixing layer during the slow mixing event, with a momentum ratio of 0.28. Correlations of fluctuations in suspended sediment concentration and cross-stream velocity were plotted, in order to identify large-scale lateral turbulent structures that would contribute to mixing. The low frequency, about 0.5 Hz, measurements recorded using an aDcp limited detection to large-scale turbulence. Negative correlations between concentration and cross-stream velocity fluctuations indicated movement of either turbid Paraguay fluid towards the Parana side or clearer Parana fluid towards the Paraguay side. These negative correlations peaked, especially at the surface, at 0.152 channel widths in the downstream direction along the mixing layer, and then rapidly decreased (see figure 23). Therefore, rapid flow mixing due to shear driven turbulence was limited to the very upstream part of the mixing layer near the confluence junction for this flow event with a near vertical mixing layer.

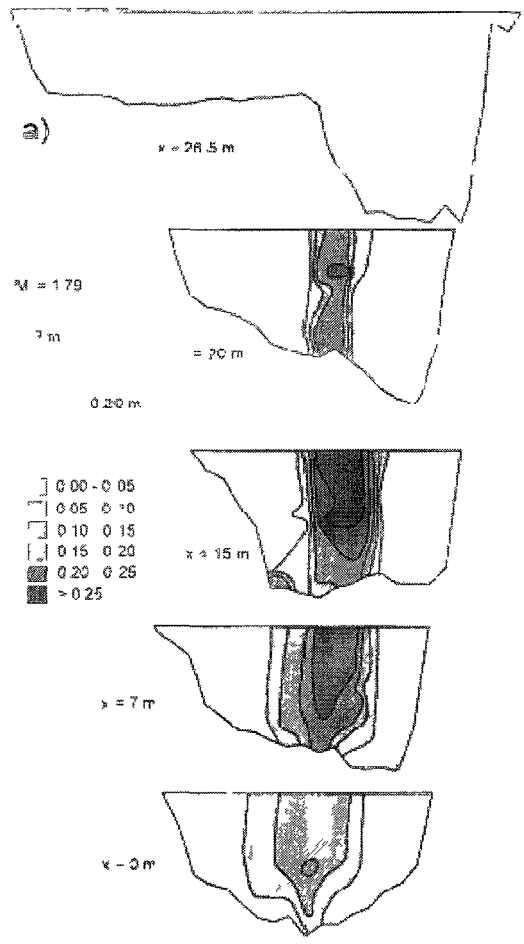

Figure 22 – Normalized turbulent kinetic energy at Berthier-Bayonne (Mr=1.79, de Serres et al, 1999)

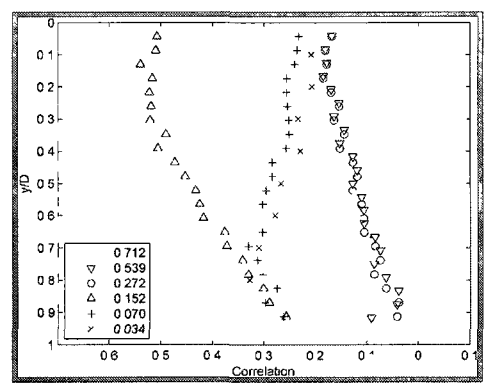

Figure 23 – Correlation of cross-stream velocity and suspended sediment conc. fluctuations (Lane et al, 2008)

Numerical Modelling

Investigation of the dynamics of confluences for a wide range of flow events has been approached by 3D numerical modelling, for both the average flow field and the evolution in time of the turbulent structures throughout the confluence. Most of the models have employed the Reynolds averaged Navier-Stokes equations, with either the k-ε or k-ω turbulence closure method (Weerakoon et al, 1991, Bradbrook et al, 1998, 2000 a, 2001, Biron et al, 2002, Huang et al, 2002). All these studies listed allowed the modelled water surface elevation to change, except for Weerakoon et al (1991) which used the rigid-lid approximation. However, the time averaging approach is a simplification of turbulent flows, and Bradbrook (2000 b) and Lane et al (2000) used the more complex Large Eddy Simulation (LES) to model the turbulent confluence flow. Most of the models have used the semi-implicit SIMPLE algorithm for the pressure-velocity coupling, however the pressure implicit splitting operator (PISO) algorithm used by Huang et al (2002) has been found to be more robust and efficient.

Natural confluences tend to have complex topographies. Representing these complex topographies has not been possible with the discretised meshes because they have introduced instabilities and convergence problems in the 3D numerical modelling. Even when convergence is achieved, the choice of discretized mesh influences that result. However, using smoothed and simplified topographies of natural confluences and 3D velocity measurements has resulted in some useful flow field results. The biggest problem has been the failure of models to capture fluid upwelling in confluences.

Weerakoon (1991) presented the first numerical modelling results, showing the development of helical flow cells under certain flow conditions for a symmetric high angle concordant bed confluence. The asymmetric high angle concordant bed Kaskaskia River-Copper Slough confluence was modelled by Bradbrook et al (2000a), yielding flow patterns qualitatively similar to those measured by Rhoads and

Kenworthy (1995 & 1998). Huang et al (2002) reported that the modelling of various flume concordant bed confluence conditions qualitatively described the secondary currents forming helical flow cells, but underestimated their strength. However, Huang et al (2002) attributed the underestimated secondary currents to the isotropic k-ω turbulence model used, suggesting that more complex turbulence models would be needed to improve model predictions.

Bradbrook et al (2001) modelled an asymmetric confluence at different confluence angles and with and without bed discordance. Model predictions compared well to measurements by Biron et al (1996 a & b), showing good representation of the stagnation zone and maximum downstream velocities, but were very poor for vertical velocities in the concordant bed case, having a correlation of only 0.10. Due to the flow separation over the step and increased lateral pressure gradient, even a small bed step was found to enhance cross-stream and vertical velocities, decreasing the water surface superelevation in the centre of the confluence and depression at the downstream junction corner. Water surface elevations at the discordant bed Berthier-Bayonne confluence were measured by Biron et al (2002) for six different flow conditions. Fluctuations in water surface elevation were quite marked, and higher elevation existed at the upstream stagnation zone, the Bayonne side in mid-confluence, and the Berthier side at the downstream end where upwelling of turbid Bayonne fluid was observed. The tilt in water surface elevation in mid-confluence, lower on the Berthier side and higher on the Bayonne side, has been attributed to the upstream curvature of the Berthier tributary producing a meander-bend like curvature where it meets the Bayonne flow. Numerical modelling of this confluence reproduced the higher water surface elevation of the stagnation zone, and the tilt between the lower elevation Berthier and higher elevation Bayonne, but it did not replicate the higher elevation on the Berthier side at the downstream end. This is not surprising as numerical models using a k-ε or a k-ω turbulence closure method have been shown not to predict fluid upwelling (Huang et al, 2002).

Summary

The mixing dynamics and bed morphology of river confluences adjust to the changing discharges and sediment loads entering from the tributaries. The characteristics common to high angle confluences include a stagnation zone with an elevated water surface at the junction apex and flow convergence and deflection. The mixing layer has an elevated water surface, the upstream section of which is termed the shear layer due to generation of turbulent structures along it, and a scour zone located below it. Flow accelerates through the confluence, and the difference in downstream velocity between the two flows dissipates though differences between secondary currents, temperature and turbidity can persist across the mixing layer. Other characteristics that may be present include the following: a pronounced scour zone with two upstream avalanche faces, a bed step with a single avalanche face, tilting of the mixing layer, full or partial helical flow cells, a downstream bar at the confluence exit, flow separation, and significant upwelling in the shear layer and/or at the downstream end. Initial studies were carried out in the laboratory, and progressed to field studies of small streams, and most recently to large rivers at high flows. The strong influence of bed morphology on mixing dynamics has revealed important differences between field sites studied.

Early research focussed on relating scour depth to confluence angle and the momentum ratio of the entering flows. Low angle confluences were not found to exhibit significant mixing dynamics. Two small channel natural asymmetric high angle confluences were identified, concordant bed and discordant bed confluences, leading to intensive study of two representative field sites, Kaskaskia River-Copper Slough (KRCS) and Berthier-Bayonne (BB) respectively. The position of the mixing layer and the scour zone underneath it was found to depend strongly on the momentum ratio of the flow event. At the concordant bed KRCS confluence, helical flow cells were found to exist on one or both sides of the vertical mixing layer but most strongly on the tributary side for momentum ratios over 1, with 2D turbulence produced at the shear layer. No helical flow cells were identified at the discordant

bed BB confluence, where the bed step from the shallower tributary resulted in a tilted shear and mixing layer, with 3D turbulence and strong fluid upwelling produced within the shear layer. Higher cross-stresses were found to correlate with bed-load transport measured by physical sampling at the edges of the scour zone for the BB confluence.

The study of high angle confluences at channel-forming flows along large rivers, with high width to depth ratios, has recently been made possible by moving boat aDcp measurement. At the Parana-Paraguay discordant bed confluence with the tributary deeper, a tilted mixing layer and rapid flow mixing occurred with the momentum ratio closer to 1, but a vertical mixing layer and slow flow mixing occurred at a lower momentum ratio. The shear layer constitutes the upstream section of the mixing layer, and consists of much higher turbulent kinetic energy than the ambient fluid. Shear layer turbulence was found to dissipate very quickly in the downstream direction, within one channel width at the Parana-Paraguay confluence, where rapid flow mixing occurred as the result of channel-scale secondary circulation patterns not turbulence. Two Parana River confluences downstream of mid-channel islands were studied by Szupiany et al (2009). For both, weak back to back helical cells were identified at the vertical mixing interface, though limited in downstream and cross-stream extent to the scour zone. This pattern of limited helicity is thought to result from the increased influence of roughness in a river with width to depth ratio over 100. The greatest suspended sediment transport occurred around the edges of the scour holes, and was not found to correlate well with shear velocity calculated from applying the log law to the entire flow profile.

Numerical modelling of rivers confluences is a useful tool and is progressing thanks to improvements in computer power and the recent availability of high quality 3D data. However, very smoothed and simplified bed morphology is required for solution convergence, whereas the strong influence of bed irregularities on mixing dynamics at confluences in field studies is outlined above. Poor replication of the highly anisotropic turbulence generated at the shear layer and any bed discordances by even

the most complex large eddy simulation (LES) turbulence modelling limits its current usefulness. Physical measurement of complex confluences is still required.

Acoustic Measurement Review

Introduction

Acoustic measurement of water velocities and discharge in rivers has now become standard practice, while using apparent bed velocity as a measure of bed-load sediment transport is currently being investigated primarily in research. Acoustic Doppler current profiler (aDcp) bed-load velocity is a fast, non-intrusive technique that yields a spatial distribution when measured from a moving boat. Apparent bed velocity is defined as the difference between the boat velocity measured by the bottom track pulse, biased by sediment movement, and the boat velocity measured by GPS. An apparent average particle velocity is determined from the Doppler shift of the returning acoustic echoes of the bottom track pulse. In this section, the principles of acoustic measurement of flow and bed velocities are presented, and studies relating the two are reviewed.

Principles

An aDcp transmits a sound pulse into the water and measures the Doppler shift of the echoes that bounce off scatterers in the flow. The scatterers are assumed to be travelling at the speed of the flow. The Doppler shift is related to the velocity of the water relative to the instrument. The Doppler shift is defined as:

$$F_d = 2 F_s \left(\frac{V}{c}\right) \quad (8)$$

Where: F_d = the Doppler shift frequency, F_s = frequency of the aDcp, c = the speed of sound (~1500 m/s), V = relative velocity of the scatterers.

An aDcp sends pulses in to the water along 3 or 4 beams and listens to the returning echoes over segments of time, with each segment relating to a specific distance along the beam path. This is known as range gating, which enables velocities to be determined throughout the depth of the water column (figure 24). The depth of flow that corresponds to each distance along the beam path can be calculated from the angle ϕ. The velocity at each depth is assigned to the centre of each depth cell; there is some overlap between measurement volumes resulting in typical correlation of measured velocities in adjacent bins of ~15% (Rennie and Church, 2010).

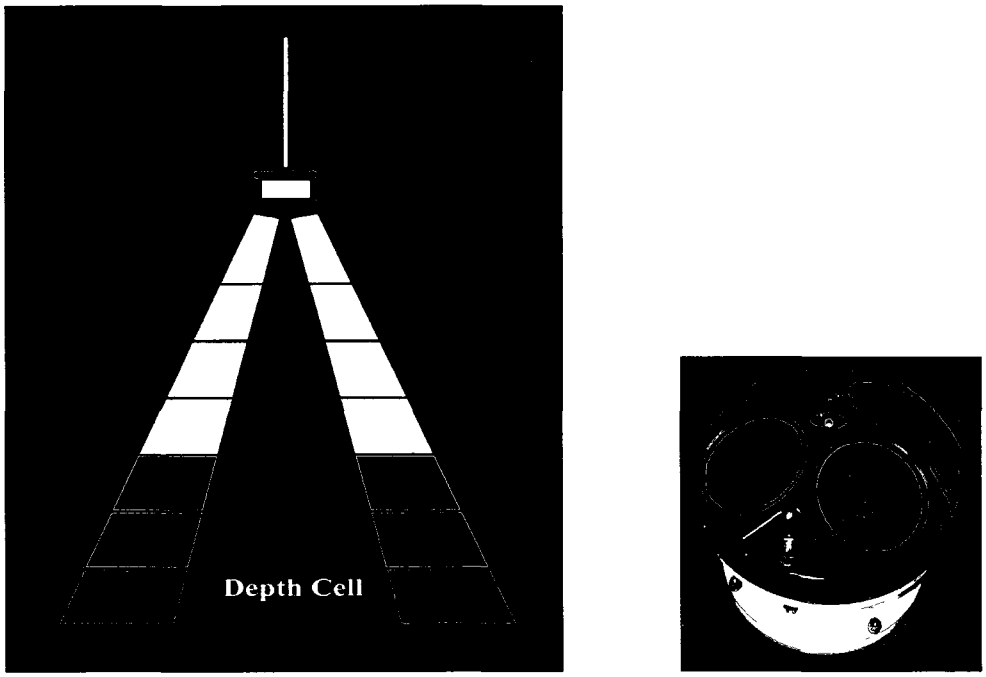

Figure 24 – aDcp sound pulse measurement and 4 beam head (Water Survey Canada)

An aDcp can only measure the shift in the component of velocity that is parallel to the transducer axis, which is at an angle to the vertical of ϕ. A horizontal velocity has a much smaller component in the beam axis than the vertical velocity (figure 25). Three beams are needed to solve for the three components of the velocity; in a 4 transducer aDcp, the fourth beam is used to yield a second value for vertical velocity. This is used to evaluate the measurement error. The algorithm used to determine the velocity components assumes homogeneous conditions over the area encircling those insonified by the transducer beams. This assumption becomes more tenuous the greater the distance from the aDcp due to beam divergence. It is especially significant for flow velocities and apparent bed-load velocity at large flow depths, particularly if bed topography is irregular.

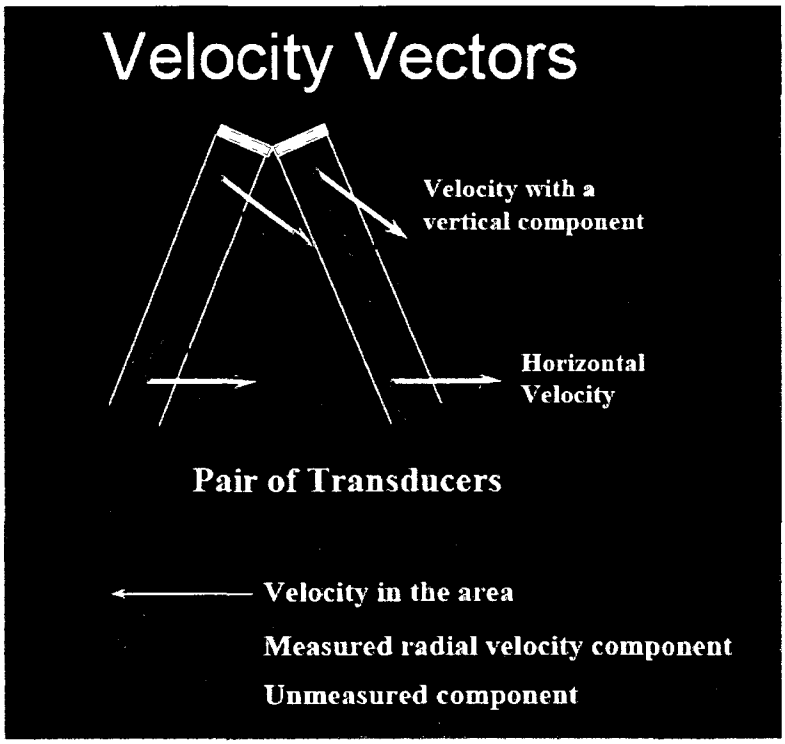

Figure 25- Velocity Vectors (USGS, 2004)

A separate pulse, called the bottom track pulse, was designed to measure the relative velocity between the instrument, or the boat to which it is attached, and an immobile bed. In the case of a mobile bed, the bottom track velocity is biased by the movement of the sediment along the bed, and a DGPS system is required to measure the velocity of the boat relative to the Earth. The difference between the biased bottom track velocity and the DGPS velocity is known as the apparent bed velocity. The apparent bed velocity is considered a measure of the bed-load sediment transport rate.

$$V_b = V_{DGPS} - V_{bt} \qquad (9)$$

Where: V_b = apparent bed velocity, V_{DGPS} = velocity of the aDcp relative to the Earth, V_{bt} = velocity of the aDcp relative to the bed.

The bottom track pulse measures the echoes from a volume, not an area. The echoes from the bed consist of echoes from particles moving in the bed layer as well as echoes from immobile sections of the bed. Backscatter, from particles moving just above the bed, contributes positively to the signal and is known as water bias. The distance above the bed to which particle movement influences the signal depends on the pulse length selected (Rennie and Millar, 2004).

Particle Velocity

An aDcp bottom track pulse measures an apparent bed-load velocity, v_b , in the insonified volume. The average bed-load particle velocity (v_p) represents the average of the different velocities, of the particles of different sizes, that exist in bed-load transport. For a sand bed where these approximations can be considered valid, the bed-load transport rate can be calculated as (Rennie et al, 2002):

$$g_b = v_p \, d_a \, (1 - \lambda_a) \, \rho_s \qquad (10)$$

Where: v_p = average particle velocity, d_a = depth of active bed layer, λ_a = porosity of active bed layer, ρ_s = density of sediment.

The contribution of the particles moving just above the bed depends on the frequency of the instrument and the characteristic size of those particles. An aDcp preferentially measures reflections from particles with a diameter equal to or greater than the wavelength of the instrument's sound wave (Thorne et al, 1995).

Stationary Boat Studies

Initial studies of apparent bed velocity correlated the bed velocity with bed-load transport rate measured by physical sampler and by dune tracking.

The first study was conducted in 2002 by Rennie et al. Apparent bed velocity was correlated to bed-load transport rate, measured by physical sampling, in the Agassiz gravel bed reach in the Fraser River.

Apparent bed velocity and concurrent bed-load transport rate measurement, by physical sampling, were compared for five data sets from three reaches in the Fraser River (Rennie and Villard, 2004). Sea Reach and Canoe Pass were sand bed reaches near the river mouth, and the third was the gravel bed Agassiz site. In the sand bed reaches, apparent bed velocity was measured on the stoss sides of dunes to reduce spatial heterogeneity. The apparent bed velocity was strongly correlated with measured bed-load transport rate for the long average Agassiz data and the Sea Reach data, and less well for the 5 minutes Agassiz data and both Canoe Pass data sets (Table 1). Larger values of g_b existed for the Agassiz data than for the Sea Reach data for similar values of apparent bed velocity; for particles travelling at the same average velocity, the larger the particle the higher the mass transport rate. Non-dimensionalised g_b, g_b^*, was correlated with the non-dimensionalised v_b, v_b/u^*, with 42% of the variance in g_b^* explained by variance in v_b/u^*. Apparent bed velocity was non-dimensionalised by dividing it by the shear velocity, u^*, calculated from the Keulegan equation. Transport rate was non-dimensionalised by using Einstein's formula. A lower g_b for Canoe Pass, 2001, was measured than for Canoe Pass, 2000,

for similar v_b because a longer pulse length was used for Canoe Pass, 2001, resulting in increased water bias in v_b.

Table 1: Linear regression and functional relations for measured g_b vs measured v_b (Rennie and Villard, 2004)

Location	n	r^2	Regression	Functional Relation	95% CI[b]	$r^2 \setminus b_r^2$
Agassiz	9	0.89	$g_b = 1.2v - 0.037$	$g_b = 1.2v - 0.041$	0.91 1.7	0.96
Agassiz 5 min	13	0.52	$g_b = 2.0v - 0.059$	$g_b = 2.6v - 0.088$	0.60 7.8	.3
Sea Reach	68	0.76	$g_b = 0.057v - 0.0007$	$g_b = 0.062v + 0.0005$	0.062 0.062	2.1
Canoe Pass 2000	49	0.38	$g_b = 0.23v + 0.001$	$g_b = 0.36v - 0.00008$	0.34 0.38	0.97
Canoe Pass 2001	15	0.42	$g_b = 0.090v - 0.0003$	$g_b = 0.14v - 0.0004$	0.0043 0.18	0
Nondimensional	127	0.42	$g_b^* = 0.043(v_* / w^*)^{0.5}$	$g_b^* = 0.045(v_* / w^*)^{0.90}$	0.74 2.5	12

Modelled g_b was also correlated with the measured g_b for all data sets in this study. In the gravel bed Agassiz reach, g_b was calculated using the Van Rijn and Ackers-White formulae. In the sand bed reaches, in addition to those two formulae, the g_b was kinematically modelled using equation 10. There were no significant correlations between the modelled and measured g_b for the Agassiz data sets, but there were correlations for all three sand bed data sets. The sediment transport equations over-predicted g_b for the sand bed data sets (Table 1). The kinematically modelled g_b was over-predicted for the Sea Reach data and under-predicted for the Canoe Pass, 2000, at higher transport rates. Correlations of v_b and g_b calculated kinematically with measured g_b varied for these data sets; therefore, v_b must be calibrated for each site. Variations resulted from differences in particle size, suspended sediment and aDcp operation.

Apparent bed velocity was correlated to bed-load transport rate from physical sampling and dune tracking by Gaeuman and Jacobson (2007) in the lower Missouri River. Measurements were taken in the thalweg, which consisted of a sand bed with dunes. Apparent bed velocity was correlated with g_b measured from dune tracking for values lower than 0.9 kg/m/s, while large variability above that value resulted from localized values of g_b being measured over large dunes. Low correlation existed

between v_b and g_b measured from physical sampling. It was suggested that physical sampling was an unsatisfactory method for characterizing g_b at the higher transport rates found in the lower Missouri River.

Gaeuman and Jacobson (2006) also modelled the relationship between the average particle velocity, v_p, and the apparent bed velocity measured by the aDcp. The average particle velocity was calculated using the van Rijn formula, a shear stress approach. The spatially averaged surface particle velocity can be assumed to vary from a value much lower than the calculated v_p near entrainment (because much of the bed surface is immobile) to a value approaching the calculated v_p at higher transporting conditions (Gaeuman and Jacobson, 2006).

$$v_b = v_p \, w_b \, w_f \qquad (11)$$

Where: v_p = particle velocity calculated from Van Rijn, w_b = weighting factor for percentage of bed mobile, w_f = weighting factor for position over bedform.

The weighting function, w_b, evaluates the proportion of the bed particles that are moving and accounts for the relative strength of the backscatter from the immobile bed particles versus mobile particles. Gaeuman and Jacobson (2006) considered particles moving in different layers of the active bed, with the immobile bed consisting of those bed particles that are not acoustically blocked by moving particles in any layer above them.

$$w_b = \left(\frac{b_p}{b_p + b_b F} \right) \qquad (12)$$

Where: b_p = fraction of bed area with moving bed particles, b_b = fraction of immobile bed 'visible' to transducer beam, F = relative strength of echoes reflected from immobile bed.

The bed fractions depend on the particle concentration in the bed-load layer and the height of the top of the bed-load layer, both calculated according to van Rijn (1984).

The value of F was assumed to be roughly 10. An additional scaling factor, w_f, was proposed, but not defined, to account for spatial differences due to the influence of bedform morphology. As expected, the ratio of v_b/v_p increased with the transport stage, T^*, and the modelled v_b was found to be close to the measured v_b.

Ramooz and Rennie (in press) conducted a calibration of bed velocity at St. Anthony's Falls Laboratory in the US. Apparent bed velocity was reasonably correlated with bed-load transport rate from physical sampling and from dune tracking for the sand bed runs. It was the only study to evaluate the sensitivity of v_b correlation with g_b to the aDcp transmit frequency; there was some difference, with the highest correlation occurring for the 600kHz aDcp.

Instrument error constitutes the majority of the measurement error for apparent bed velocity (Rennie et al, 2002). The probability density function (pdf) of particle velocities measured in the insonified beam areas of the gravel beds at Agassiz and Norrish Creek was modelled by deconvolving the pdf of the instrument error from that of the measured data (Rennie and Millar, 2007). In gravel bed reaches, bed-load transport occurs as discrete events, with a large percentage of the bed being immobile at any given time, with the bed velocity assumed to be an average of moving and stationary particles. Two velocity distributions were used to model the actual bed velocities, a compound Poisson-gamma distribution (cPg) and an empirically fit gamma distribution. There was good fit between the modelled and measured distributions. However, there were many possible velocity distributions that fit, due to the strong influence of the pdf of the noise on the pdf of the generated velocity. The compound Poisson-gamma distribution was found to fit better with optimized parameters. The velocity distributions were positively skewed, which would result from a few high values among mostly low values, as expected for partial transport of gravel. The instrument noise was found to be 0.21 m/s for Agassiz (adjusted to single ping) and 0.31 m/s for Norrish Creek. This error was similar to that for water velocity measurement, 0.23 m/s for a 1 second average with 0.20 m pulse length.

Moving Boat Studies

Two studies of the spatial distribution of apparent bed velocity in a reach have been conducted, Rennie and Millar (2004) and Rennie and Church (2010). Kriging was used to smooth the raw data to produce coherent distributions from moving boat apparent bed velocity measurement. Assessment of these distributions was achieved by comparison to those of shear velocity, depth, near-bed water velocity, and depth averaged water velocity.

Shear velocity was calculated by Rennie et al (2002), Rennie and Millar (2004), and Rennie and Church (2010), from a two-parameter log law fit of the vertical streamwise water profiles measured with the aDcp, where the intercept provides an estimate of the bed roughness and the slope then gives the corresponding estimate of shear velocity.

$$u = \frac{u_*}{\kappa} ln(h) + \frac{u_*}{\kappa} ln\left(\frac{30}{k_s}\right) \qquad (13)$$

Where: u = the velocity at, h = elevation above the bed, $u_* = \sqrt{\frac{\tau}{\rho}}$ = shear velocity, κ = von Karman constant (0.41), k_s = bed roughness

Significant variations existed in the distributions mapped in Sea Reach, a sand bed estuarine distributary of the Fraser River (Rennie and Millar, 2004). The near bed velocity was measured in the bin between 25 cm and 50 cm above the bed. The bed shear velocity was calculated from fitting the log law to the measured vertical velocity profiles. Both the near-bed water velocities and the depth averaged water velocities were correlated with the apparent bed velocities for spatial lags up to about 10 m. Similarly, areas with high shear velocity matched those with high apparent bed velocities. High shear velocities were found to stretch from the upper left side to the lower right side of the reach.

Velocity distributions over a 5.5 km long gravel bed stretch of the Fraser River about 150 km upstream from the river mouth, were produced for a moderate and high freshet flow, of 6 000 m^3/s in 2006 and 11 000 m^3/s in 2007 (Rennie and Church, 2010). Vertical velocity profiles, averaged over a width of 9 m (2007 survey), were fitted to the log law to calculate the shear velocity. Apparent bed velocities were interpolated by kriging onto a 25 m grid to yield the spatial distribution. The distributions of flow depth, depth averaged water velocity and shear velocity were generated likewise. The distributions for depth, depth averaged water velocity (figure 26), shear velocity and apparent bed velocity (figure 26) were very coherent. Maximum values of shear stress were found in the thalweg in and just downstream of areas of flow convergence, the deep pools in the bends. Areas of flow separation and over shallow point bars had lower shear stress. Apparent bed velocity matched bed shear except in a deep pool adjacent to a rapidly receeding bank, where highly turbulent flow existed. Rapid erosion and the highest apparent bed velocities existed along this pool, which was located downstream of the river's confluence with the Minto side channel.

The uncertainty of the spatial distributions was assessed according to three measures: modelled error, of both measurement error and real temporal fluctuations in water velocity due to turbulence, the measured local standard deviations and the kriging standard deviations, which gives an indication of the degree of spatial autocorrelation in the data and hence the reliability of the estimated spatial pattern. For the high flow 2007 survey, the average uncertainty of a single bin single ping velocity measurement was 0.35 m/s, that of the resulting mean depth-averaged velocity was 0.10 m/s, that of shear velocity estimates could be reduced to less than 0.02 m/s if at least 10 pings are used to generate an average velocity profile, and that of single ping apparent bed-load velocity was 0.07 m/s. Measured local standard deviations were somewhat higher than the modelled values, possibly positively biased by real spatial variation. The mean and standard deviation of depth-averaged water velocity throughout the reach were 2.2 and 0.7 m/s, for interpolated and single ping U, with interpolation error dominating the uncertainty. Tighter transect spacing would

reduce the interpolation error. High apparent bed velocity values were found to be significant at a 95% confidence level, despite the large estimated uncertainty.

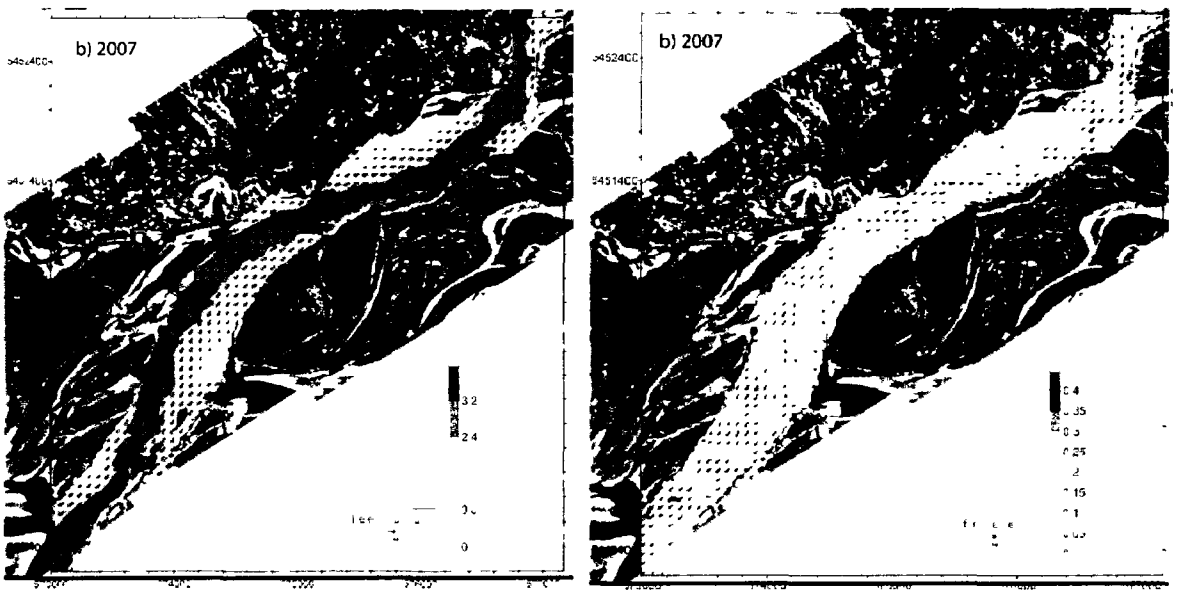

Depth Averaged Water Velocity (m/s) Bed Velocity (m/s)

Figure 26 – 2007 Velocity Distributions on the Fraser River (Rennie and Church, 2010)

Shear velocity is used as a measure of sediment transport, and compared to more direct measures of sediment transport in many moving boat aDcp studies: apparent bed velocity (Rennie and Millar, 2004, Rennie and Church, 2010), and backscatter intensity and suspended sediment concentration (Szupiany et al, 2009). The log law was also applied to the near-bed area to determine the near-bed velocities that are not directly measureable by aDcp and the flow patterns were compared to backscatter intensity patterns along a large river bend (Dinehart and Burau, 2005). The most repeatable estimate of shear velocity determined from aDcp single transect moving boat measurement was assessed by comparing four different methods of applying the log law to the vertical downstream velocity profile from outward and return transects for the same locations (Sime et al, 2007). The shear velocity estimate calculated using

the vertically averaged mean velocity and a roughness height estimated from bed D84 (equation 14) was found to be the most repeatable, as compared to two estimates calculated using the estimated roughness height and only the lowest and the average of the three lowest velocities (equation 14) and to a two-parameter log law fitted to the entire vertical velocity profile (equation 13).

$$u = \frac{u_*}{\kappa} ln\left(\frac{z}{z_0}\right) \qquad with\ z_0 = 0.1D84 \qquad (14)$$

Where: u = velocity, u^* = shear velocity, κ = von Karman constant (0.41), z = elevation above the bed, z_0 = small positive height at which u = 0.

Traditionally, characterization of flow patterns in rivers was determined from point measurements, averaged over 3-5 minutes, taken at a few locations across a cross-section. Acoustic flow measurement from a moving boat yields instantaneous, spatially intense 3D measurements, which vary from the mean flow values due to measurement errors and real temporal fluctuations. Researchers have calculated mean flow values by averaging values over multiple ensembles, either during data collection or in post-processing, and also either incorporating averaging from ordinary kriging of results through the flow volume from single transects or averaging the results of repeated transects at specific cross-sections. A comparison of fixed vessel and moving vessel aDp measurements at cross-sections of the Parana River (Szupiany et al, 2007) indicates that the general patterns of secondary flow can be identified from a single transect, but that 7 minutes of fixed vessel measurement or 5 repeated transects for moving vessel measurement are required to reduce mean horizontal flow velocity error to less than 5%. Errors in shear velocity were 10-15%, when calculated from flow velocity profiles resulting from 5 moving vessel transects. Mean flow values were determined from recording single transects by Rennie and Church (2010), Rennie and Millar (2004), Lane et al (2008), Parsons et al (2007),

Parsons et al (2005), Kostaschuk et al (2005) and from repeated transects by Szupiany et al (2009), Sime et al (2007) and Dinehart and Burau (2005).

Summary

Apparent bed velocity measurement using an aDcp is a fast and non-intrusive technique. The great advantage of using aDcp to characterize bed-load transport is the ability to measure the spatial distribution of apparent bed velocity. Stationary measurement of apparent bed velocity in sand and gravel reaches has been correlated to bed-load transport rate measured concurrently from physical sampling, dune tracking (for sand bed rivers), and bed shear. Apparent bed velocity distributions measured from a moving boat have been correlated to concurrent distributions of near-bed water velocity, depth averaged water velocity, shear velocity, and channel depth. Apparent bed velocity needs to be calibrated for each site; the calibration depends on the sediment size and the operating parameters of the aDcp.

Error is a significant limitation of bed velocity. Instrument error constitutes the majority of the error (Rennie et al., 2002). Raw bed velocities are very noisy, and must be averaged. The error of the bottom track velocity for a mobile bed is the same order of magnitude as that for water velocity (Rennie and Millar, 2007). Moving boat measurements use the inherent averaging of kriging to reduce error (Rennie and Millar, 2004, and Rennie and Church, 2010).

Methodology

Study Site

The confluence of the Fraser River main channel with Minto side channel, is located near the town of Chilliwack, BC, downstream of the confluence of the Harrison river with the Fraser. This stretch of the Fraser River flows over a confined, slowly-aggrading, alluvial fan with a sinuous, wandering pattern around mid-channel islands. The gravel bed is bi-modal, with a gravel D50 of 25-30 mm, and fine sand comprising about 10-20% of the total (Church, 2001). The D84 was estimated to be 40 mm for the confluence area, from a 40 km survey of upper and mid bar locations exposed at low discharge along the lower Fraser River (Sime et al, 2007). Large volumes of sediment are eroded and deposited locally during the spring freshets, in areas of flow convergence and divergence respectively, although the net sediment transport through the reach is relatively small. Average particle path lengths range from several hundred metres to several kilometres (Church, 2001). Channel instability is, therefore, characteristic of this reach, and it provides excellent fish habitat. Management of erosion and flooding along the south bank of this reach has become important due to infrastructure development over the last century.

The confluence of Minto side channel with the main channel comprises the lower portion of an intensively studied reach that extends upstream of the confluence of the Harrison and Fraser rivers. The single channel flow of the Fraser currently splits around the upper end of the consolidated Minto/Harrison island complex, with the main channel following the right bank towards the mouth of the Harrison river and Minto side channel branching off to the left (see figure 28). Aerial photographs, from 1928 to 1999 (Church and Ham, 2004), showed significant changes in the locations of islands and channels between Foster bar and the survey area. The first maps of the area suggest that Minto channel formed the main channel in the late 19th century, though located northwest of its current location. Both the lower Minto channel and

the islands opposite were established in their current location south of the main channel by 1928. The portion of the channel upstream from the present 2008 survey has been very active over the last century. The formation of Harrison Island split the flow, with the main channel first flowing left along what is now upper Minto channel, and later right of the Harrison island/bar complex. Realignment of the channel along the left bank, upstream of the split, eroded material from upstream and deposited it as Foster bar, which has cut off most of the sediment transport from Minto side channel.

An acoustic survey conducted in 2006 of a 6 km stretch of the Fraser River (Rennie and Church, 2007), which included the confluence of Minto side channel with the main channel, revealed a deep scour hole and a rapidly eroding cutbank along the left bank of the confluence. Comparison of the 1971 (figure 27) and 1999 (figure 28) aerial photographs with the 2006 acoustic survey (figures 29 and 30) showed aggradation on Calamity bar, the north bank of the main channel downstream of the Harrison confluence, and increased sinuosity of the main channel between lower Minto and Queen Islands. The resulting deposition on the north and west sides of lower Minto Island, and corresponding erosion along Queen Island, has changed the confluence topography and angle. The tightening of the channel bends redirects the thalweg across to the left bank at the downstream end of the confluence area, and Minto side channel flow is turned by the deposition downstream of lower Minto Island and directed down the left bank of the confluence. This has resulted in a high confluence angle. The plot of depth averaged velocity in the confluence area from the 2006 acoustic survey clearly showed the sinuous thalweg (see figure 29).

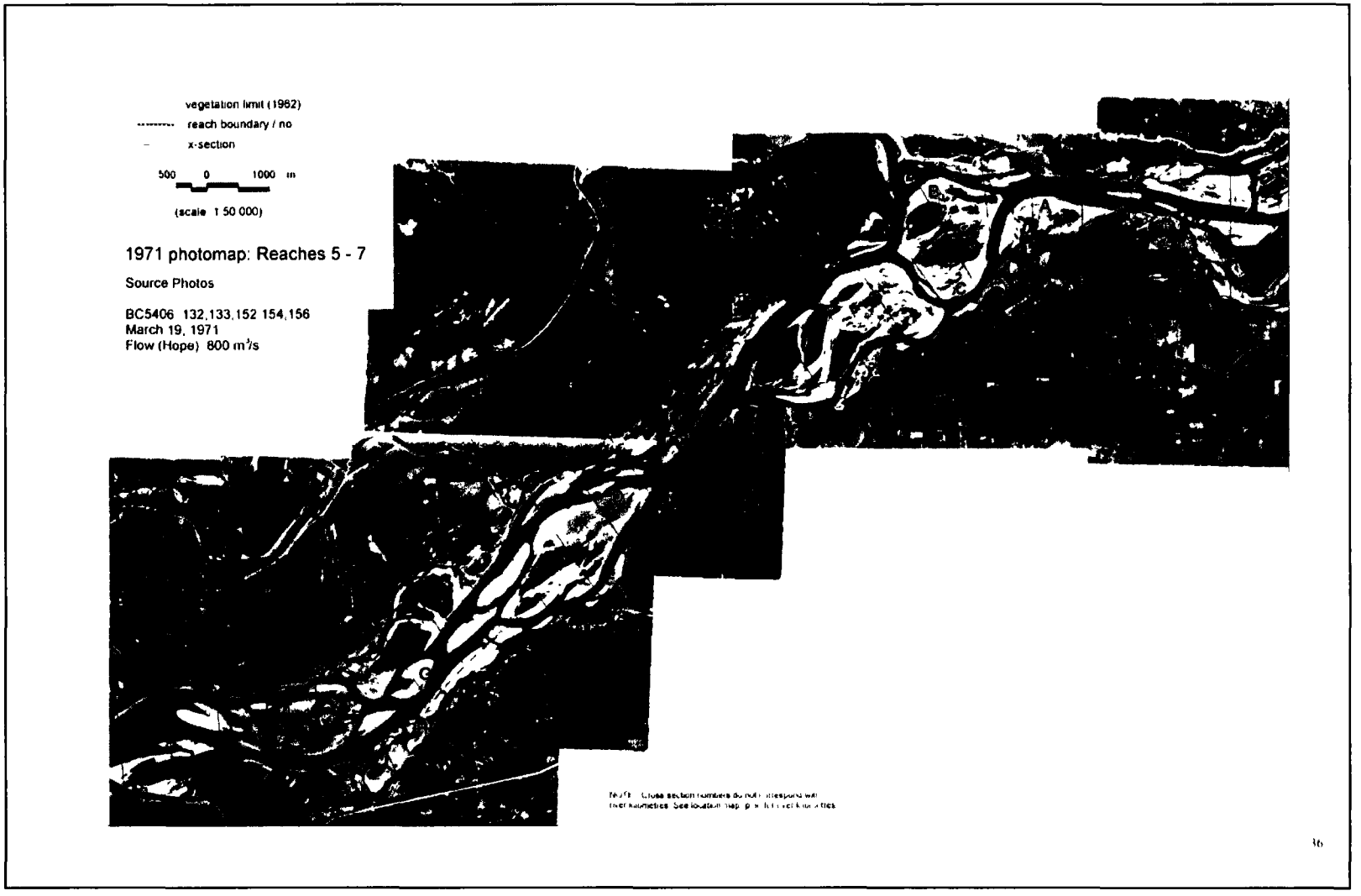

Figure 27 – Minto/main channel confluence, 1971 (sections 58 & 60)

(Church and Ham, 2004)

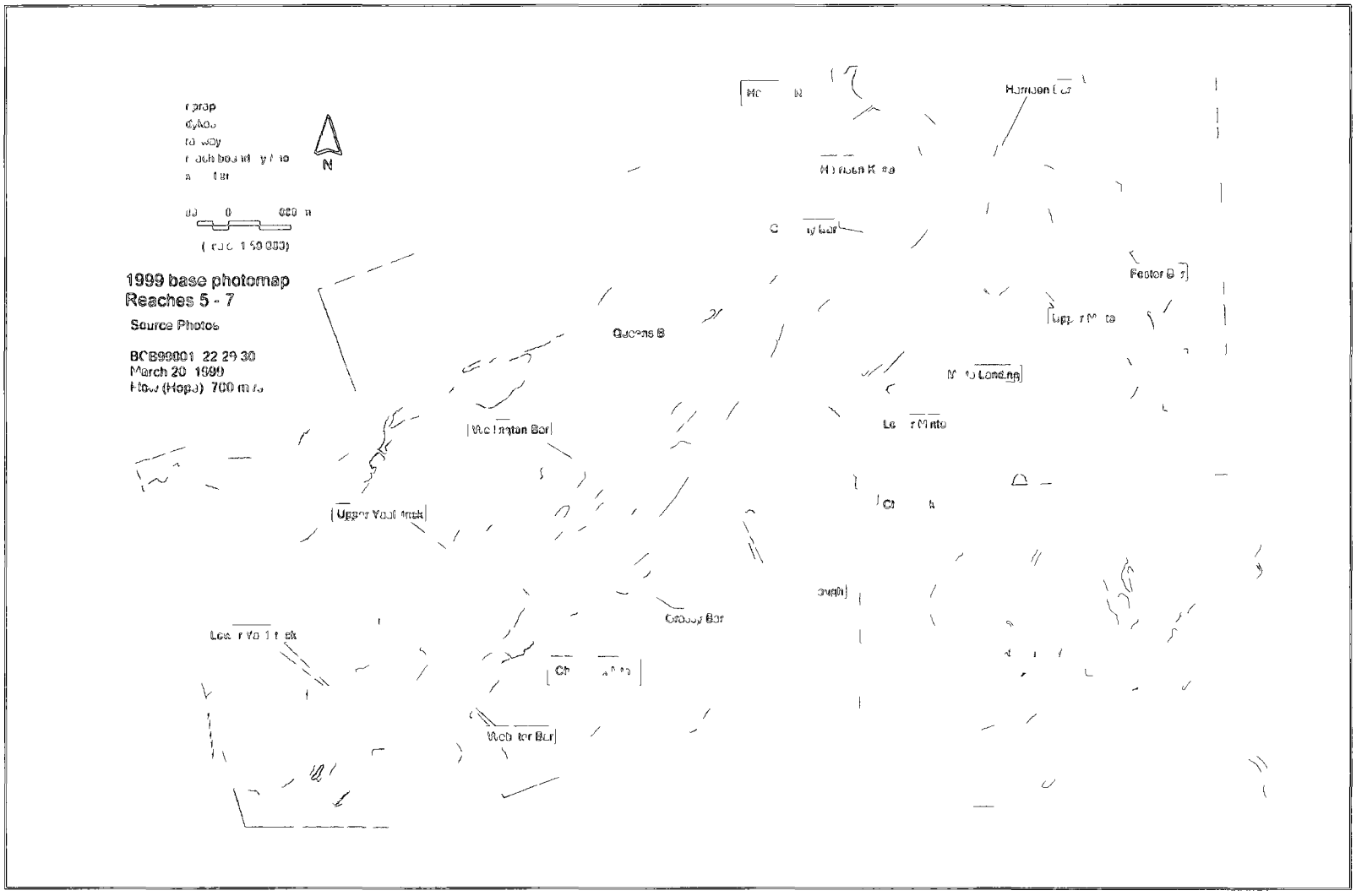

Figure 28 – Minto/main channel confluence, 1999 (sections 58 & 60)

(Church and Ham, 2004)

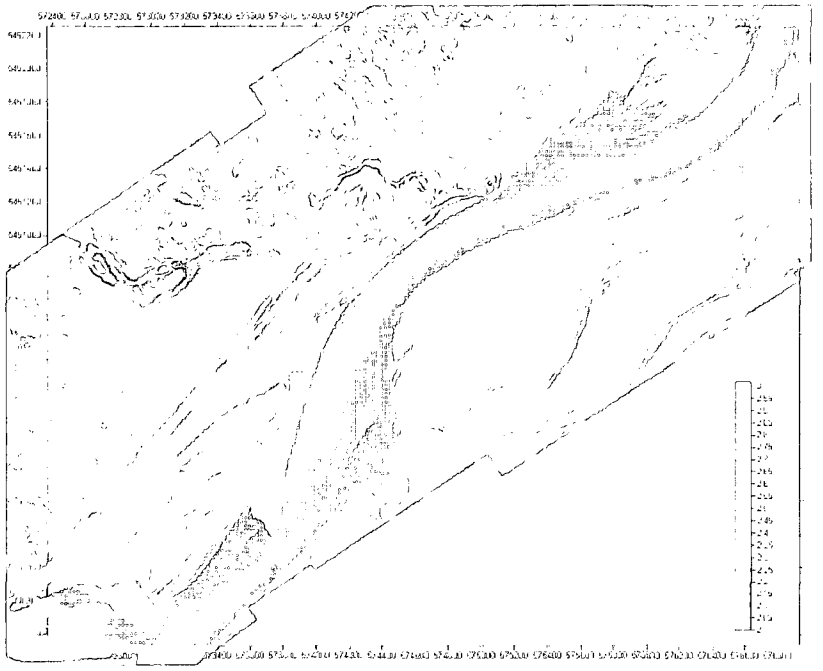

Figure 29 – Depth averaged velocity (m/s), Minto/main channel confluence (Rennie and Church, 2007)

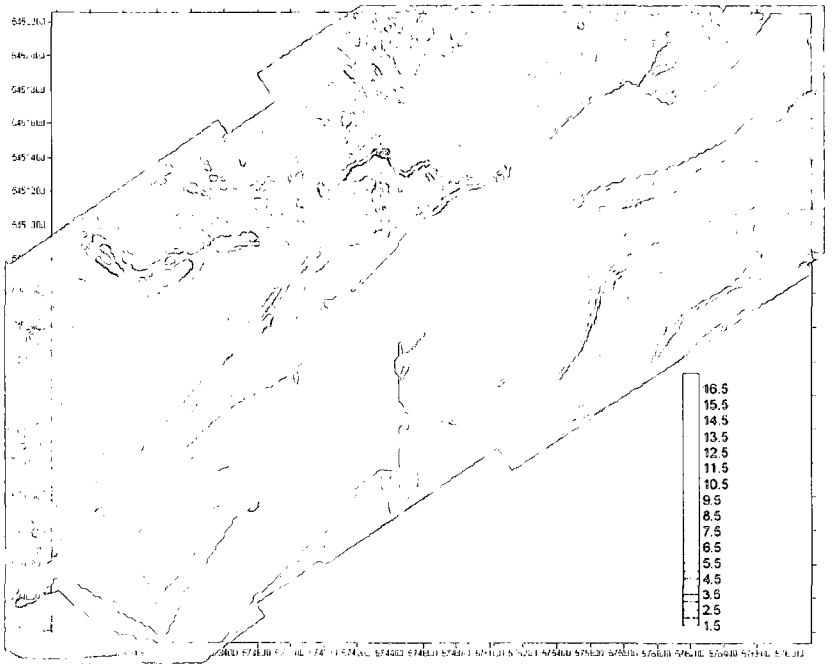

Figure 30 – Channel Depth (m), Minto/main channel confluence (Rennie and Church, 2007)

Measurements

Flow patterns and sediment transport through the confluence of Minto side channel with the main channel of the Fraser River, near the town of Chilliwack, BC, Canada, were measured on June 10th and 11th, 2008, during the falling limb of the spring freshet. The combined discharge was 7500 m^3/s, 5000 m^3/s in the main channel and 2500 m^3/s in Minto side channel, and the momentum ratio was 0.3. The main channel width is around 500m and that of Minto side channel about 300m. The river discharge at the Mission gauge 25 km downstream was around 9500 m^3/s on June 10th , when the main confluence area was surveyed, and 9000 m^3/s on June 11th, 2008, when Minto side channel was surveyed, so each day's survey was plotted separately. The edges of the mid-channel islands were inundated on June 10th, and close to bankfull on June 11th. An acoustic Doppler current profiler (aDcp) was used for single transect moving boat measurement of flow and bed velocities throughout the confluence area. A Teledyne RD Instruments 4 beam 1.2 MHz Rio Grande Workhorse aDcp with RTK-GPS was attached with a side mount to a 4.9 m aluminium boat with a 30 hp outboard engine. Real-time kinematic differential global positioning system (RTK-DGPS) position data were collected at 10Hz with a dual frequency Novatel Propak® 23 LB+ receiver, with reported relative horizontal position accuracy of ±2 cm CEP (i.e. 50% of position estimates have error < 2 cm). The average error of measured RTK-DGPS velocity was evaluated and determined to be 2.6 cm/s (Rennie and Rainville, 2006). The data were filtered to retain only those ensembles recorded using this high quality dual frequency RTK-DGPS. Single ping aDcp ensembles were collected using broadband Water Mode 1 and Bottom Mode 5, with a radial ambiguity velocity of 4.1 m/s and 25 cm bins at a sampling frequency of approximately 2 Hz. The first bin in each ensemble was centred at a depth of 1.00 m, and bins within the lowest 6% of the flow depth were discarded due to interference from beam side lobes. The aDcp internal compass was calibrated to ±1° several times a day, *in situ*, using RDI compass calibration AX command (Workhorse Commands and Output Data Format, 2002). Transects for the main confluence area were spaced about 50 m apart and traversed diagonally into the

main channel current and straight across the mixing interface near the left bank, with the boat powering upstream into the main channel current, and moving upstream when travelling towards the right bank and downstream when travelling towards the left bank. Transects for the Minto side channel were also spaced about 50 m apart and traversed diagonally into the Minto channel current with the boat powering upstream into the Minto current and moving downstream in both directions of travel. The main confluence area surveyed and the transect lines navigated on June 10th, and those for Minto side channel on June 11th, 2008, are shown in figure 31.

The 2008 survey is displayed on the 2008 airphoto, with the measurement areas for the main confluence and Minto side channel shown in outline in figure 32. Erosion is evident along the right bank of the main confluence area and deposition downstream (West) of Minto Island, which is consistent with the continuation of the increase in sinuosity of the main channel thalweg noted from previous studies. Erosion is also evident along the left bank of the main confluence area. Rock riprap has been placed at the upstream and downstream end of the left bank of the main confluence area, with increased erosion occurring along the unprotected part of the bank in between, shown in photos of the site in figures 33, 34, and 35.

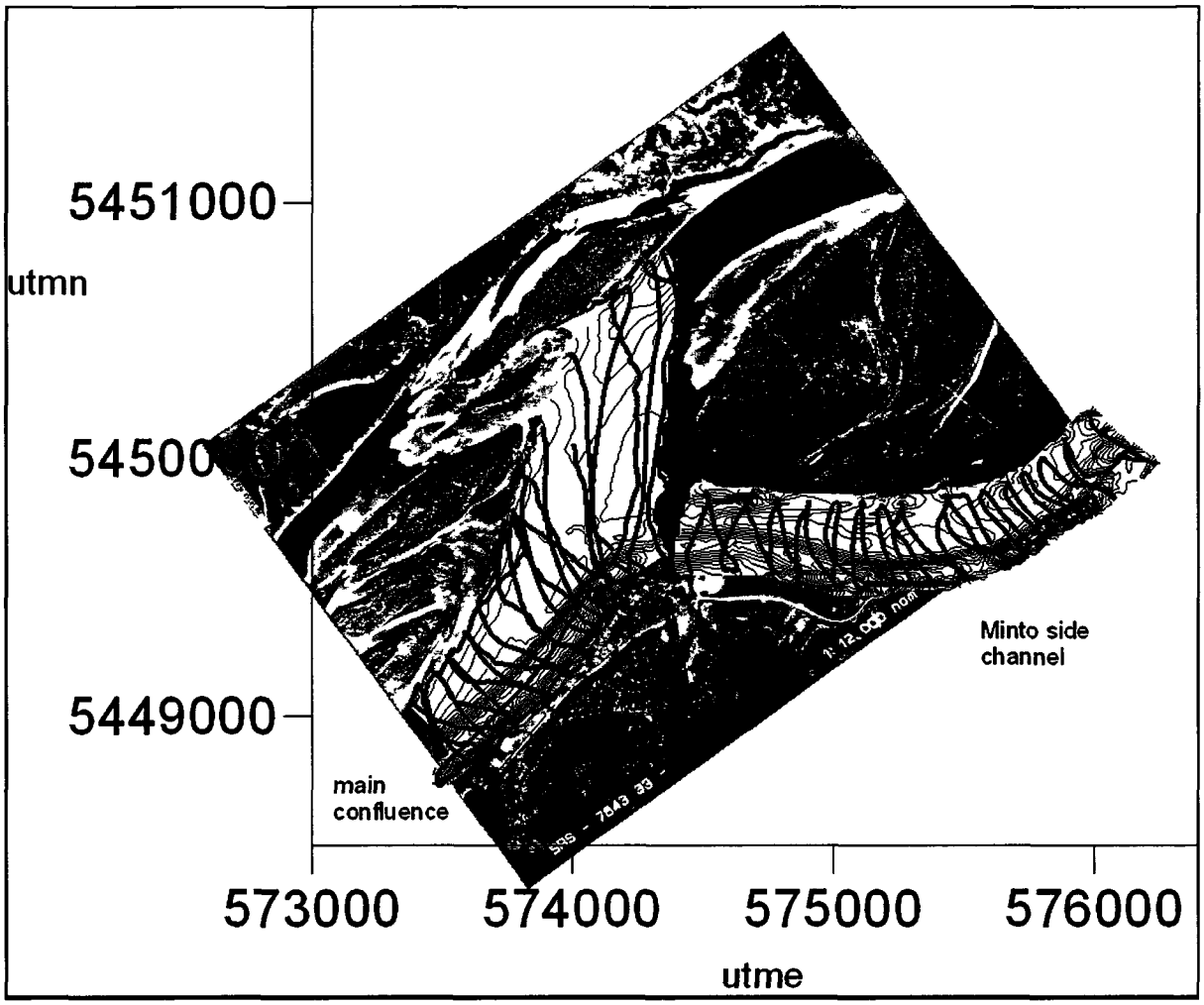

Figure 31 – aDcp Transects

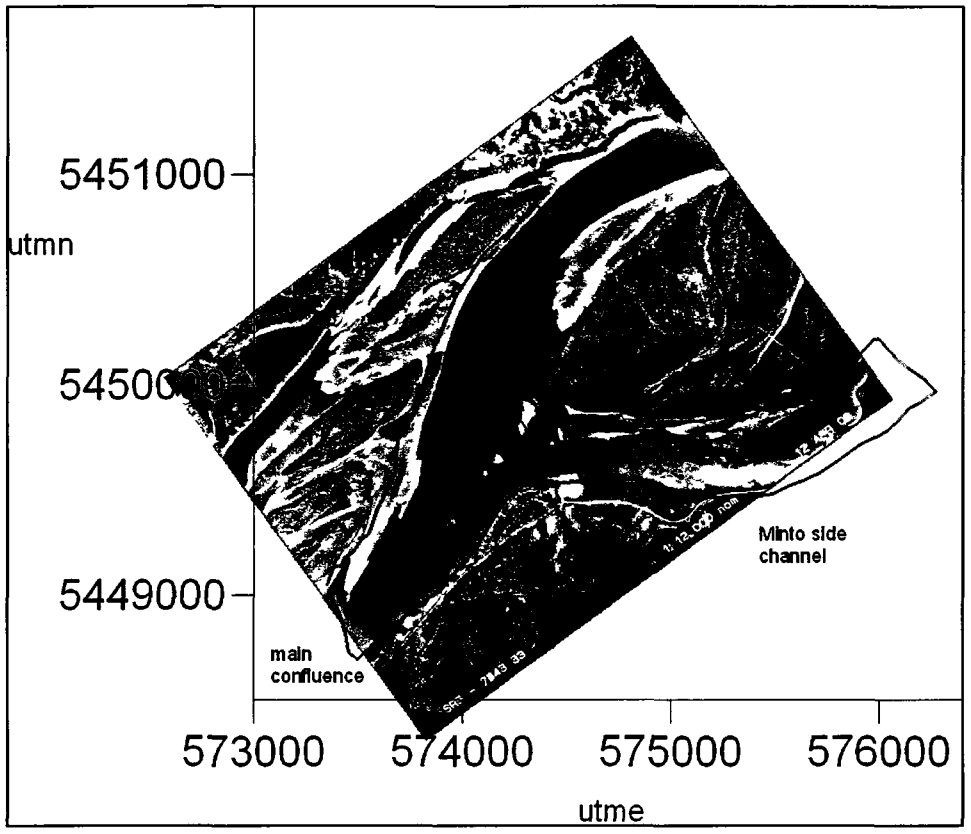

Figure 32 – 2008 Survey on 2008 Airphoto

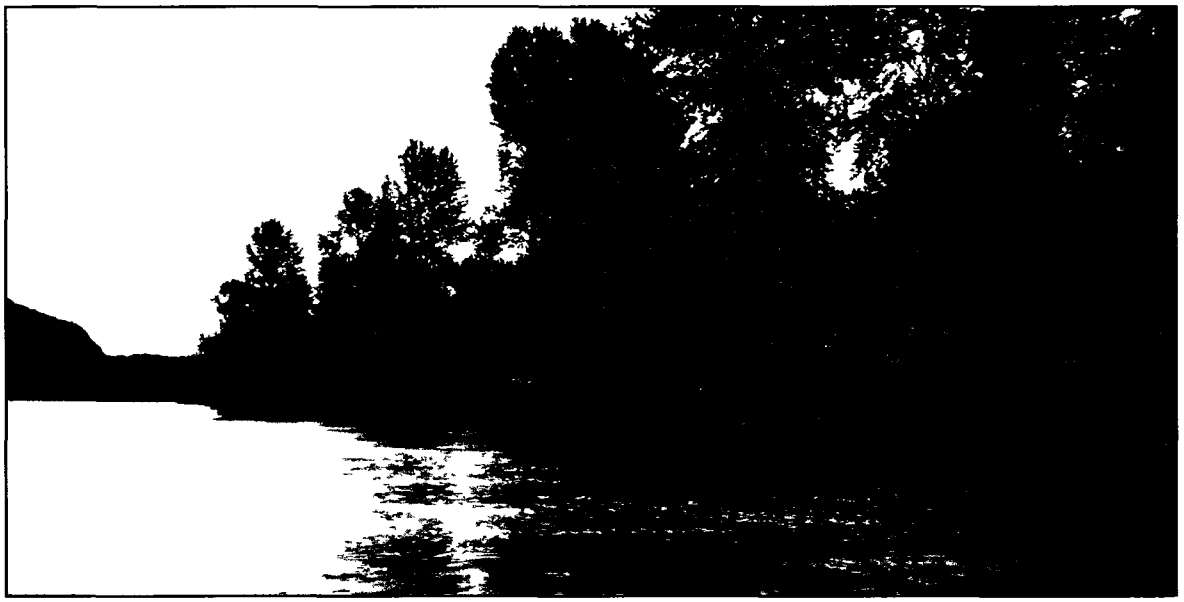

Figure 33 – Erosion at Upstream End of Left Bank

Figure 34 – Erosion and Riprap at Downstream End of Left Bank

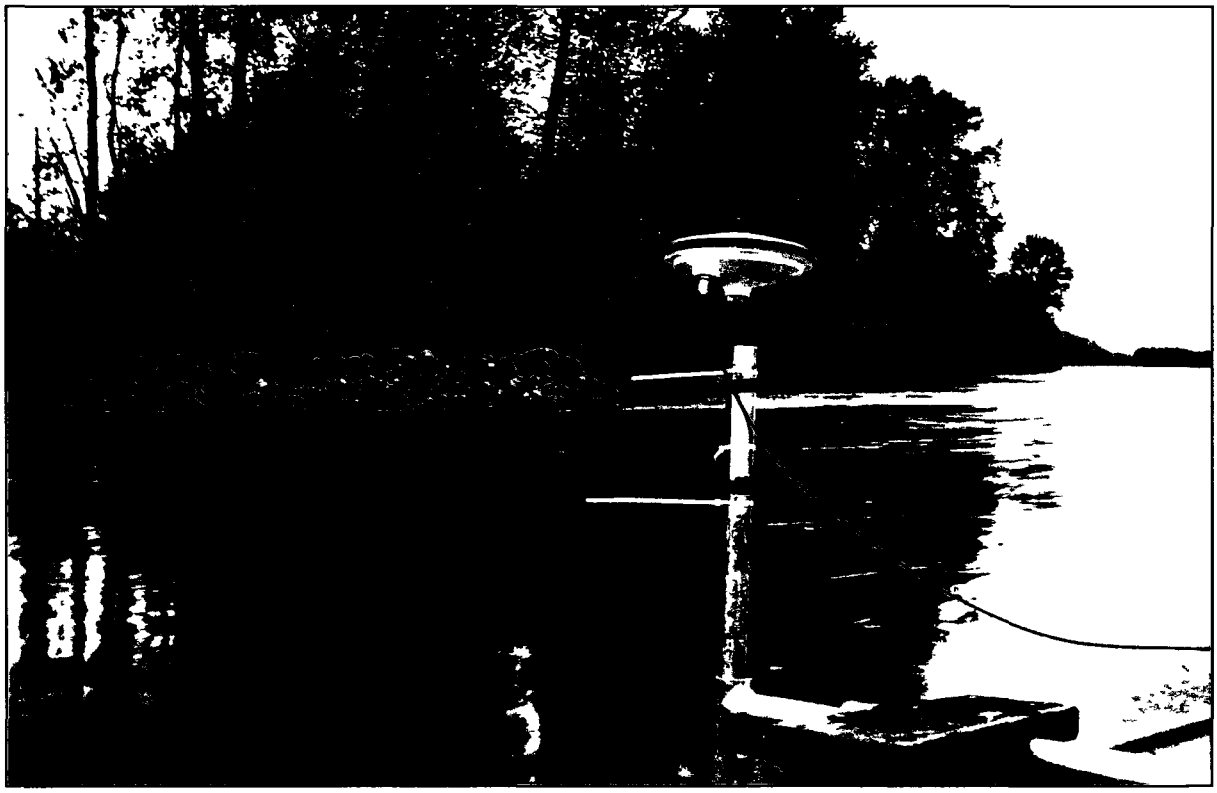

Figure 35 – Riprap at Downstream End of Left Bank

The bathymetry (figure 36) was produced by interpolating measured channel bed elevations using fitted semivariograms (figure 37) for ordinary kriging in the plotting software Surfer. The confluence bathymetry is shown in greater detail in figure 38. The sinuous thalweg paths are clearly visible from the bathymetry, moving from the right bank towards the left bank for the main confluence and moving from right bank to the left bank through the curve and back towards the channel centre before meeting the main channel flow for Minto side channel. Deep holes along the left bank of the upper half of Minto side channel are thought to be relics of previous gravel mining operations in the river. Thalweg riffles have depths of around 5 m and pools around 11 m. Deep scour, elongated in the downstream direction, is present along the left bank of the confluence area, with a maximum depth of 18 m at the upstream end (just downstream of the upstream riprap) and at the downstream end (opposite the downstream riprap) and a depth of 14 m in between. High bed slopes exist along the bed step flanking the right side of the deep confluence scour, ranging from 15° at the deep upstream pool to 10° at the deep downstream pool. High bed slopes also exist along the left bank beside the deep confluence scour, being about 10°, with a maximum of 20° at the deep downstream pool where the downstream gabion matting confines the flow. Deep scour holes, thought to result from past gravel mining of the river bed, are located in the bend of the Minto side channel. A small channel through Minto Island flows into the right side of Minto side channel where the Minto thalweg moves from the right to the left side of the channel. Another small channel through Minto Island is carving a small secondary flow path after it joins the downstream right bank of Minto side channel. Bed slopes of about 5° exist along the thalweg pools in both Minto side channel and the main channel. The width to depth ratio for Minto side channel is about 60 and that of the main confluence area about 70.

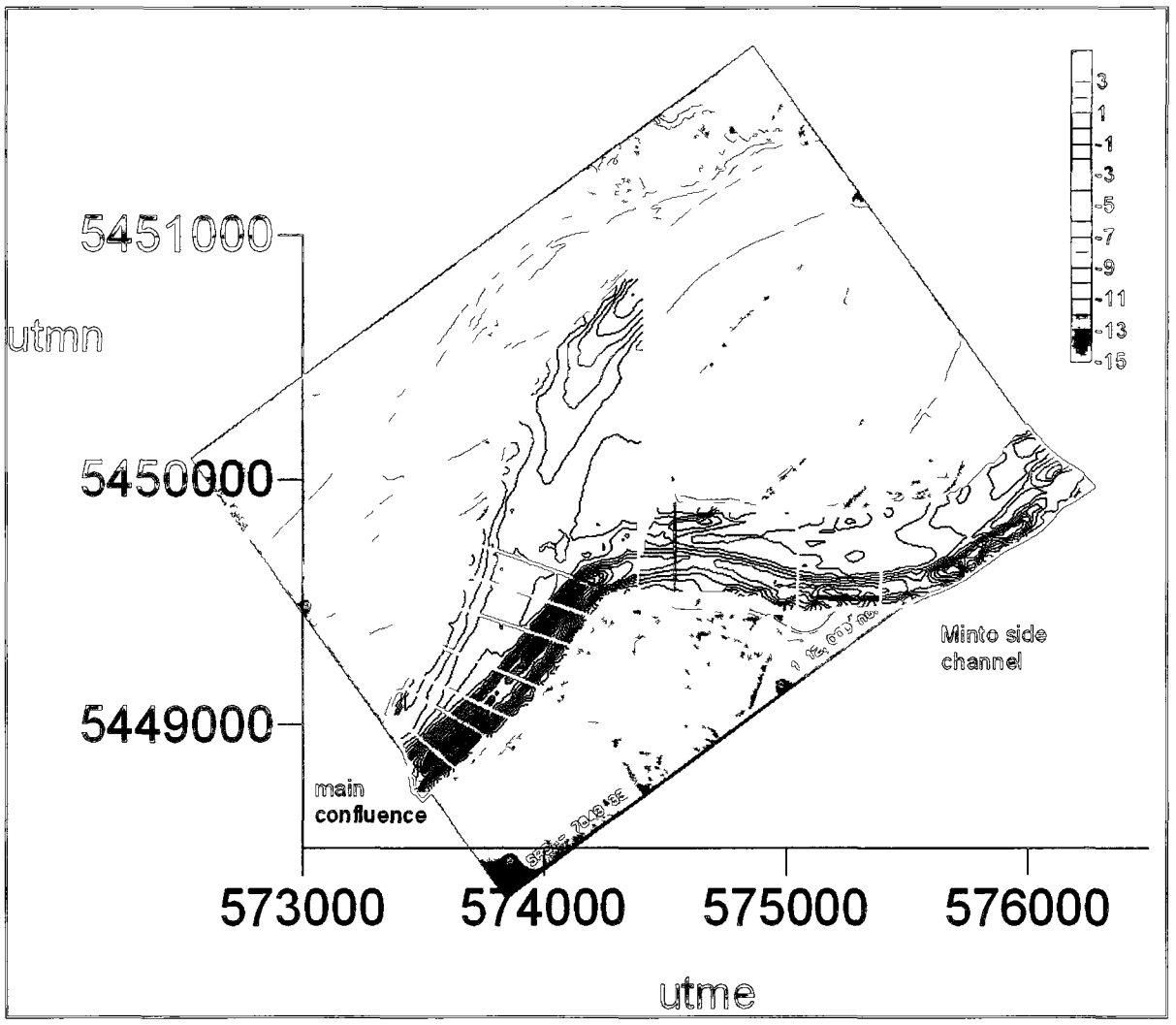

Figure 36 – Bathymetry

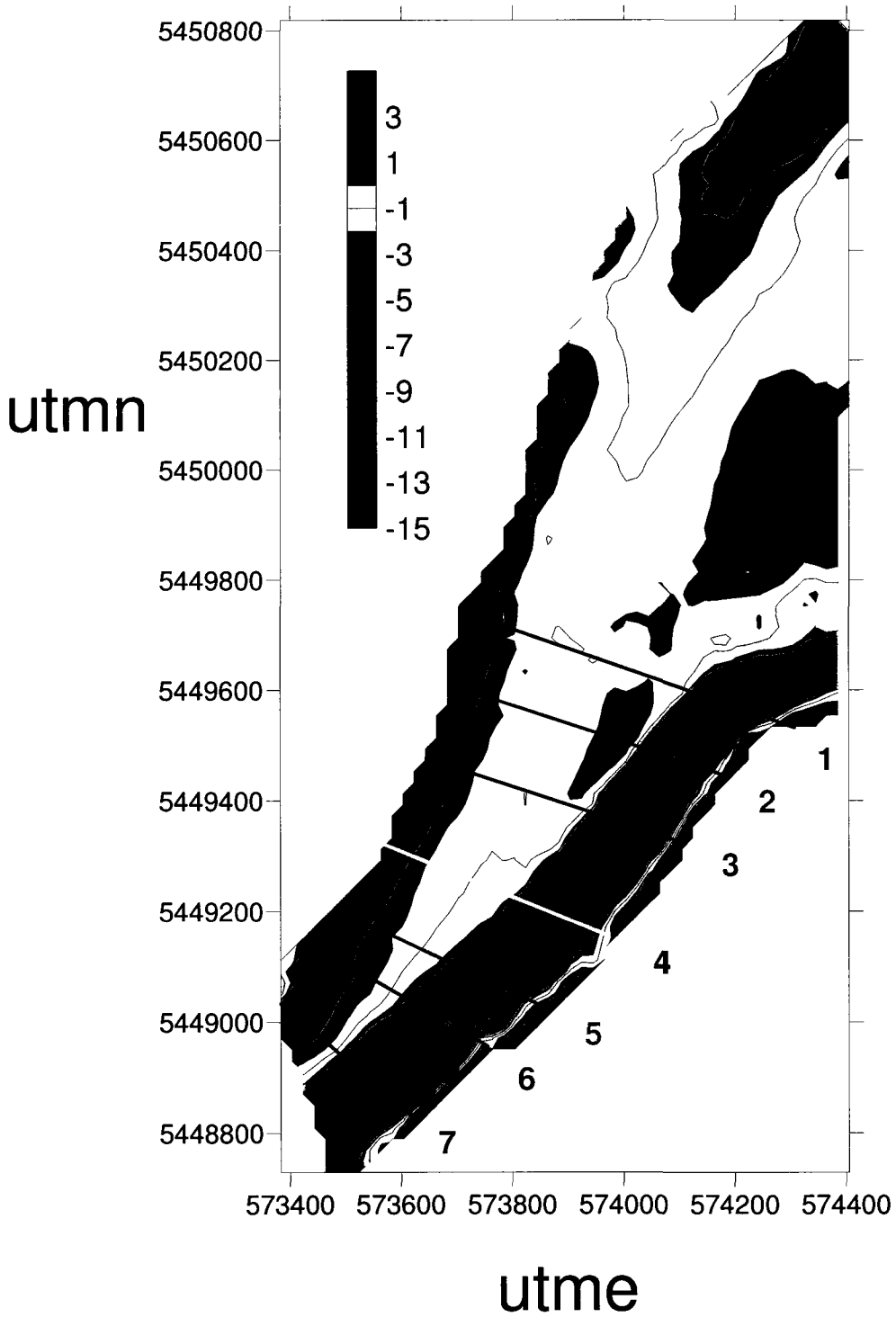

Figure 38 – Confluence Bathymetry

Methods

The measured Easting and Northing components of horizontal velocity were rotated into primary, or downstream, and secondary, or cross-stream, components according to the Rozovskii definition (Rhoads and Kenworthy, 1998). The Rozovkii definition has been used to identify secondary currents at large river confluences by Szupiany et al (2009), Szupiany et al (2007), and Parsons et al (2007). Secondary currents were identified by Lane et al (2008) in the large Parana/Paraguay River confluence by comparing the direction of bed and surface velocity vectors. Both approaches were investigated in this study. In addition, cross-section plots of the Easting, Northing, and vertical vectors tangential to the cross-sections, as used by de Serres (1999), were compared to the respective cross-section contour plots of primary, secondary and vertical velocities. Three-dimensional volumes of Easting, Northing, primary, secondary, and vertical velocities were produced by ordinary kriging in the software Tecplot, using a zero value of 0.05, a range of 0.3, no drift and using 12 nearest neighbour points. The main confluence volume consisted of a 20 m by 20 m grid in the East and North directions with 15 cells in the vertical, giving cells with a vertical dimensions ranging from around 1 m in the scour zone to 1/3 – 2/3 m for the rest of the confluence. The Minto side channel volume also consisted of a 20 m by 20 m grid in the East and North directions, but with 10 cells in the vertical, giving cells with a maximum vertical dimension of about 1 m in the deep holes. Vertical slices were extracted from the 3-D volume at progressive downstream cross-sections, from slice 1 to 7 through the main confluence, and from slice 8 to 10 in Minto side channel. Only the downstream half of the Minto side channel was used for results due to compass calibrations problems with the upstream half of the measured data (other than bathymetry which uses the average of the four beam depths and so is valid regardless of compass errors since GPS gives a correct boat location.) Vertical velocities, being much smaller, were filtered to retain only the bins where the vertical velocity was at least double the error velocity. Vertical GPS velocities were used to correct for vertical boat movement. These filtered vertical velocities were then interpolated

using ordinary kriging in Tecplot in the same manner as the horizontal velocities. Vertical slices and the near-bed layer were extracted to show details of the flow pattern.

The measured Easting and Northing components of bed velocity were similarly rotated to give the primary, or downstream, component according to the application of the Rozovskii definition (Rhoads and Kenworthy, 1998) to each flow profile for comparison with shear velocity. Interpolated two-dimensional plots of bed velocity vectors and primary bed velocity were produced using fitted semivariograms for ordinary kriging in Surfer. The locations of the vertical slices are shown.

The measured single transect flow velocity data were smoothed over 11 ensembles, or 5.5 seconds for a sampling frequency of about 2 Hz, to reduce random noise associated with temporal flow variability. Maximum boat velocity for the main confluence ranged from 1.5 – 2 m/s when travelling in the upstream direction and 3.5 – 4 m/s in the downstream direction, resulting in smoothing occurring over a maximum distance of about 10 m in the upstream direction and 20 m in the downstream direction. Maximum boat velocity for Minto side channel ranged from 1.5 – 2 m/s, resulting in smoothing over a maximum distance of about 10 m. The plots of primary, secondary, and shear velocity were calculated from the smoothed flow data.

Shear velocity was calculated from applying the log law of the wall to each individual vertical velocity profile. The log law of the wall is considered to be strictly applicable only to the lowest 20% of the flow depth, although it has often been found to fit the velocity profile of the entire flow depth (Nezu and Nakagawa, 1993). It was fitted to the entire profile for Minto side channel, and to the lowest 20% of the flow profile (minus the bottom 6% lost to side lobe interference) for the main confluence area where plunging flow was present. Shear velocity values were calculated using the formulation of the log law of the wall using the average of the primary velocity and the depth for the selected profile bins and the roughness value estimate (eq. 14),

which was determined to give the most repeatable estimate for moving boat single transect measurement (Sime et al, 2007). An assessment of shear velocity estimation in the study reach is presented in the Discussion section. Interpolated two-dimensional plots of shear velocity were produced using fitted semivariograms for ordinary kriging in Surfer.

Results

The downstream slope of the water surface was determined to be 0.0004 in the main confluence area and 0.0002 in Minto side channel. The water surface elevation is about 5 m.a.s.l. at the upstream end of the main channel in the confluence area, and about 4 m.a.s.l. at the downstream end. The water surface elevation is about 4.5 m.a.s.l. where Minto side channel joins the confluence area. The interpolated primary velocity volumes for the main confluence and Minto side channel are shown in figure 39. The vertical dimension has been exaggerated to better display the flow patterns (1:1:10 for x:y:z). The details of the flow are examined at labelled vertical cross-sections through the main confluence flow, sections 1-7, and Minto side channel flow, sections 8-10. The thalweg in the main channel is clearly visible, moving from the right bank at the upstream end to the left bank at the downstream end, with flow acceleration and the highest velocities, about 3.5 m/s, occurring at the upstream and downstream channel bends. The thalweg in Minto side channel also clearly moves from the right bank at the upstream end to the left bank at the downstream end, where flow is deflected by the sediment deposition downstream of Minto island and accelerated along the left bank with the highest velocities, about 3 m/s, occurring as the flow enters the confluence area at section 1.

The interpolated secondary velocity volumes for the main confluence and Minto side channel are shown in figure 40. Positive secondary velocity is directed towards the left bank and negative secondary velocity is directed towards the right bank. The position of the mixing interface is evident at the surface along the left bank of the confluence, where the highest secondary component, about -0.5 m/s, of the left bank flow is directed towards the main channel, and that of the main channel flow, about 0.5 m/s, is directed towards the left bank flow. Limited secondary flow exists in Minto side channel between sections 8 and 9, occurring where the thalweg moves from the right bank to the left bank.

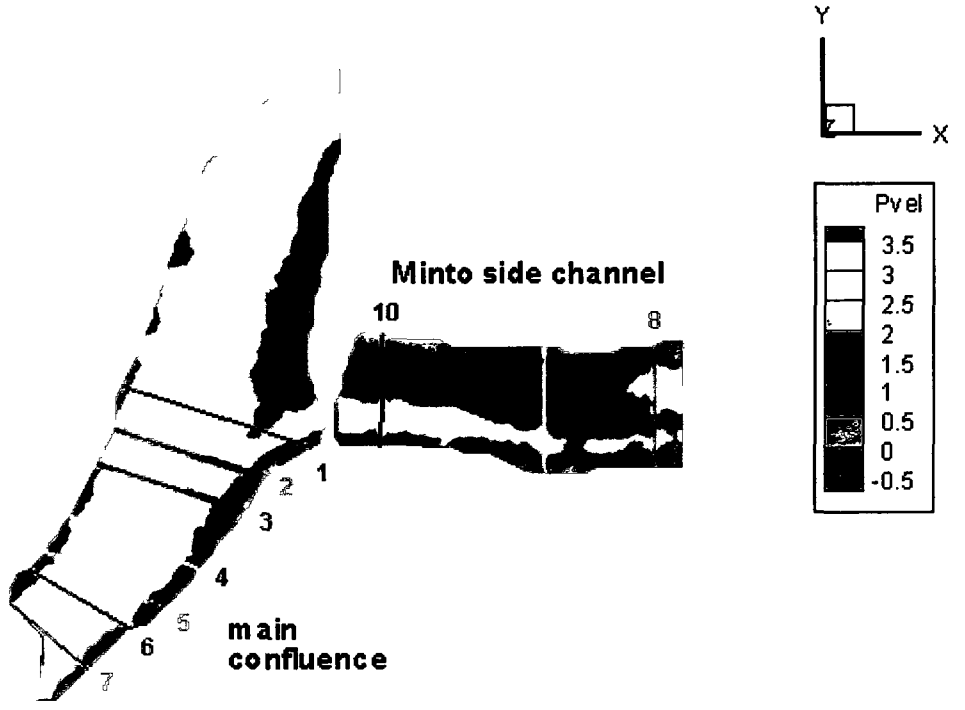

Figure 39 – Primary Velocity (m/s)

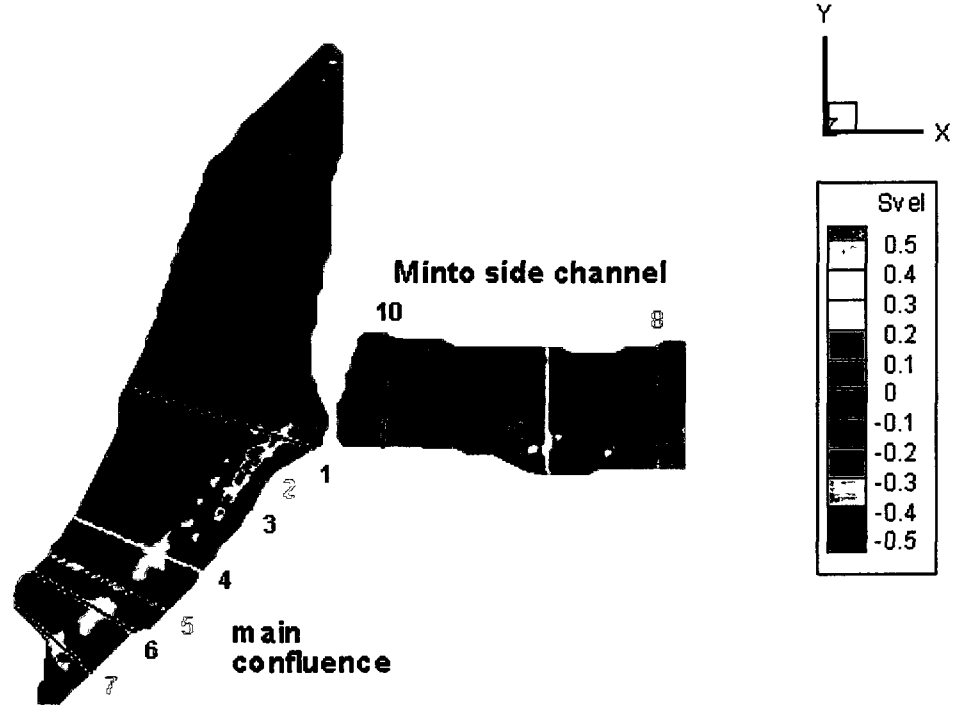

Figure 40 – Secondary Velocity (m/s)

The interpolated primary bed velocity is shown in figure 41. Primary bed velocity follows the path of the thalweg along the main channel, with the highest values about 0.15 m/s in the upstream scour hole where the Minto flow enters the confluence and in the downstream end of the confluence. Intermediate bed velocities in Minto side channel, up to 0.1 m/s, are located in the vicinity of the gravel mining holes along the left bank, between sections 8 and 9, and along the outer bends of the two curved flow paths present around section 10.

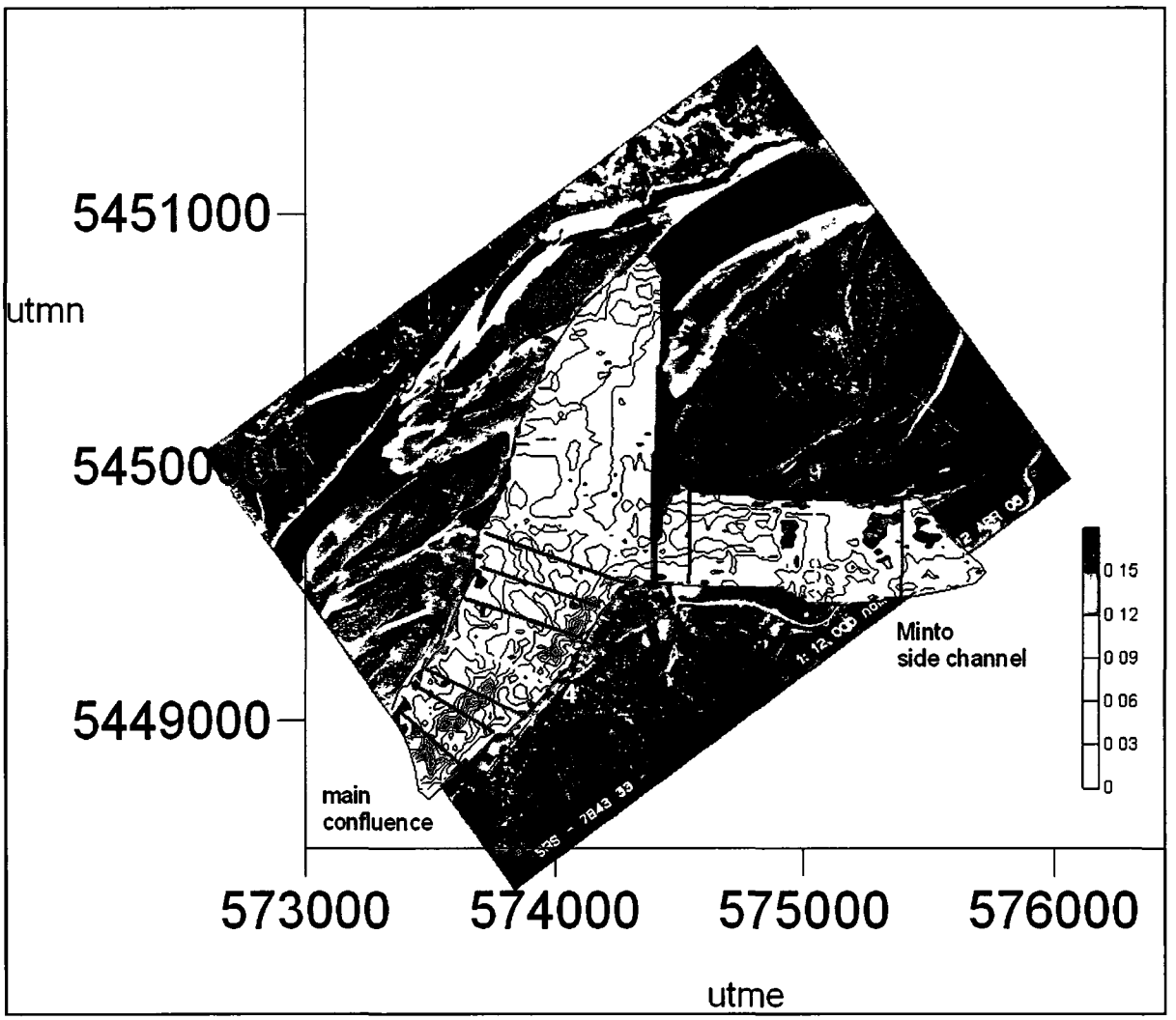

Figure 41 – Primary Bed Velocity (m/s)

The plot of interpolated bed velocity vectors is shown in figure 42. Bed velocity vectors generally follow the direction of the channel thalweg, both in the main confluence and Minto side channel, with the highest values of about 0.2 m/s in the main confluence and 0.1 m/s in Minto side channel. In the main channel riffle upstream of the confluence, the bed velocity vectors are directed towards Queen Islands; it is proposed that the bed velocity in this area is following the general downstream direction since flow permeates through the mid-channel islands. Bed velocity vectors clearly show bed movement around the edges of the deep scour hole in the confluence, and along the outer edges of the thalweg bends in both the main channel and Minto side channel.

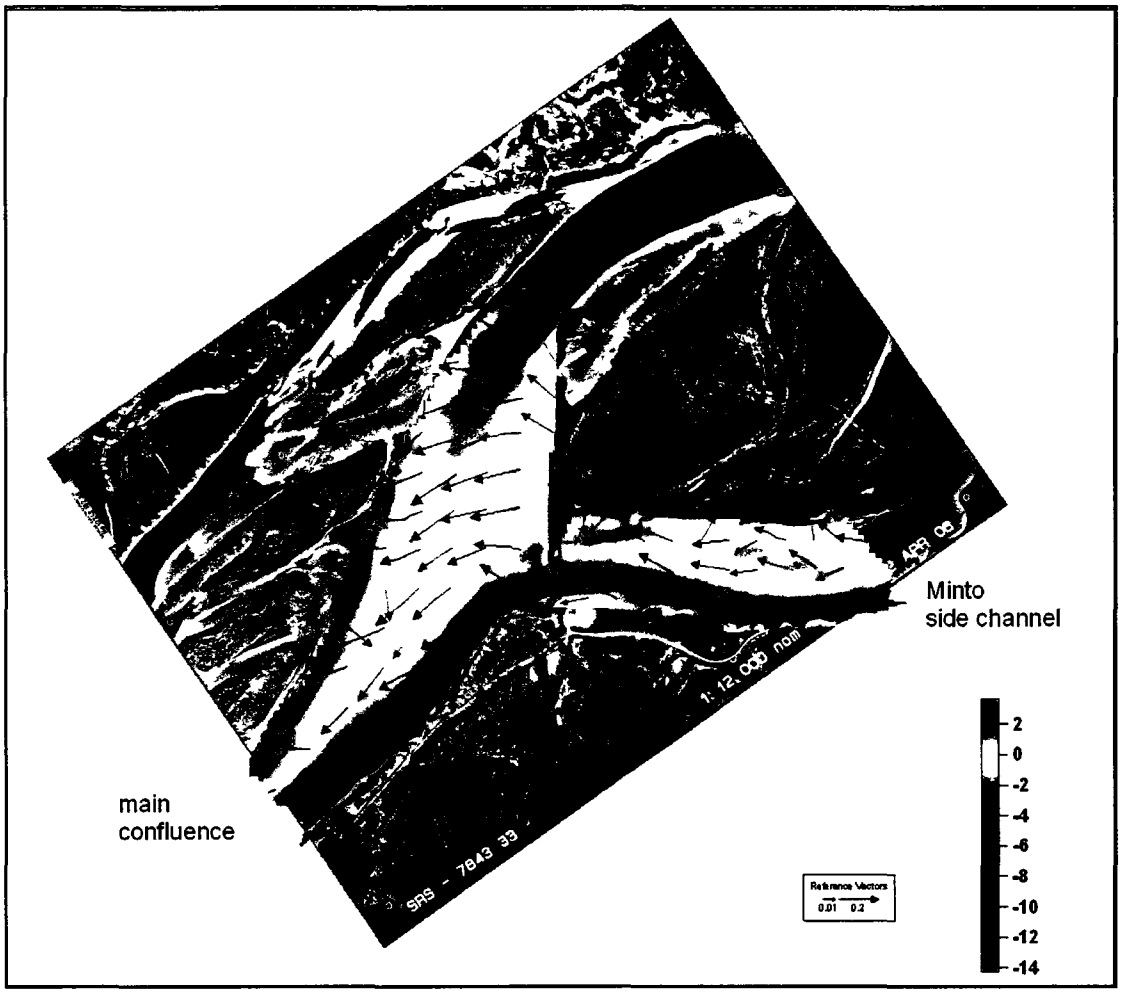

Figure 42 – Bed Velocity Vectors (m/s)

Main Confluence

The general flow pattern through the confluence is displayed in the plot of superimposed near bed and surface velocity vectors at each cross-section (figure 43). The surface Minto flow entering the confluence at section 1 is moving towards the mixing interface while the flow near the bed is directed downstream. At sections 2, 3, and 4, the flow on both sides of the mixing interface is moving towards it at the surface and away from it near the bed. The flow above the bed step is moving towards the left bank at the surface and in the downstream direction near the bed in the downstream sections, 5, 6, and 7.

The flow pattern through the confluence is detailed through progressive vertical cross-sections 1 to 7 in the downstream direction, oriented perpendicular to the mixing interface, showing the primary, secondary, vertical, and tangential velocity vectors plotted on primary velocity contours (figures 44-50). The high velocity core of Minto side channel plunges to the bottom of the scour hole upon entering the confluence area, while that of the main channel moves further left towards the confluence scour hole. The main channel high velocity core then drops into the scour hole and joins the Minto high velocity core to form a single coherent flow. The plots of secondary and vertical velocities and the tangential velocity vectors show the location of the vertical mixing interface between the two helical flow cells where flow is advected downwards in the upstream part of the scour zone; weaker helical flow is evident in the main channel flow as it confines the strongly helical left bank flow. In the downstream part of the confluence, once the high velocity cores have joined, the helical cells have dissipated, but very strong downward velocity exists along the left bank at the downstream end where the riprap confines and accelerates the flow.

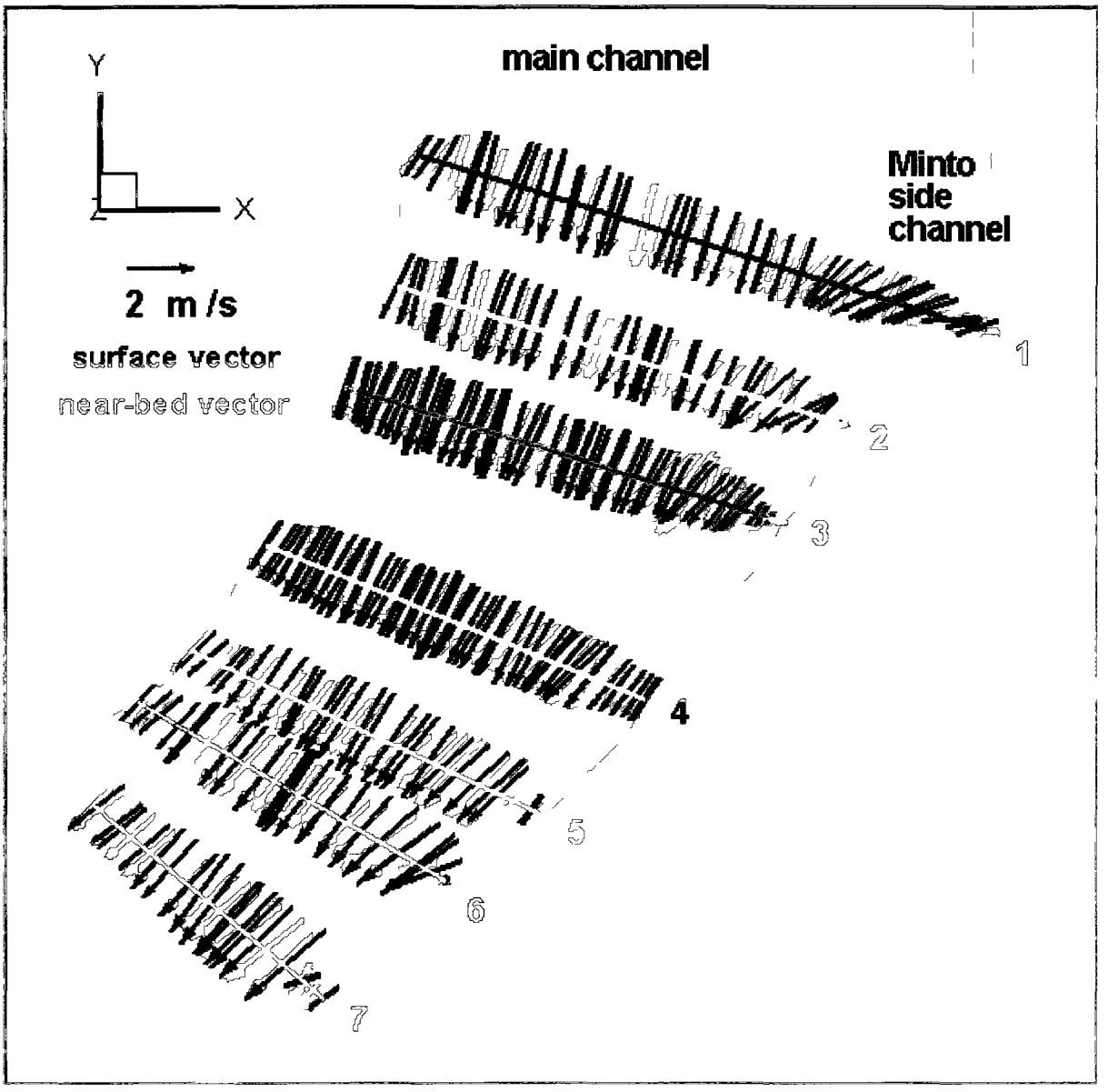

Figure 43 – Main Confluence Surface and Near Bed Velocity Vectors

The primary velocity plot in section 1 (figure 44) clearly shows the two high velocity cores, at the surface of the main channel and of Minto side channel. The plot of secondary velocity shows near-surface flow directed towards the mixing interface and near-bed flow directed towards the left bank. The plot of vertical velocity shows

downward flow at the mixing interface and upward flow next to the left bank. The start of the helical pattern in the Minto flow is evident in the plot of tangential velocity vectors, with flow moving strongly towards the mixing interface at the surface and downwards at the mixing interface. The Minto flow entering the confluence is is helical due to planform curvature. This helicity is accentuated by the acceleration of the Minto flow due to its lateral confinement by the main channel flow, with cross-sectional area of the Minto flow reducing 6% between sections 1 and 2 and 14% between sections 2 and 3 despite the deepening of the scour hole.

The primary velocity plot in section 2 (figure 45) shows the Minto high velocity core plunging into the deepening scour hole. Strong helical flow is evident on the left side of the confluence, with the highest values for secondary and vertical velocities following the same pattern as described for section 1. Secondary velocities range from 0.5 to -0.5 m/s and vertical velocities range from 0.3 to -0.3 m/s. A weak partial helical pattern starts to develop on the main channel side of the mixing interface, with flow directed towards the mixing interface near the surface, downwards at the mixing interface, away from the mixing interface near the bed and upwards across the bed step. Both the stronger helical pattern to the left of the mixing interface and the start of the helical pattern to the right of the mixing interface are visible in the plot of tangential velocity vectors.

The primary velocity plot in section 3 (figure 46) shows the Minto high velocity core accelerating along the bottom of the scour hole, with velocities over 3 m/s. Strong helical flow is still evident along the left side of the confluence, with high values for secondary and vertical velocities following the same pattern. The partial helical pattern on the main channel side of the mixing interface strengthens but is still weak when compared to that on the left side. The helical cells on both sides of the mixing interface are clearly visible in the plot of tangential velocity vectors, with the stronger cell to the left of the mixing interface.

Section 1

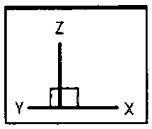

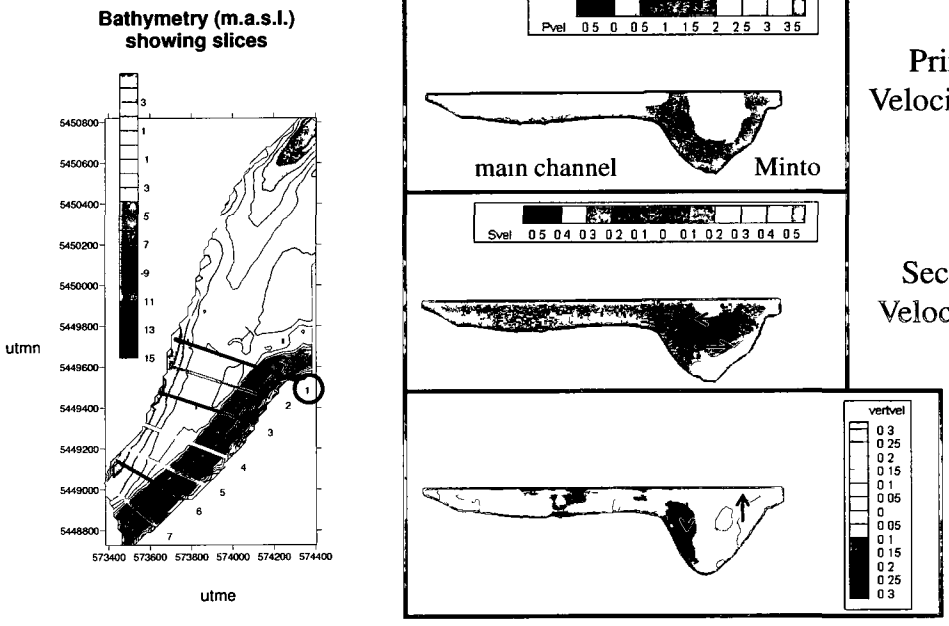

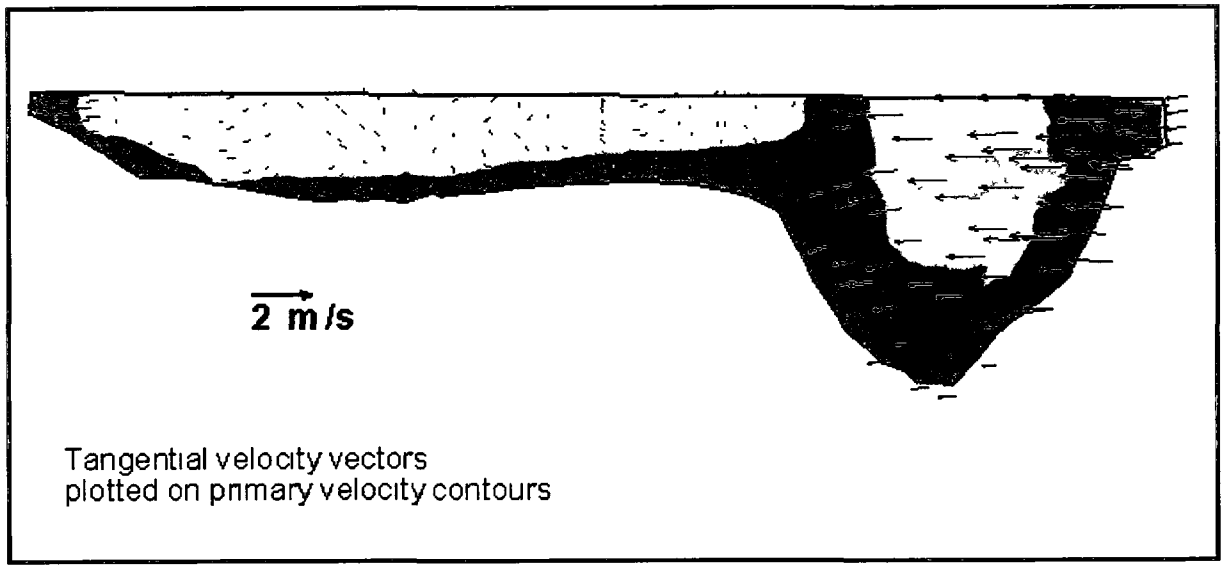

Figure 44 – Section 1 Flow Velocities, viewed from downstream

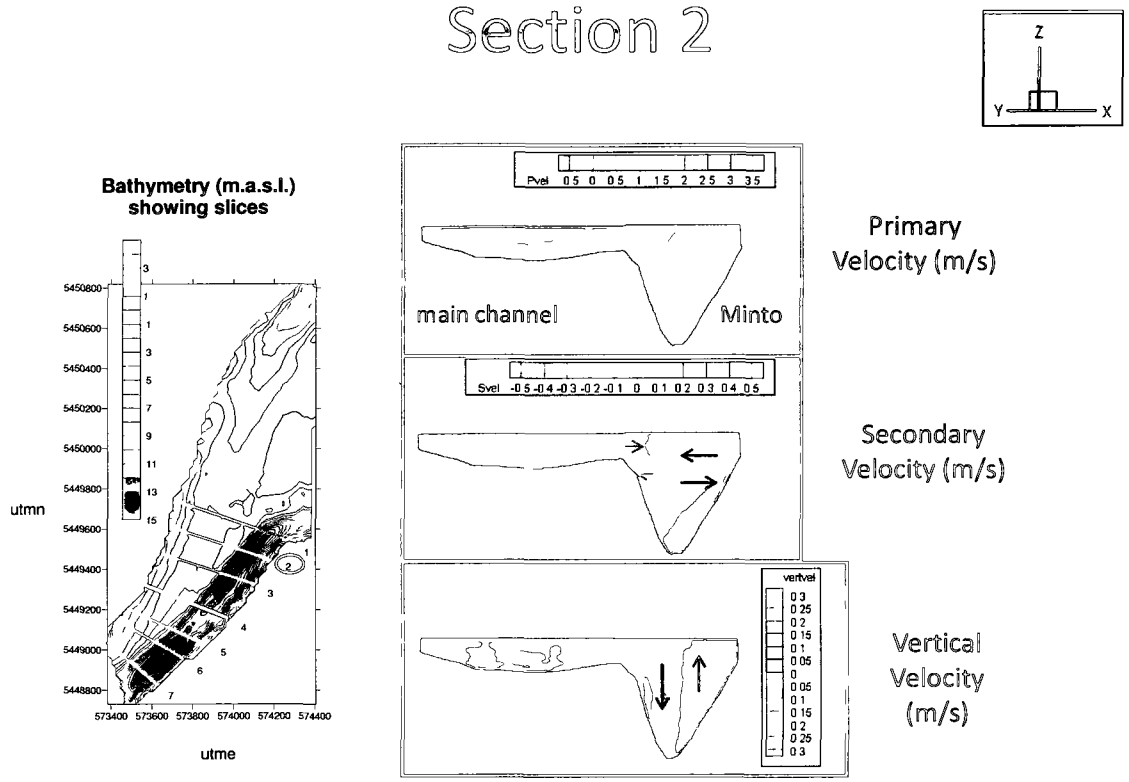

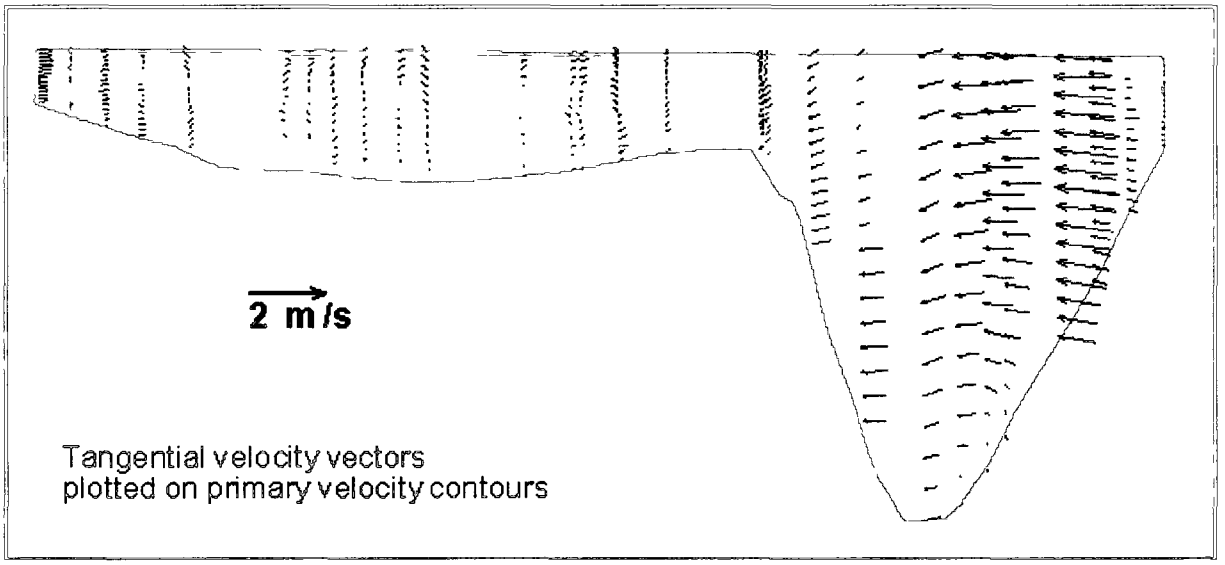

Figure 45 – Section 2 Flow Velocities, viewed from downstream

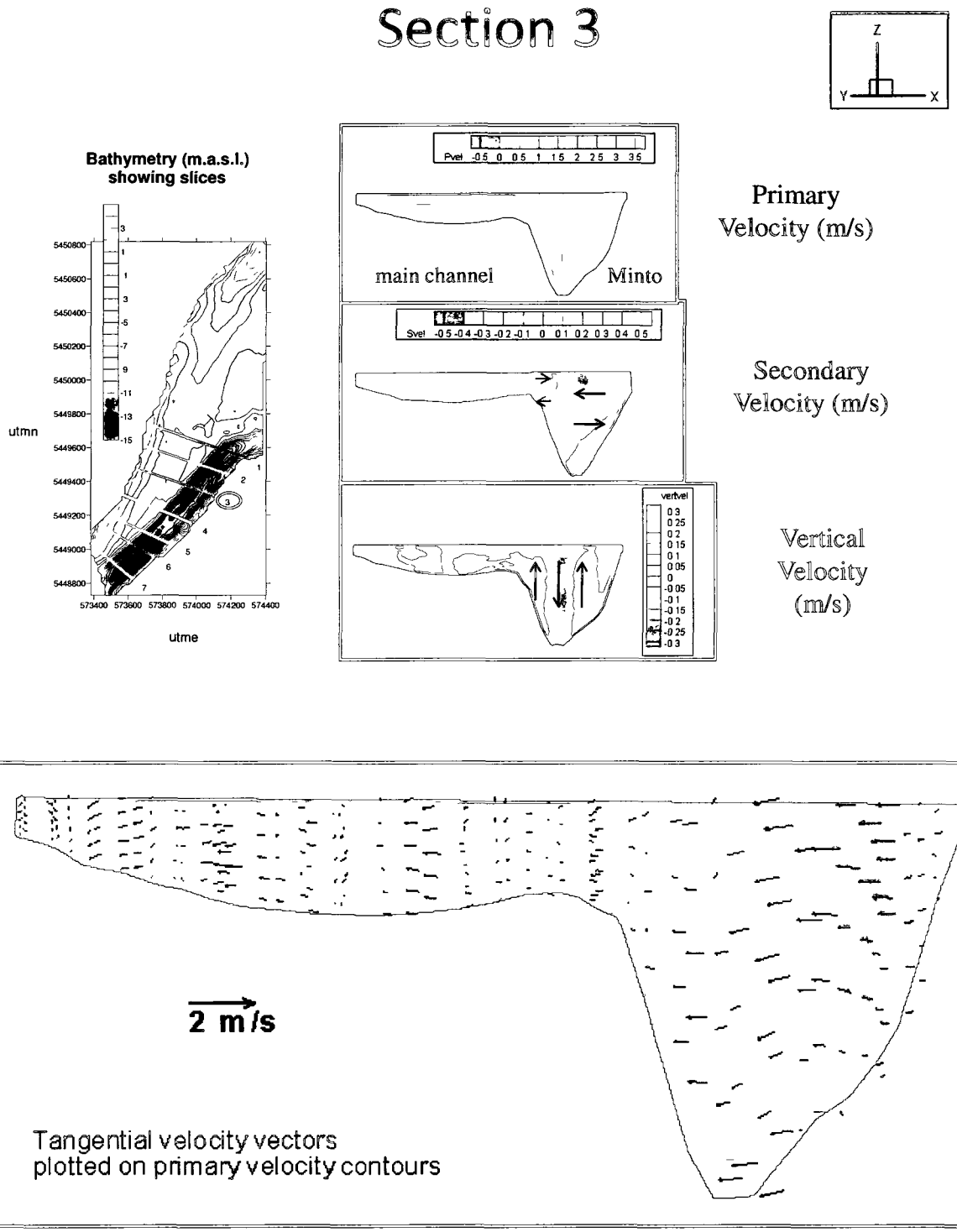

Figure 46 – Section 3 Flow Velocities, viewed from downstream

The primary velocity plot in section 4 (figure 47) shows the main channel high velocity core reaching the mixing interface at the surface, while the Minto high velocity core is still located near the bottom of the scour and expands a little with maximum velocities dropping below 3 m/s again. The helical flow cells decay considerably; downwards flow persists at the mixing interface with upwards flow on either side of it still evident in the vertical velocity plot, although the secondary velocities have dissipated. The weakening of both helical flow cells is evident in the plot of tangential velocity vectors.

The primary velocity plot in section 5 (figure 48) shows the main channel high velocity core having moved over and down to join the Minto high velocity core in the scour. Secondary velocities have dissipated, however upward vertical velocity exists at the right edge of the bed step and downward velocity exists where the main channel core is joining the Minto core underneath it. Weakly helical floe is visible above the right edge of the bed step in the plot of tangential velocity vectors, while flow along the left bank is uniformly directed at an angle downwards and towards the right bank.

Section 6 (figure 49) is located just where the channel width is constricted by the start of the downstream riprap. The primary velocity plot shows velocities above 3 m/s where the flow is accelerating in the upper two-thirds of the high velocity core in the scour hole, with the combined high velocity core nearly extending across the entire cross-section. Strong downward velocities exist adjacent to the riprap along the left bank where the flow is constricted, visible in the both the vertical velocity plot and the plot of tangential velocity vectors. The tangential velocity vectors in the scour hole are still fairly uniformly directed at an angle downwards and towards the right bank.

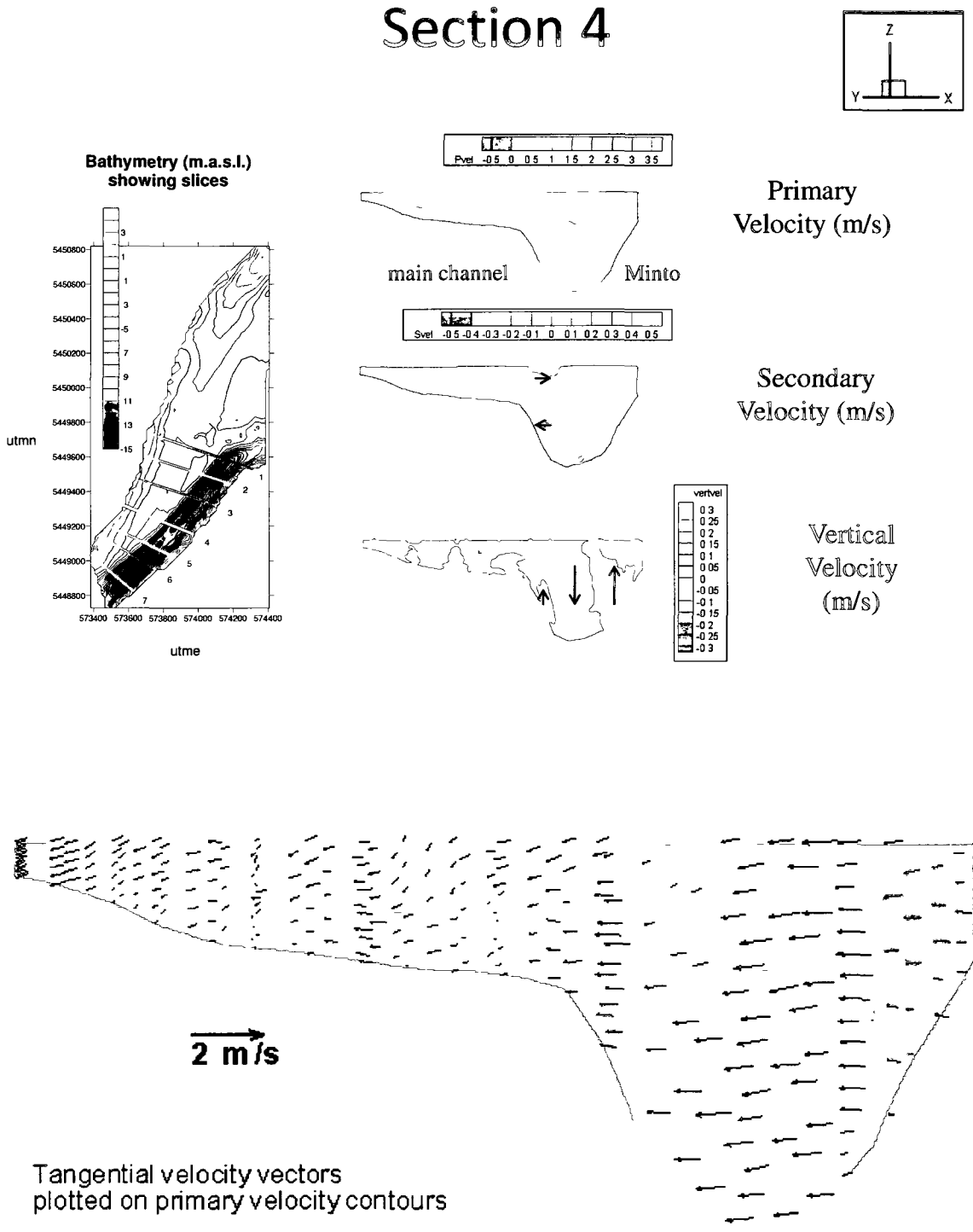

Figure 47 – Section 4 Flow Velocities, viewed from downstream

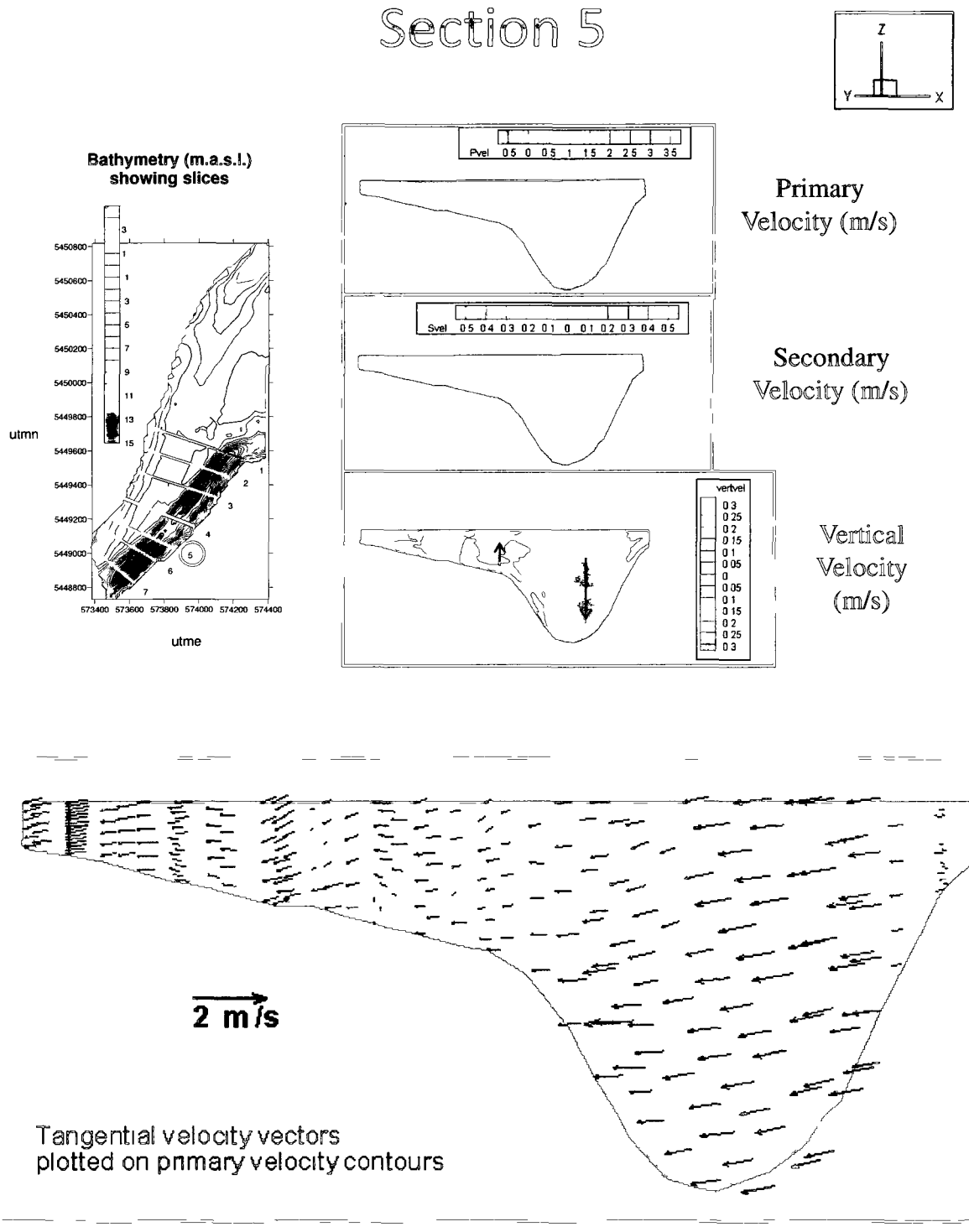

Figure 48 – Section 5 Flow Velocities, viewed from downstream

Section 6

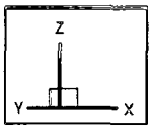

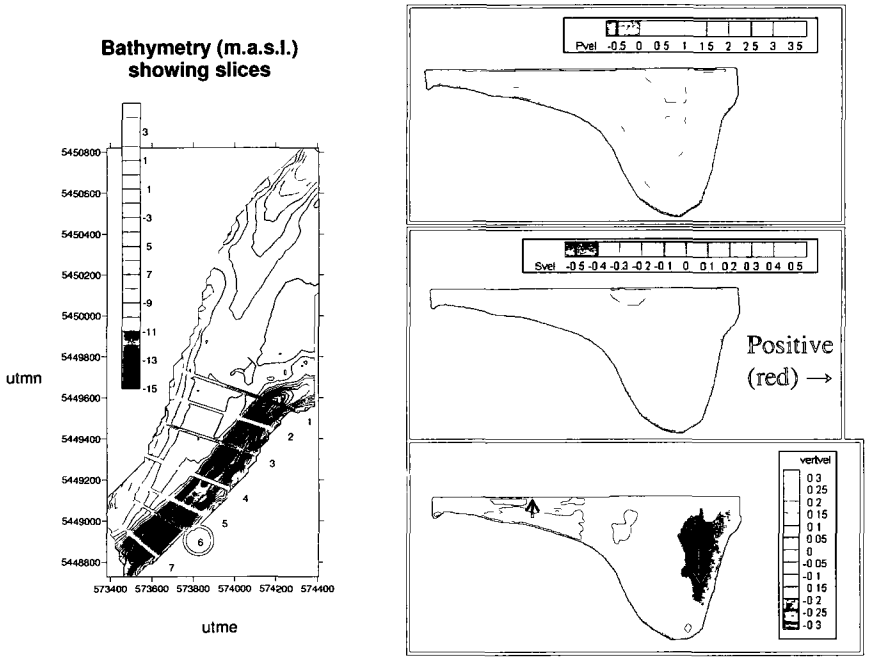

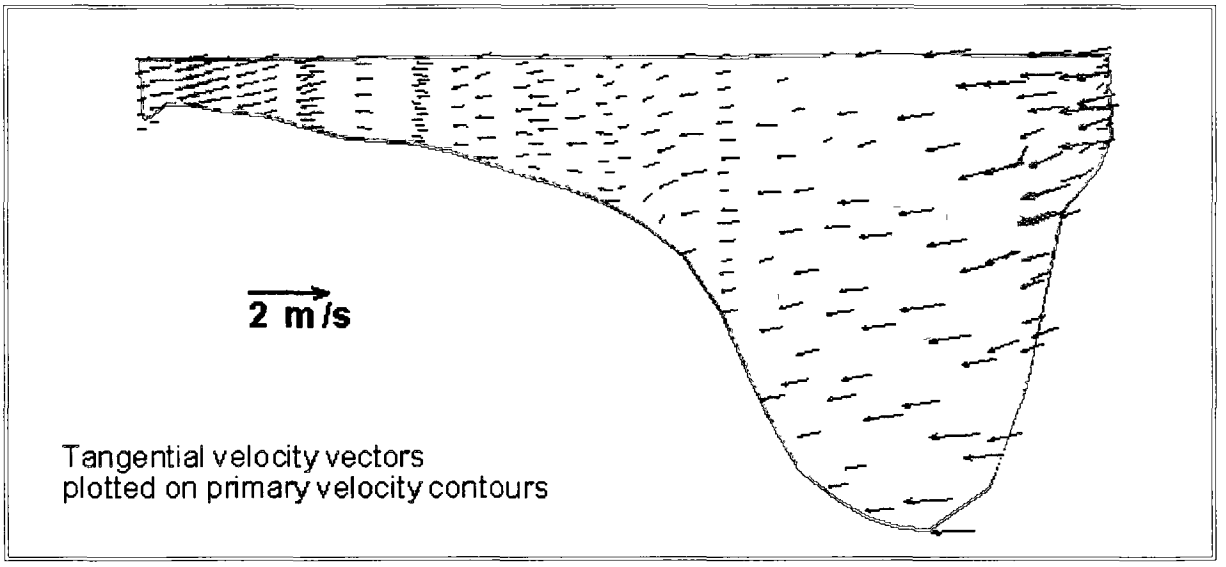

Figure 49 – Section 6 Flow Velocities, viewed from downstream

Section 7 (figure 50) is located at the start of the downstream main channel bend, and displays typical channel bend pool geometry and accelerating high velocity core. One quarter of the channel flow has primary velocities over 3 m/s, with the high velocity core extending from the surface to the bottom of the deep scour. The vertical velocity plot shows some flow separation from the bank, with the downward velocity shifted somewhat into the channel and upward velocity existing right next to the bank. The primary velocity is also much lower near the bank, where a clear vertical boundary shows in the primary velocity plot. The plot of the tangential velocity vectors clearly shows the flow separation and upwards vectors at the left bank, and the start of a single helical cell in the coherent flow entering the downstream bend in the main channel thalweg, with flow directed downwards in the high velocity core near the left bank and then towards the right side of the scour hole.

A complete helical cell develops in the confined flow left of the mixing interface, evident from section 1, and a weaker partial helical cell develops in the main channel flow between the elongated bed step and the mixing interface, evident from section 2. The back-to-back helical cells dissipate as the high velocity cores merge, the cell to the left of the mixing interface has dissipated by section 5 and the cell to the right of the mixing interface has dissipated by section 6. A single partial helical cell starts to develop at section 7 once the high velocity cores have merged at the downstream bend of the main channel. This pattern of back-to-back full and partial helical cells and a vertical mixing interface at the beginning of the confluence, limited in width to the scour zone and to where the high velocity cores are separate, was also identified at confluences A and B downstream of mid-channels islands along the Parana River (Szupiany et al, 2009). A morphological pattern developed at confluence B that was very similar to that at the Fraser River confluence; a very deep scour hole existed under the mixing interface and erosion occurred along the left bank, where the left tributary flow was confined and accelerated between the mixing interface and the left bank. The slow mixing case of the Parana/Paraguay confluence exhibited a vertical mixing interface, and partial helical cells limited to the region around the bed step

Section 7

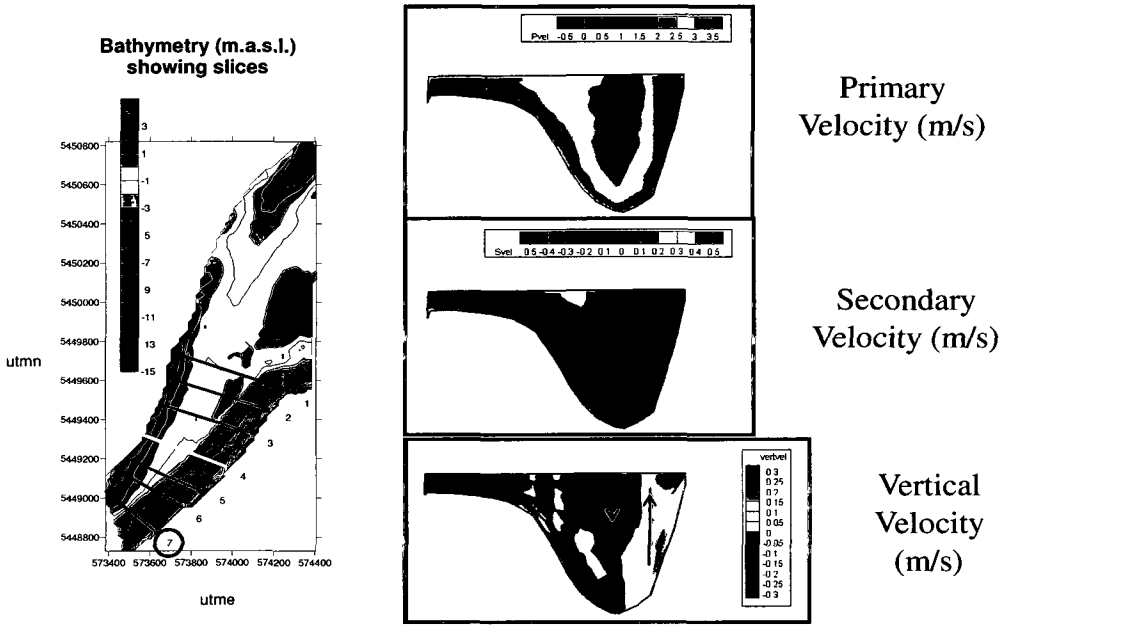

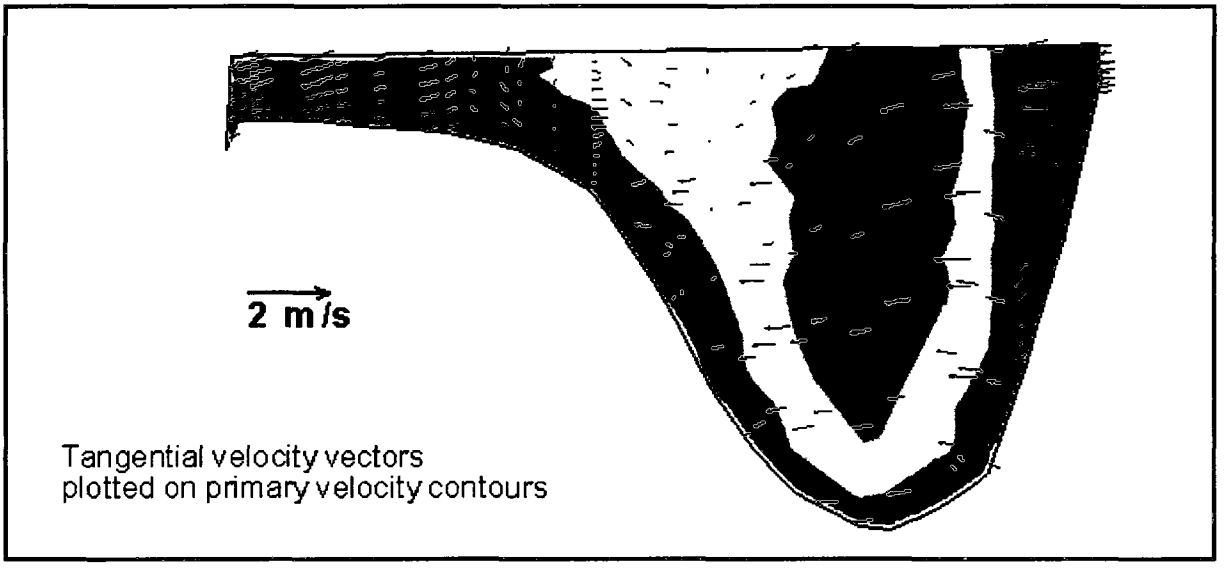

Figure 50 – Section 7 Flow Velocities, viewed from downstream

and mixing interface (Lane et al, 2008). The high width to depth ratios of these reaches, around 70 for the Fraser River confluence and around 100 for the Parana River confluences, may account for helical flow development being limited to the scour zone. It was proposed that the absence of secondary circulation at the low-angle sand-bed confluence-diffluence unit along the Parana River (Parsons et al, 2007) was due to the bed roughness for flow, over the dune bed at a width to depth ratio around 200, inhibiting any secondary flow development. Channel-wide back-to-back helical cells and a vertical mixing interface were reported by Rhoads and Kenworthy (1998), for the small Kaskaskia River-Copper Slough confluence with a width to depth ratio less than 5.

The primary bed velocity, near-bed vertical velocity, and shear velocity for the main confluence, with the bathymetry for reference, are compared in figure 51. The primary bed velocity and the shear velocity are shown both in 3D, mapped on the bathymetry, and in 2D to show detail. The shear velocity, again, is calculated from the primary flow velocities, with a maximum of 0.2 m/s (corresponding to a bed shear stress of 40 N/m^2).

The primary bed velocity generally follows the thalweg, where the shear velocity values are also high. The largest area of high primary bed velocity values occurs along the elongated bed step, from section 3 – 7, while the shear velocity is similarly high from section 4 – 7. The second area of high primary bed velocity occurs along the bank-side edges of the deepest upstream and downstream scour holes under the mixing interface, from section 2 – 4 and from section 5 – 7. The shear velocity values are high in the deepest path through the scour, which is under the mixing interface and where consistent downward vertical velocities exist. However, strong upward vertical velocities exist near the bed along the bank-side edges of the deepest upstream scour where the primary bed velocity is high. This pattern of highest primary flow velocities and shear velocities occurring in the deepest part of the scour while the bed-load transport occurs along the edges of the scour has been identified by Szupiany et al (2009) and Boyer et al (2006). Church (1987) referred to an early

sediment transport study along the Inn River, conducted by Muhlhofer in 1933, where the highest sediment transport occurred on the bar face flanking the scour hole. These maps of primary bed velocity, near-bed flow velocity and shear velocity show consistency, with areas of high primary bed velocity matching areas of high shear velocity and/or strongly upward vertical flow velocity.

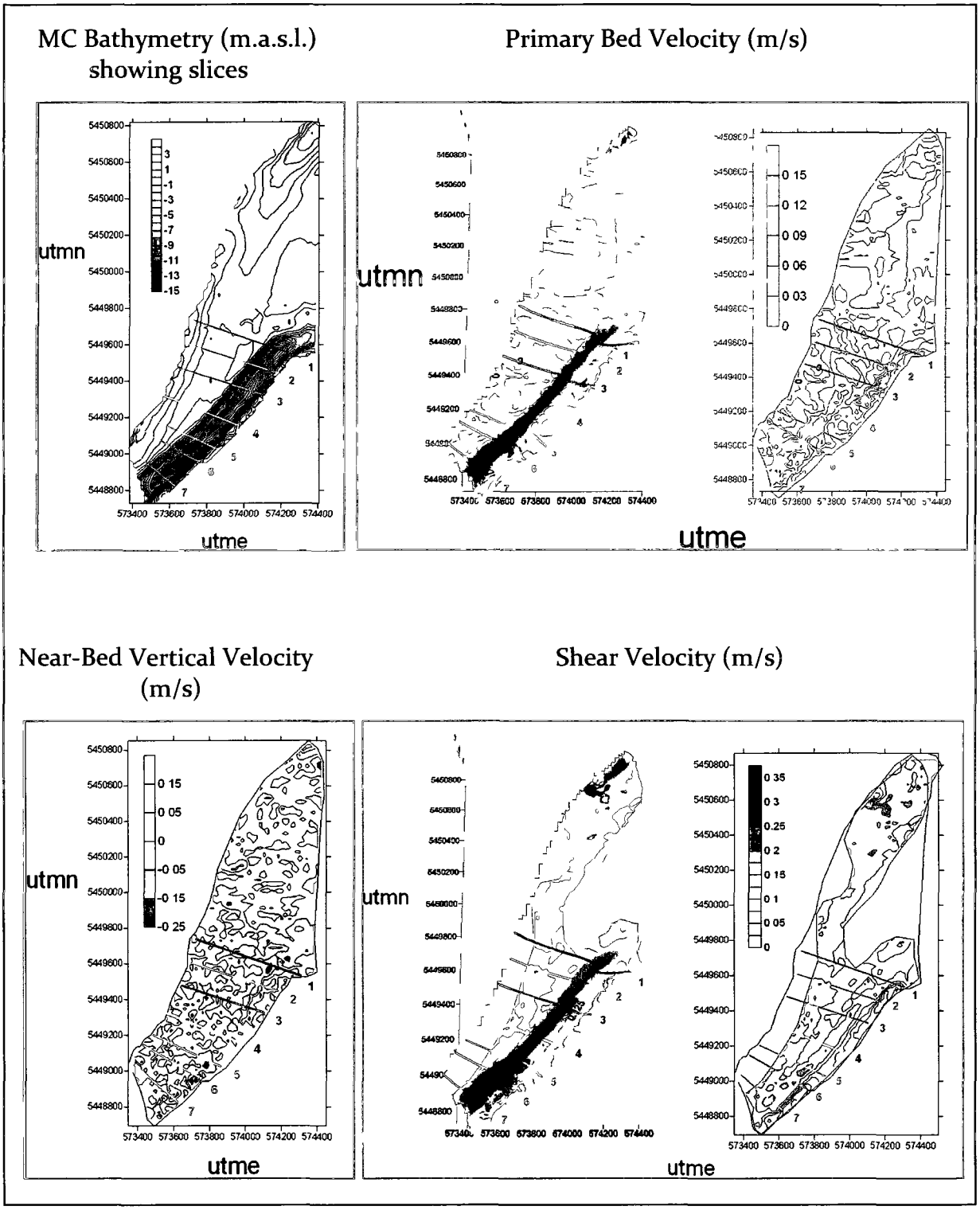

Figure 51 – Main Confluence Primary Bed Velocity, Near-Bed Vertical Velocity and Shear Velocity (m/s)

Minto Side Channel

The flow pattern through Minto side channel is detailed through progressive vertical cross-sections in the downstream direction, 8 – 10, oriented perpendicular to the banks showing the primary, secondary and vertical velocities (figures 52-54). At section 8 (figure 52), the thalweg is moving from the right bank towards the left bank, where the deep holes presumed to be from previous gravel-mining of the river bed are located. Some upward vertical velocity exists on the left side of the deep hole. At section 9 (figure 53), the thalweg flows along the left bank, there is some secondary velocity in the thalweg towards the left bank at the surface, and small upward velocities exist under the thalweg as the channel bed is rising out of the deep hole. At section 10 (figure 54), a small curved path has developed in the bed along the right bank in addition to the thalweg path in the bed curving away from the left bank. Some upward and upstream flow velocities exist in the inner bend of the small curved path along the right bank.

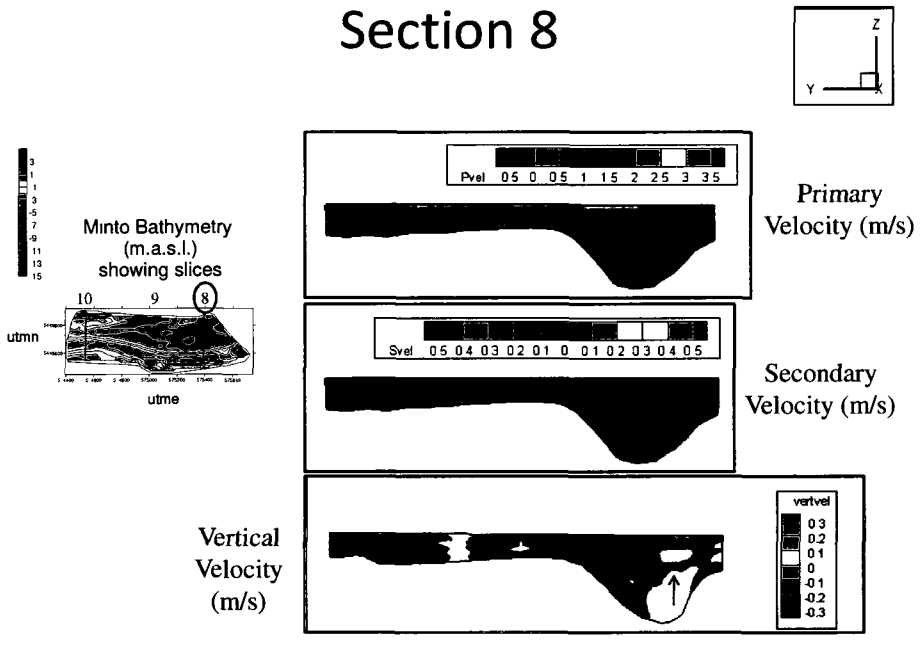

Figure 52 – Section 8 Flow Velocities (m/s), viewed from downstream

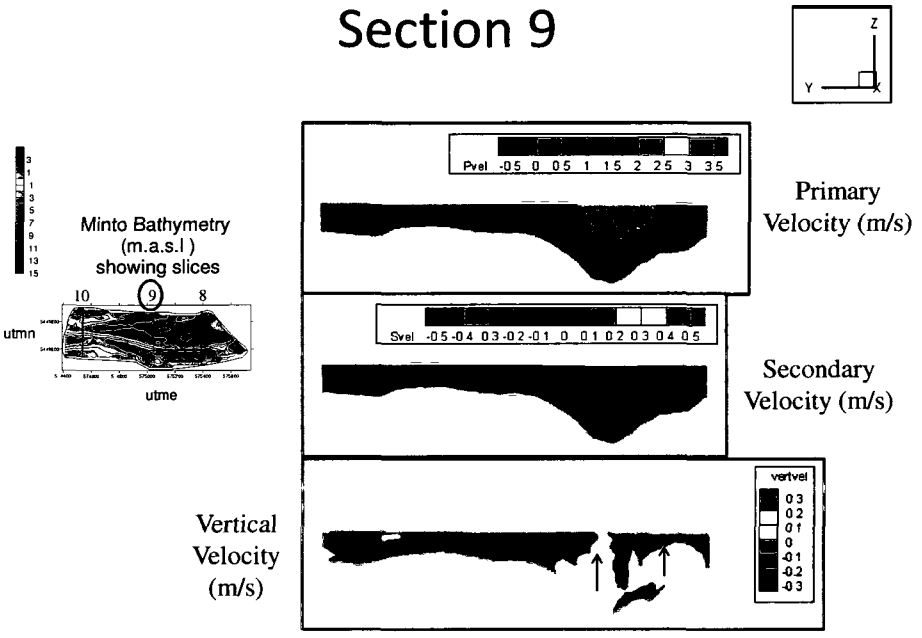

Figure 54 – Section 9 Flow Velocities (m/s), viewed from downstream

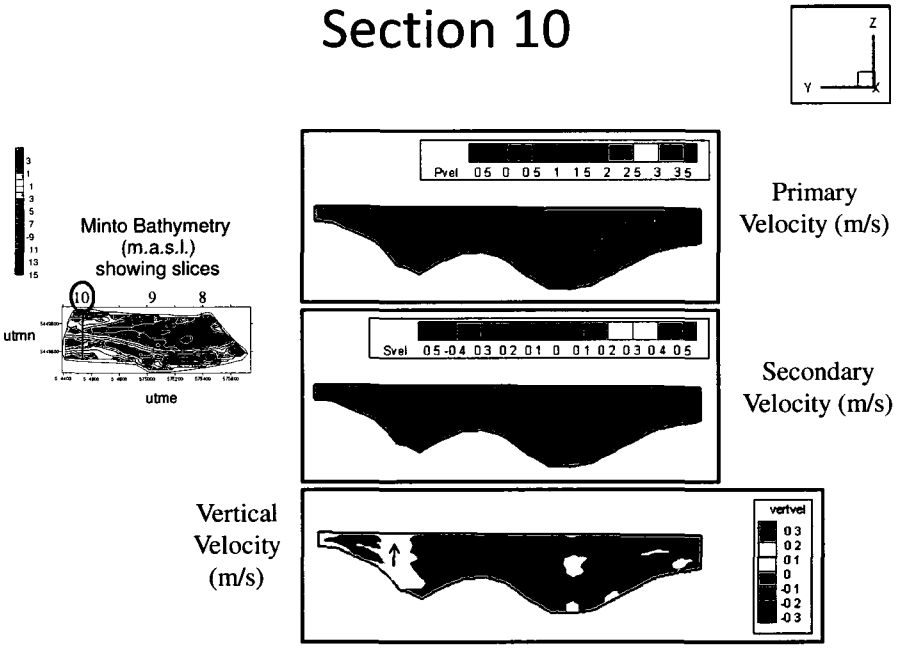

Figure 54 – Section 9 Flow Velocities (m/s), viewed from downstream

The primary bed velocity and shear velocity for Minto side channel are shown in figure 55. The primary bed velocities are highest in two downstream areas: along the right bank of the thalweg path in the bed as it curves to the left before entering the confluence area, and along the left bank of the small channel entering from Minto island as it curves to the right. Higher shear velocities, about 0.15 m/s, do exist in the deepest part of the thalweg channel in the downstream section, although it is not clear why similar shear velocities exist in the upstream riffle where there are no measured bed velocities. Intermediate bed velocities exist along the upstream part of the left side of the channel bed, where the deep holes are located. Despite lower shear velocities, upward vertical velocities match the bed velocities along the thalweg path between sections 9 and 10.

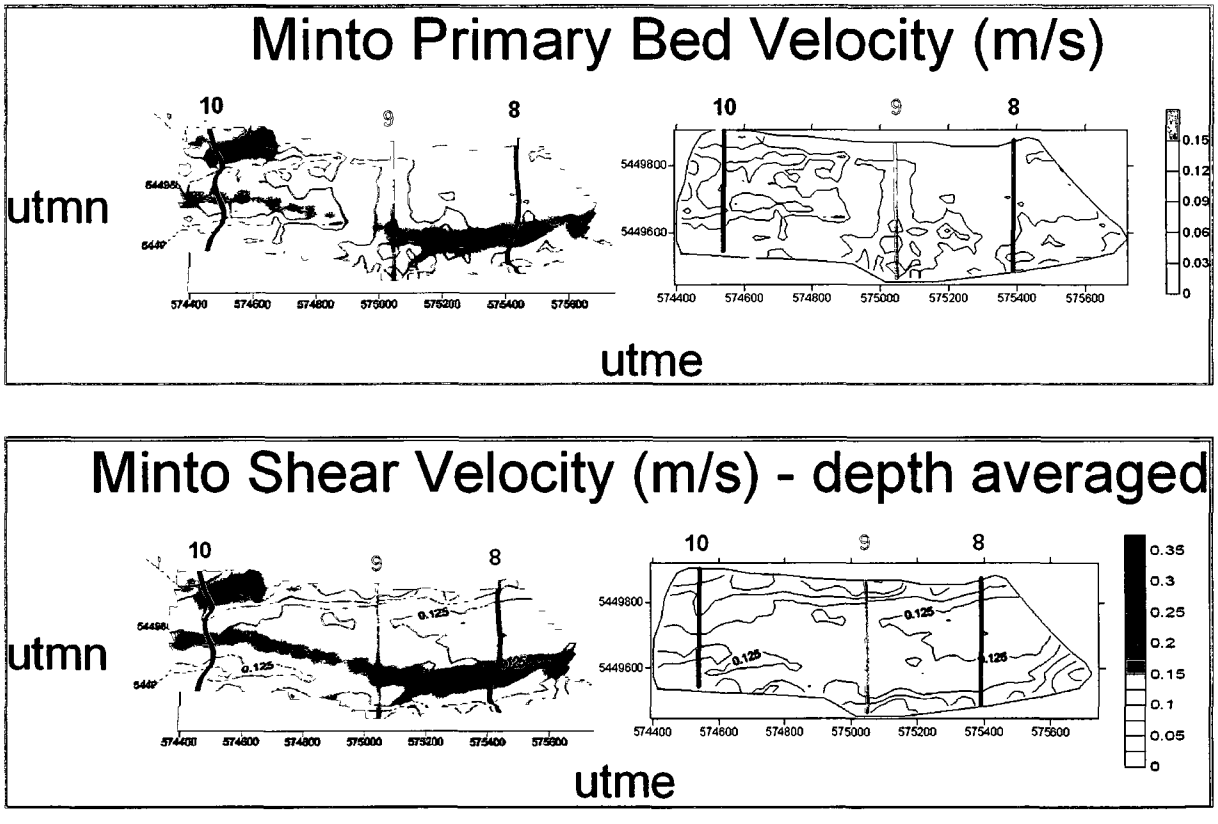

Figure 55 – Minto Side Channel Primary Bed Velocity and Shear Velocity (m/s)

A summary of distribution statistics of the measured and interpolated water, shear and bed velocities for the complete survey area are presented in Table 2. Primary and secondary water velocities were smoothed over 11 ensembles, and shear velocity was calculated from the smoothed primary velocity profiles. The vertical water velocities and bed velocities were single ping measurements. The water velocity error is the difference between the two single ping vertical velocity determinations for each bin, scaled for horizontal velocity. Primary water velocities are of much higher magnitude, with a mean of about 2 m/s, than the error velocities, with a standard deviation of 0.32 m/s. The standard deviation of error velocities for data smoothed over 11 ensembles becomes reduced to 0.1 m/s ($0.32/\sqrt{11}$ m/s). Secondary water velocities are much lower, but do represent the general secondary flow patterns identified by the values measured at both ends of the range. Vertical velocities are also low, so only bins with vertical velocity at least double the respective error velocity were selected. The standard deviations of interpolated values are all smaller than the measured values since the tight transect spacing resulted in significant averaging through kriging. Interpolated standard deviations for shear velocities and bed velocities are comparable to and are a bit lower than those of the surveys by Rennie and Church (2010) that included this reach since transect spacing was tighter for this study.

Table 2 – Data Statistics

		N	Minimum	Maximum	Mean	Standard Deviation
Water Velocity (m/s)	Smoothed u	643 849	-1.5	3.9	2.07	0.61
	Interpolated u	48 221	-0.030	3.40	1.96	0.59
	Smoothed v	643 849	-2.1	2.1	0.0058	0.21
	Interpolated v	48 221	-0.81	0.74	-0.0024	0.096
	Single ping w	77 934	-1.0	1.1	-0.021	0.17
	Interpolated w	48 221	-0.37	0.32	-0.028	0.069
Water Velocity Error (m/s)	Single ping	643 849	-1.5	1.5	0.000071	0.32
Shear Velocity (m/s)	Smoothed u^*	12 546	0.0030	0.22	0.13	0.030
	Interpolated u^*	2 866	0.014	0.20	0.13	0.035
Primary Apparent Bed Velocity (m/s)	Single ping v_a	27 673	-1.46	1.21	0.035	0.080
	Interpolated v_a	3 733	-0.061	0.17	0.044	0.030

Discussion

Biron et al (1998) determined that shear stress estimates, obtained by fitting the log-law (eq. 13) to the log-linear portion of the vertical velocity profile, were very sensitive to the inclusion of near-bed points. Velocity measurements for this study were obtained over 2 minute intervals with a 25 Hz ADV. Sime et al (2007) concluded that for single transect moving boat aDcp measurement of this Fraser river reach at flood flow, the most repeatable shear velocity estimate was that calculated from equation 14 using the depth averaged streamwise velocity and an estimate of bed roughness, because the mean velocity is less affected by instrument noise, turbulent fluctuations and near-bed errors. Estimates of shear stress calculated from fitting the log-law (eq. 13) were less repeatable and tended to be overpredicted. Plots of transect-averaged bed shear stresses showed good agreement between equation 14 using the depth averaged velocity and the average velocity of the three lowest bins, which indicated that both could be considered accurate "since the main source of error is uncertainty for both methods about z_0 and the estimators differ in their sensitivity to z_0" (Sime et al, 2007). Plots comparing the transect-averaged bed shear stresses for equation 13 with equation 14 using the depth averaged velocity showed that estimates calculated from equation 13 tended to be overpredicted since they were higher than the accurate estimates calculated from equation 14.

However, both equation 13 and 14 are only applicable to the full velocity profile if the streamwise velocity profile is log linear for the entire flow depth. This condition is clearly not satisfied where the Minto flow plunges into the scour hole at the confluence of the main channel with Minto side channel. Sime et al (2007) also noted that the flow may not be log-linear in the upper half or more if secondary currents are present, as they are in the elongated scour zone along the left bank. The vertical primary velocity profiles at three representative points in the main confluence area are shown in figures 56 and 57: at a riffle in the main channel upstream of the confluence, at the point of maximum scour at section 3 where plunging flow occurs, and at the point of maximum upwards vertical velocity near the left bank at section 2.

The vertical primary velocity profile at the riffle is log-linear with elevation above the bed, having the standard upwardly concave parabolic shape for the plot of velocity versus elevation. The plot of velocity versus elevation for the plunging flow has an irregular shape, with velocity increasing from the bed to 20% of the flow depth and then decreasing. The plot of velocity versus the natural logarithm of the elevation above the bed for the plunging flow shows that the lowest 20% of the flow can be considered log-linear. Where strong upwards flow exists, the plot of velocity versus elevation is fairly linear overall but shows a lot of scatter within the lowest 20% of the flow. This scatter is only somewhat reduced in the plot of velocity versus the natural logarithm of the elevation above the bed, so even the lowest 20% of the flow is not log-linear. This assessment was qualitative, but a quantitative evaluation of the log-fit using R-squared values could be determined, with a threshold value used to select those profiles with large enough R-squared values to be considered log-linear for the lowest 20% of the depth.

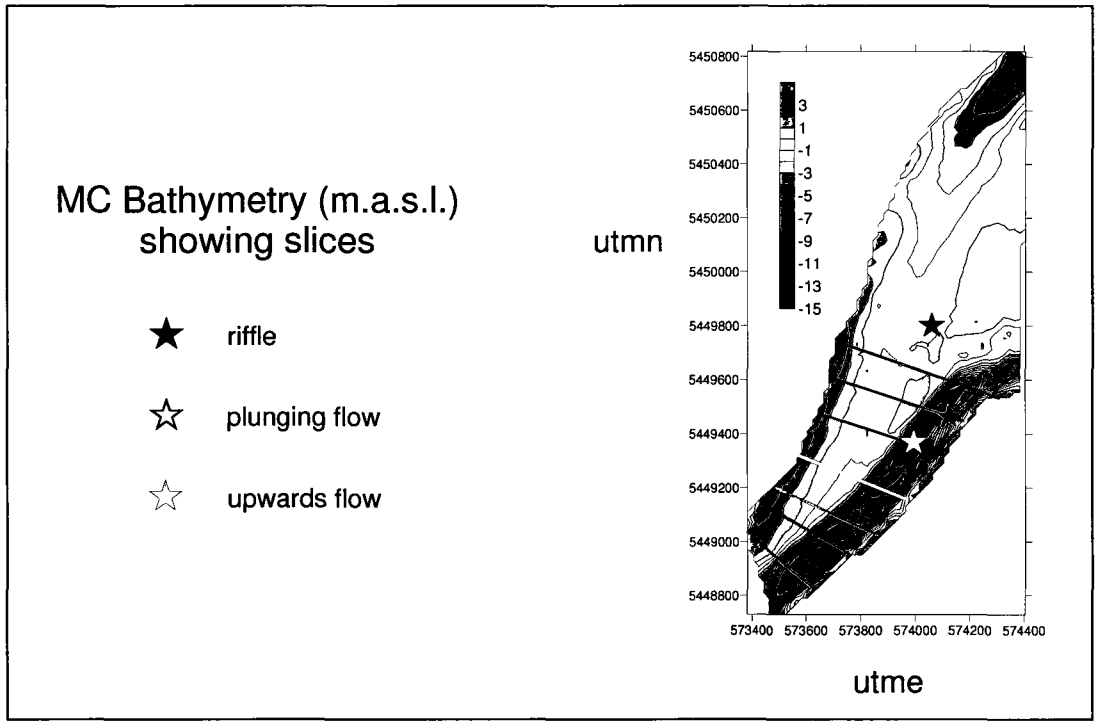

Figure 56 – Locations of Vertical Velocity Profiles

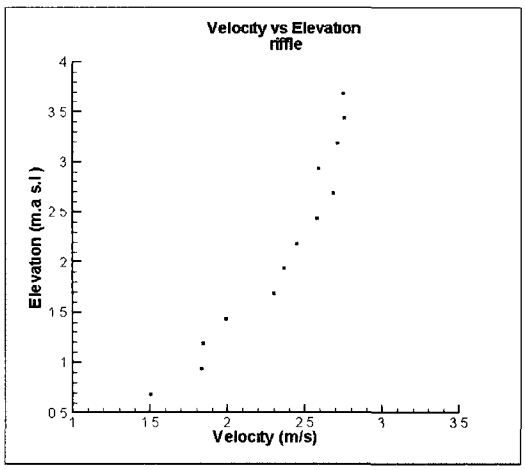

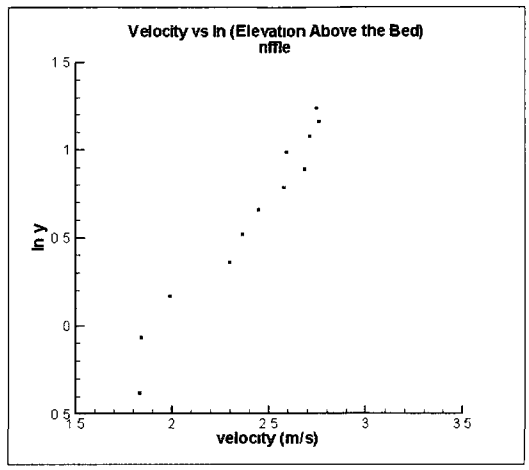

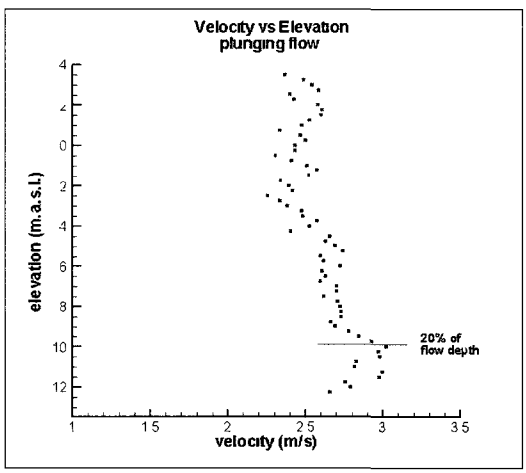

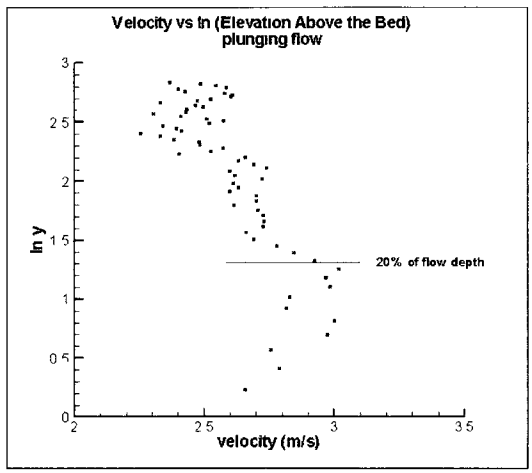

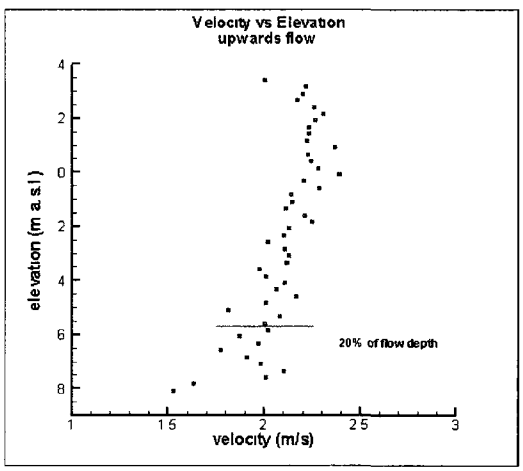

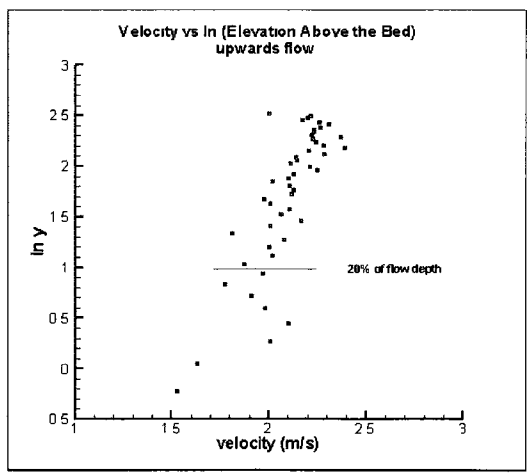

Figure 57 – Vertical Velocity Profiles

Plots of confluence shear velocity were calculated in four ways: from fitting the log-law using both equation 13 (unconstrained log fit) and 14 (depth-averaged) to the full profile, and to the lowest 20% of the flow depth, defined from the lowest bin (above 6% of the flow depth) to the bin at or just below 20% of the flow depth. The results for the confluence shear velocity using the lower velocity profile are shown in figure 58, and using the full profile in figure 59. Results for the lower velocity profile are limited to profiles with at least 3 bins lower than 20% of the flow depth, and so are not available for the shallower regions of the confluence area.

Only the shear velocity calculated from the lower velocity profile (figure 58) is valid across the majority of the confluence area, applicable where plunging flow exists but not where strong upwards vertical velocity exists along the left bank (figure 51). The shear velocity plot in figure 58 a, calculated using the depth averaged velocity (eq. 14), shows high values along the main channel thalweg, and along the elongated scour near the left bank downstream of section 2. The highest values exist where the flow accelerates: at the upstream bend of the main channel, in the deep scour at section 3 where the Minto flow plunges upon entering the confluence, and in the deep scour along the left bank from section 5-7 where the high velocity cores have joined. The same general pattern is evident in the shear velocity plot in figure 58 b, calculated using the unconstrained log-fit (eq. 13), though the values are more variable and roughly double those of the depth averaged, having a maximum of 0.3 m/s. High values are identified in a much smaller portion of the plunging flow using the unconstrained log-fit, perhaps due to the greater variability in the individual velocities in the highly non-uniform plunging flow. These differences between the depth-averaged and unconstrained log-fit plots of shear velocity for the lower profile also exist for the full profile (figures 59 a and b). As expected, the shear velocity plots calculated using the full profile (figure 59) did not show higher values in the elongated scour zone along the left bank of the confluence. Similarly, Szupiany et al (2009) reported that shear velocity calculated using the entire flow depth did not

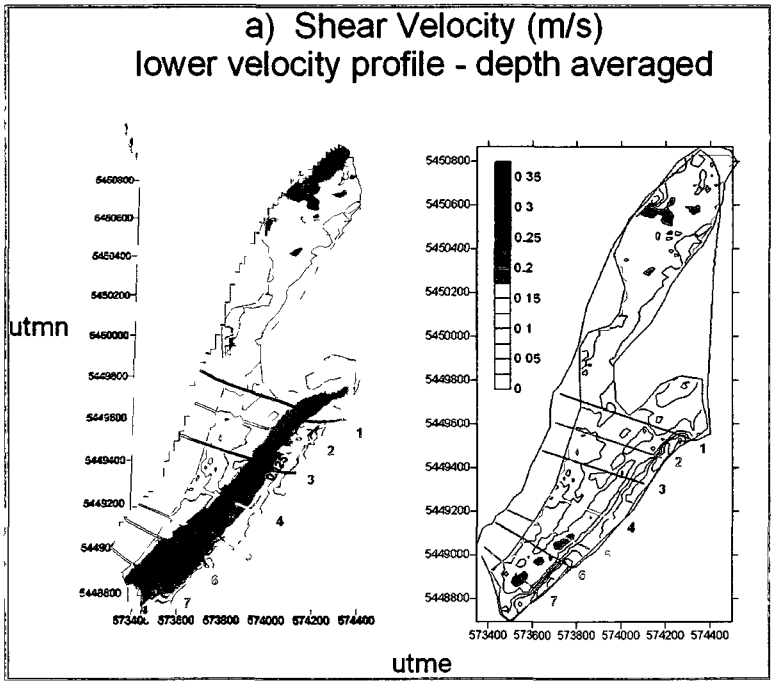

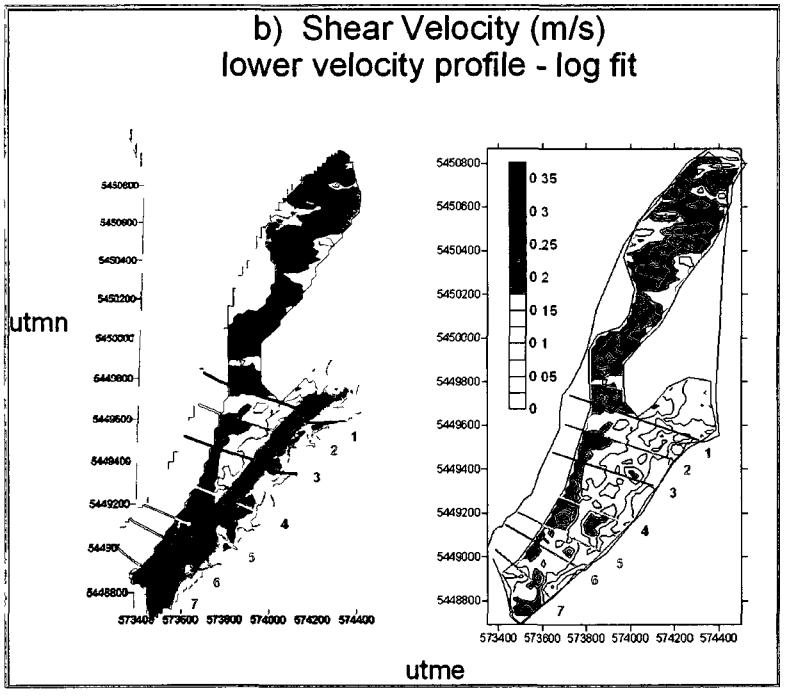

Figure 58 – Main Confluence Lower Profile Shear Velocity (m/s)

a) depth averaged b) unconstrained log-fit

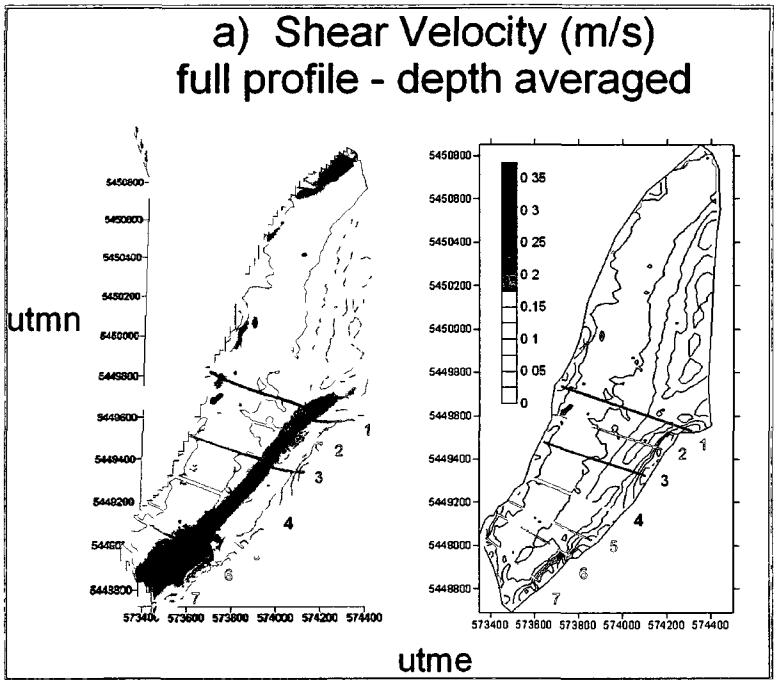

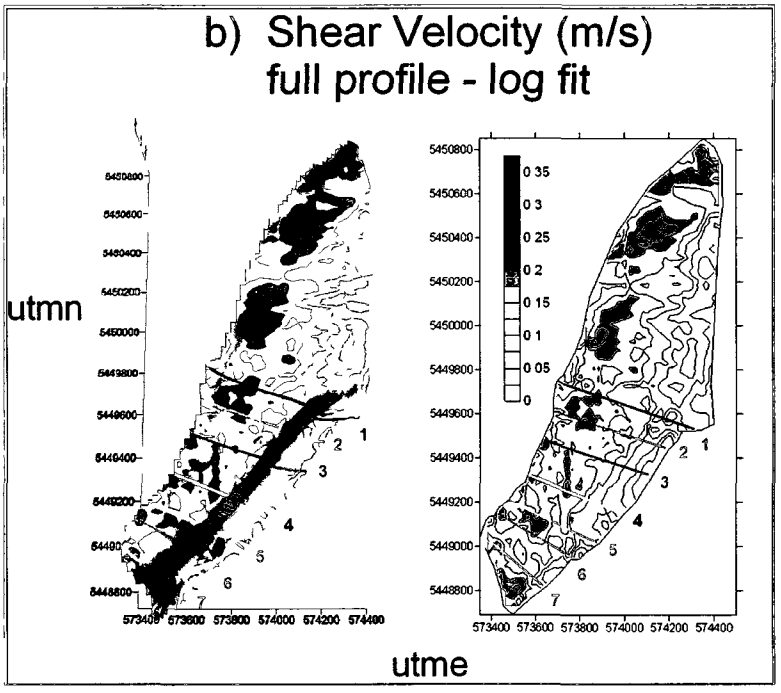

Figure 59 – Main Confluence Full Profile Shear Velocity (m/s)

a) depth averaged b) unconstrained log-fit

correlate well with suspended sediment concentration at confluence B along the Parana River where significant secondary currents existed.

Plots of shear velocity in Minto side channel calculated from applying both equations 14 and 13 to the full vertical primary velocity profiles are shown in figure 60. Again, the highest shear velocity values for the unconstrained log-fit (eq. 13) were double the highest values for the depth-averaged log-fit (eq. 14), and the shear velocities were much more variable.

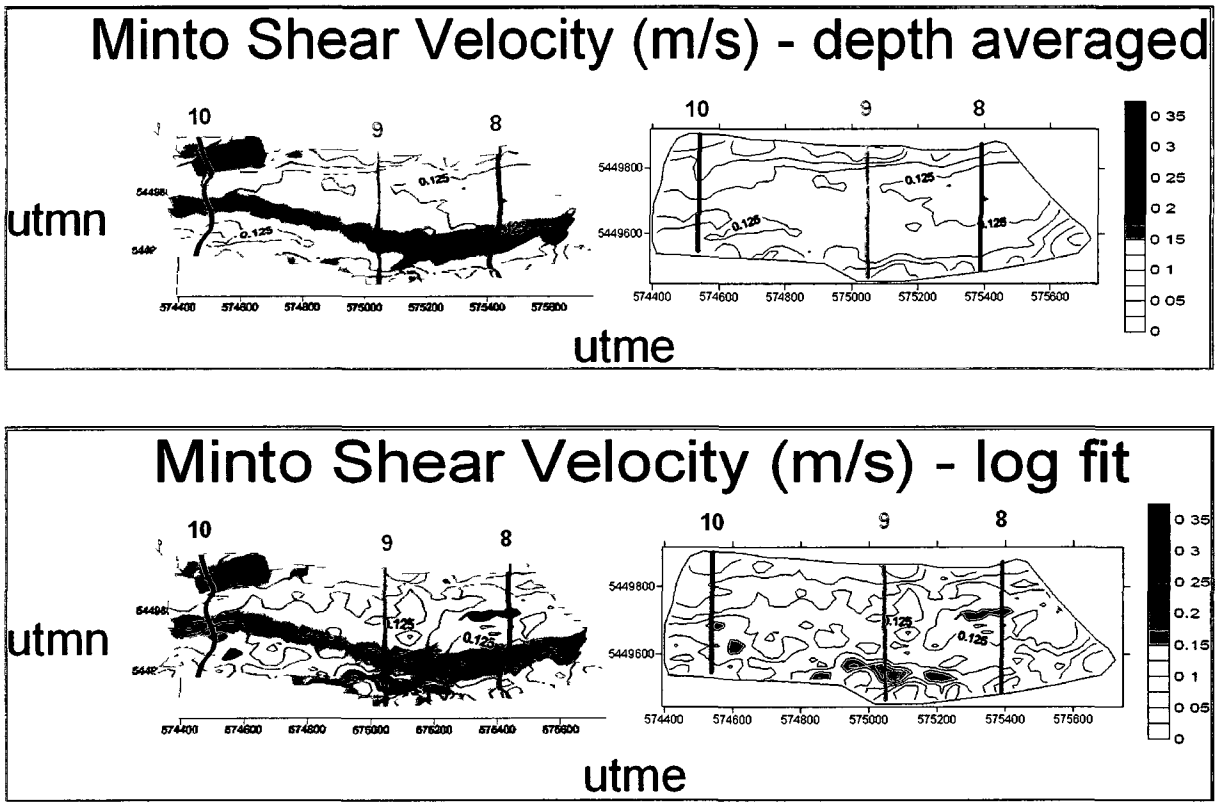

Figure 60 – Minto Full Profile Shear Velocity (m/s)

The unconstrained 2 parameter log-fit (eq. 13) to the vertical velocity profile provides an estimate of the bed roughness in addition to shear velocity. The reasons the

unconstrained log-fit gives less repeatable estimates have been explained above. However, the estimates of bed roughness obtained are examined herein for relative patterns of bed armouring. Bray and Davar (1987) reviewed the gravel bed roughness literature, and k_s=3.5D84 was fitted to Alberta gravel-bed rivers at 2-year bankfull flows. This relationship is a guide, and an assessment of how exactly it represents the flow resistance from bed roughness for this reach of the Fraser River has not been investigated. The roughness used in equation 7 (z_o=0.1D84) is equivalent to k_s=3.0D84, which is similar to the value of k_s=3.5D84 fitted by Bray and Davar (1987). Unconstrained estimation of local k_s directly using equation 13 allows for comparison of the shear velocity plots calculated using the two equations.

The plots of kriged D84 values, for the lower profile and the full profile along the main channel thalweg where the log law is applicable to the full flow depth, and the primary bed velocity, are shown in figure 61 for the main confluence. The plot of kriged D84 values for the full profile in Minto side channel, where the log law is applicable to the full flow depth, and the primary bed velocity, are shown in figure 62. The average D84 value was calculated to be 0.162 m for the main confluence using the lower profile, 0.073 m for the main channel thalweg where the full profile is applicable, and 0.102 m for Minto side channel. Pebble counts of bar tops exposed in winter low flows for the main channel yielded a D84 of 40 mm, with error within ± 50% or ± 20 mm (Sime et al (2007). Bar tops might be expected to have finer sediments than the channel thalweg. However, Sime et al (2007) did report a 1983 dredge sample of D84 = 20 mm and bimodal sand/gravel distribution from the thalweg near transect 1 (about 15 km downstream of confluence location of current study), which was within the ± 50% error envelope for the Sime et al (2007) transect 1 result for D84 = 26 mm ± 13 mm. Despite the differences between the D84 from the pebble counts of bar tops (Sime et al, 2007) and the unconstrained log-fit D84 estimates (filtered coarsely for k_s), the distribution of unconstrained log-fit estimates were qualitatively analyzed to show relative D84 patterns.

The plot of D84 for the main confluence (figure 61 a) using the lower profile shows coarser bed material throughout the area, except for fining along the elongated bed step adjacent to the mixing layer where higher upwards vertical velocity and primary bed velocity (figure 51) exist between sections 3 and 5. Erosion would appear to have removed the armoured bed surface to expose the finer subsurface. At section 4, finer particles extend across to the left bank where strong upwards vertical velocities also exist. The plot of D84 for the main confluence (figure 61 b) using the full profile in the main channel thalweg, where the log law is applicable to the full flow depth, is only similar to the plot of D84 using the lower profile only in the upstream bend, showing coarser bed material where higher primary bed velocity also exists. The riffle section of the main channel shows finer bed material in figure 61 b), with a very similar size distribution to that of the riffles in figure 62 for Minto side channel. The average D84 value using the full profile in the main channel thaweg is closer to the pebble count of exposed bar tops at low flow. Visual inspection of the D84 under shallow water along Queens Bar in the plot of D84 (figure 61b), which would become exposed during low flows, shows that it generally ranges from 0.025 m to 0.075 m, which is quite similar to the D84 = 40 mm ± 20 mm reported from pebble counts of exposed bar tops in this section (Sime et al, 2007)

The differences in the plotted D84 values for the main channel riffle section between the lower profile and full profile are significant. The plots of shear values from the lower profile and the full profile in the main channel upstream of the confluence are much more comparable, though the plot of shear velocity from the log-fit to the limited number of values in the lower profile is much more variable and is the least similar to the other shear velocity plots. This suggests that little confidence can be ascribed to the results generated from fitting the log law to the 3 to 5 values comprising the lower profiles. Since the bed D84 size distribution is visually similar for the main channel upstream of the confluence and Minto side channel, from application of the log law to the full flow depth, and that measured and predicted ranges of D84 for bar tops exposed at low flows were found to overlap closely, it

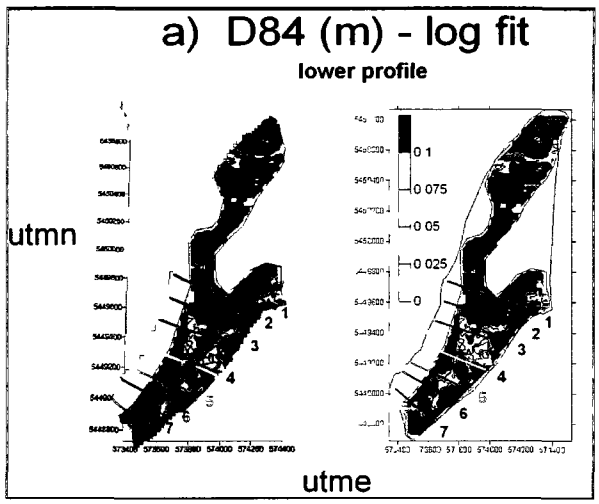

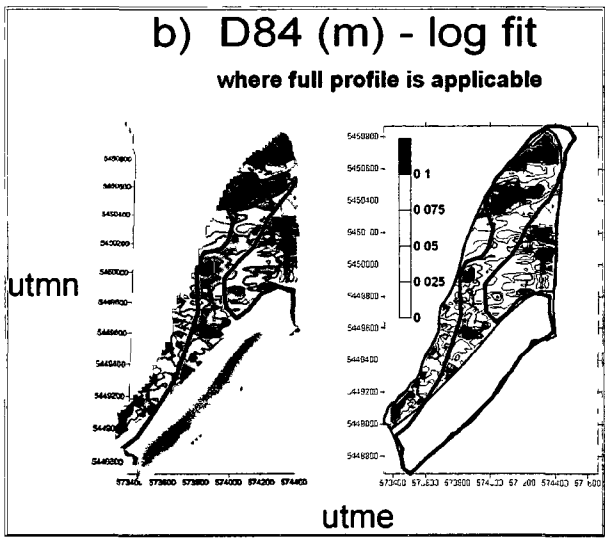

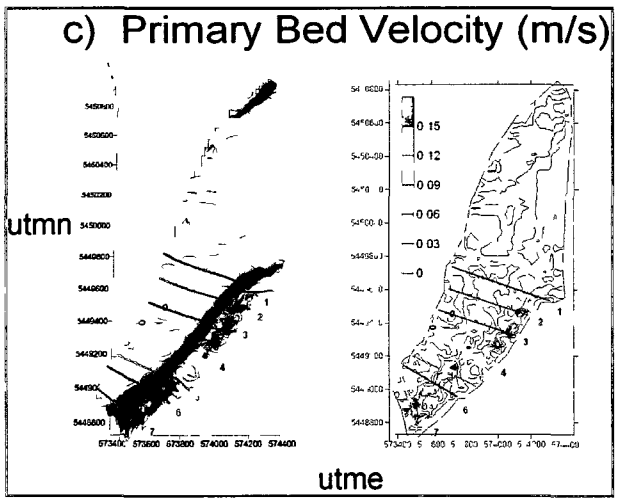

Figure 61 – Main Confluence D84 and Primary Bed Velocity

would appear that there are enough values in the full profiles for roughness estimates to be valid for qualitative analysis. The average number of values in the full profiles was 15, in the section of the main confluence where the log law is applicable to the full flow depth, and 14 in the full profiles in Minto side channel.

The plot of D84 for Minto side channel (figure 62) shows that the thalweg along the left bank from section 8 to beyond section 9 is much coarser than the higher central section of the bed. This area of the bed experiences upwards vertical velocity, as seen in the velocity plots of sections 8 and 9 (figures 52 & 53). The right bank between sections 9 and 10 shows a similar coarseness, where there are also upstream and/or upwards velocities. Two areas of higher primary bed velocity also show coarsening or armouring of the bed: along the inner and outer bend of the thalweg path at section 9, and along the outer bend of the thalweg path at section 10.

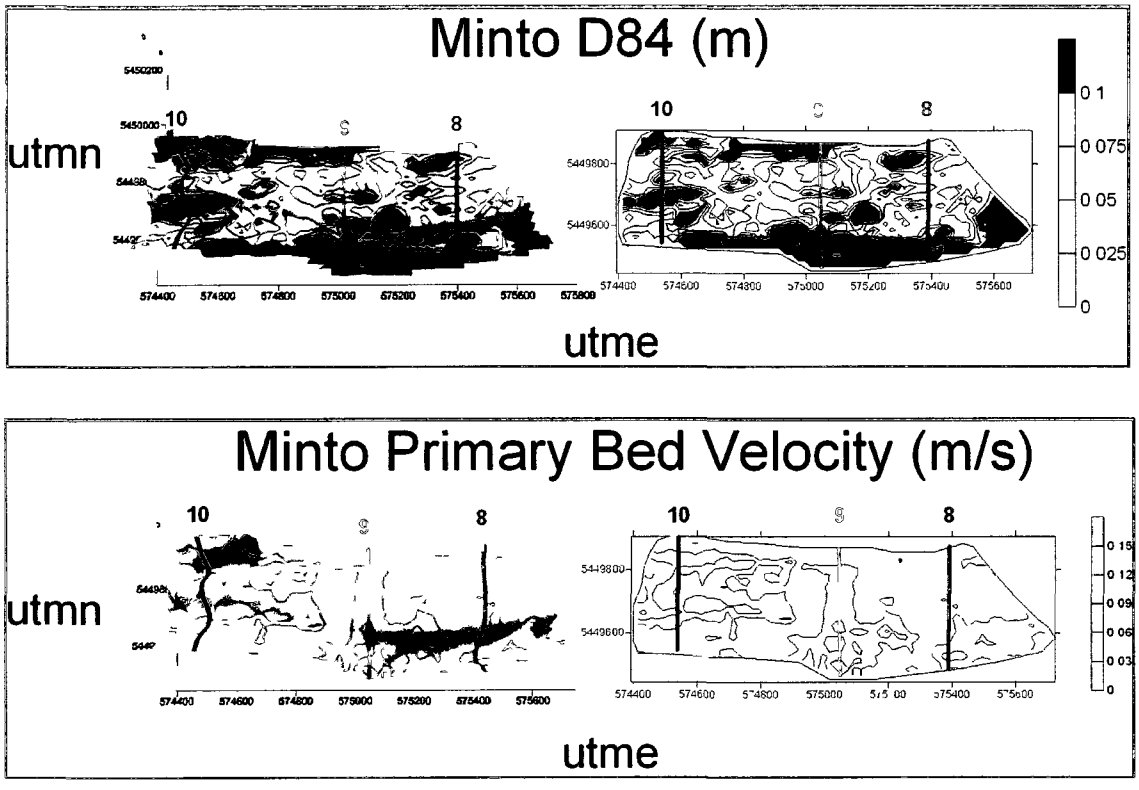

Figure 62 – Minto D84 and Primary Bed Velocity

A pattern of bed armouring exists in the thalweg in the main confluence area upstream of the confluence and in Minto side channel where the highest bed velocity and/or vertical velocity exist. The coarsening of the bed surface of gravel bed rivers, with respect to the underlying or subsurface material, for a large range of flow conditions and sediment transport rates, has been well documented (Andrews and Parker, 1987). It is not clear how reliable the qualitative analysis of roughness estimates in the confluence area from application of the log law is due to the limited number of values in the lower profiles. However, it is likely that erosion of the steep bed step along the very deep confluence scour hole would penetrate the bed surface to expose a finer subsurface. Visual inspection of the plots shows the secondary currents near the mixing interface in the confluence correlate well from with the primary bed velocities and bed surface fining along the bed step between sections 3–5.

Significant erosion is occurring along the left bank of the confluence of the Fraser River main channel and Minto side channel, identified in a 2006 acoustic survey (Rennie and Church, 2007). The increase in sinuosity of the main channel between lower Minto and Queen Islands is evident from comparison of the 1971 (figure 27), 1999 (figure 28), and 2006 (figures 29 & 30) airphotos. The tightening of the channel bends has redirected the thalweg across to the left bank of the confluence, moving the mixing interface to the left and confining the Minto flow against the left bank. Figure 33 shows the bank erosion at the upstream end of the left bank, and the tree that fell into the river overnight between June 10th and 11th, 2008, observesed on the second day of the survey. The erosion and riprap at the downstream end of the left bank are shown in figures 34 and 35. The 2006 and 2008 confluence airphotos are presented in figure 63. The 2008 airphoto was taken at a higher stage than the 2006 airphoto, but comparison would appear to show a more curved edge, hence greater erosion of the left bank, in the 2008 airphoto. However, since these two airphotos are not orthorectified, no quantitative comparisons of the position of the left bank edge between 2006 and 2008 can be made.

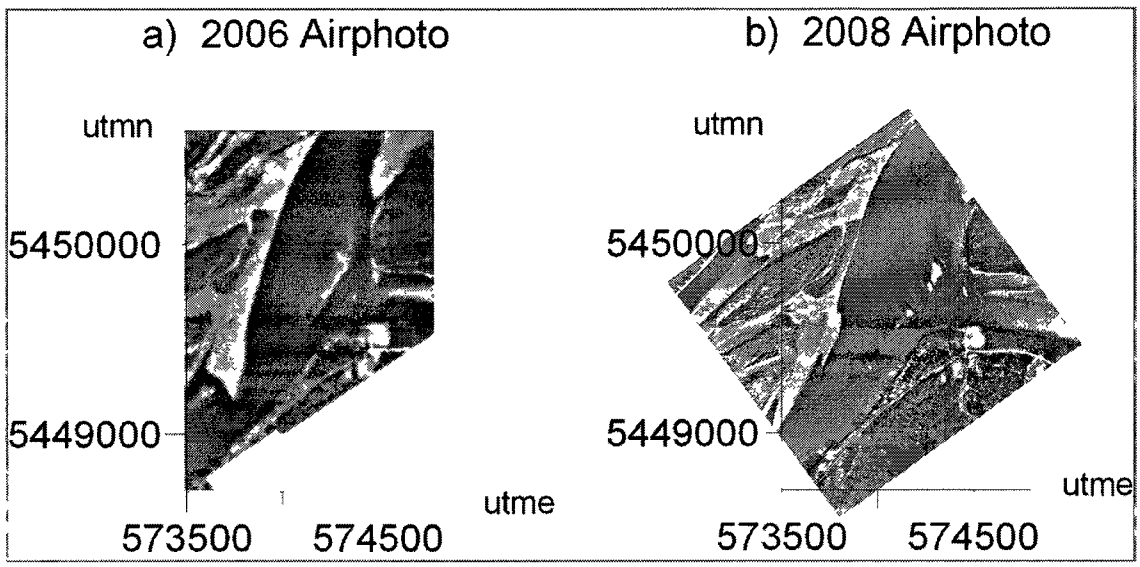

Figure 63 – 2006 and 2008 Confluence Airphotos
(photos courtesy of M. Church, UBC)

Bed and bank erosion at the confluence is examined through detailed plots of the confluence bathymetry, bed velocity vectors, near-bed horizontal velocity vectors, near-bed vertical velocity, shear velocity and primary bed velocity, shown in figure 64. The elongated confluence scour consists of two scour holes with an elevation of 15 m below sea level and a shallower section in between them with an elevation of 11 m below sea level (figure 64 a). The deep upstream hole is located under the mixing interface, next to the bed step, and the deep downstream hole is located next to the left bank where the flow is constricted by rock riprap. Erosion along the left bank occurs between section 1, where the upstream riprap ends, and section 6, where the downstream riprap begins.

The helical flow patterns are strongest at the beginning of the confluence, and the bed velocity vectors in the upstream scour hole, sections 2 and 3, are clearly directed away from the mixing interface (figure 64 b). The main channel near-bed flow changes from being directed towards the bed step to along it at the mixing interface, and the

Minto flow at the mixing interface is directed towards the left bank (figure 64 c). The line of near-bed downward vertical velocity (figure 64 d) shows the location of the mixing interface, extended from the top of the bed step at section 1 to the bottom of the bed step at section 5. Strong upward near-bed vertical velocity exists along the left bank, from section 1 to 4 (figure 64 d), completing the helical flow left of the mixing interface and resulting in bank erosion. High primary bed velocity, found along the left bank from section 1 to 4 (figure 64 f), closely matches the near-bed upwards vertical velocity.

At the downstream scour hole, helical patterns have dissipated and flow consists of a single coherent cell. From section 5 to 7, the near-bed velocity vectors and the bed velocity vectors along the left bank are directed towards the bed step (figures 64 b, c). Strong downward flow exists from section 5 to 7 near the left bank, confined by riprap at section 6 (figure 64 d), resulting in deep scour. High shear velocity matches high primary bed velocity along the bed step at the downstream scour hole (figures 64 e, f).

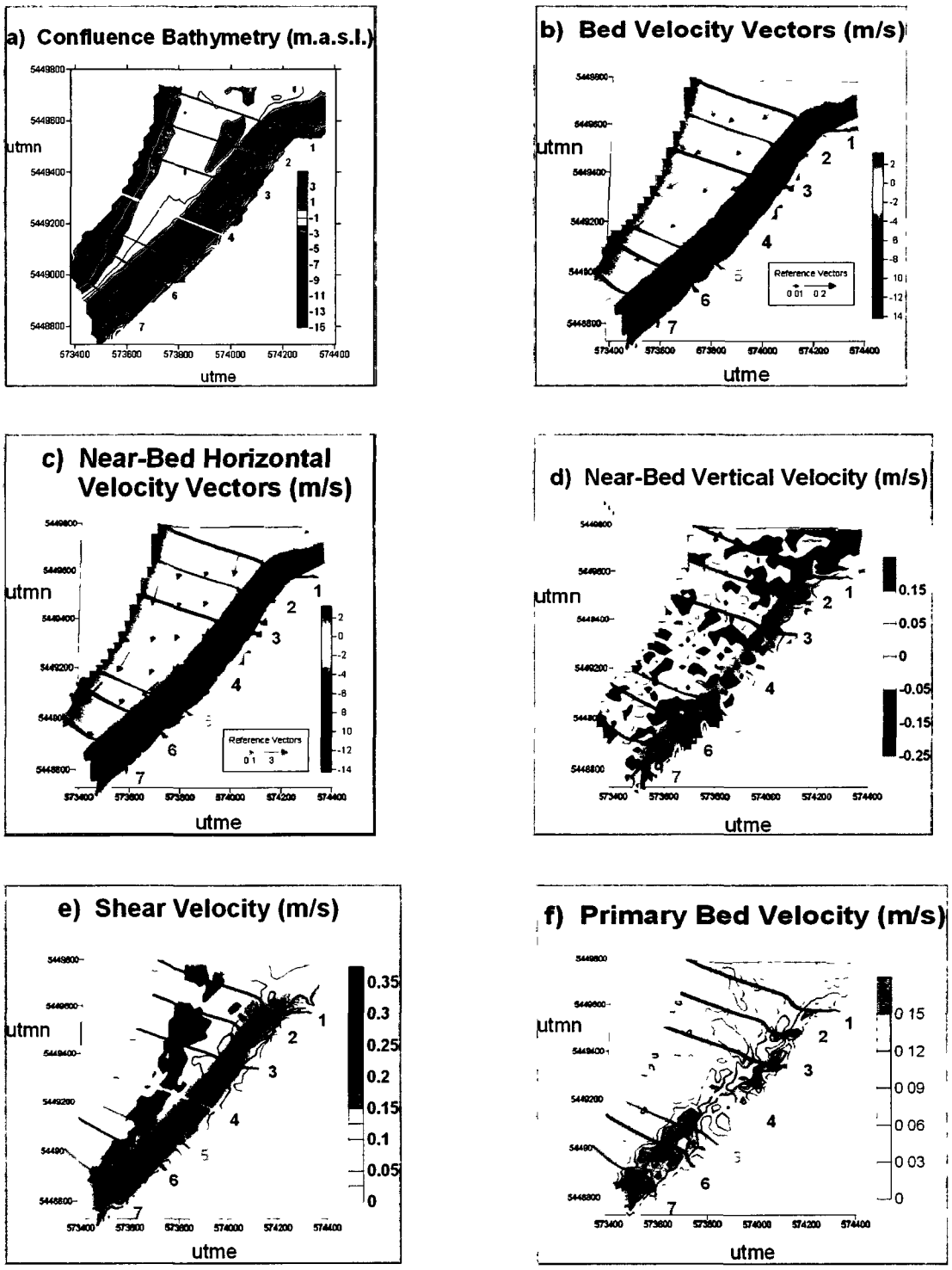

Figure 64 – Confluence Flow, Bed, and Shear Velocity (m/s)

Conclusions

This study described the morphodynamics of the high angle asymmetric gravel-bed confluence of the Fraser River main channel with Minto side channel, downstream of a mid-channel island near Chilliwack, BC:

1. Maximum primary velocities reached 3.5 m/s, maximum secondary velocities ranged from -0.5 to 0.5 m/s, and maximum vertical velocities ranged from -0.3 to 0.3 m/s.
2. A vertical mixing interface paralleling the left bank was identified from secondary flow patterns, with flow being advected down into a deep elongated scour zone along the left bank, reaching a depth of 18 m with bed slopes between 10° and 20°, flanked by an elongated bed step to the right.
3. The Minto flow was confined by the main channel flow against the left bank and accelerated, plunging to the bottom of the scour hole upon entering the confluence.
4. A coherent helical flow cell existed in the confined flow to the left of the mixing layer, and a partial helical cell to the right of the mixing layer. These secondary flow patterns dissipated as the high velocity cores merged in the downstream half of the confluence zone.
5. Flow acceleration occurred in the downstream main channel thalweg bend, where it was also constricted by the downstream riprap along the left bank, resulting in high downstream velocities and downward vertical velocities.
6. Apparent bed velocity generally followed the thalweg, with the highest values near 0.15 m/s occurring at the edges of the scour zone, along the elongated bed step and along the left bank where the plunging flow and upwards vertical velocity existed.

Significant erosion existed along the left bank between the upstream and downstream bank protection (rock riprap). Examination of aerial photographs from 1971 to 2006 showed an increase in sinuosity of the main channel between lower Minto Island and Queens Islands, resulting in deposition downstream of Minto island and erosion along Queen Island. The confluence angle has increased and the mixing interface has moved closer to the left side of the confluence. The main channel flow confined the Minto flow entering the confluence against the left bank, and flow was advected strongly down into the scour hole, plunging to the bottom, accelerating and resulting in deep scour. Strong upwards vertical velocities along the left bank comprise part of the helical flow cell to the left of the mixing layer, and have led to erosion along the left bank between the upstream and downstream riprap. Scour deepened again along the left bank at the downstream end of the confluence zone, resulting from the strong downward vertical velocity where the flow is confined by riprap. This alluvial stretch of the Fraser River is in a state of dynamic equilibrium. The deep scour and bank erosion along the left bank represent the river adjusting its' course to the high flows and increased sediment transport of the freshet, aligning the banks at the confluence with the dominant sinuous main channel thalweg.

At the confluence of the main Fraser River channel with Minto side channel, apparent bed velocity gave a rapid non-intrusive measure of the spatial distribution of the bed-load transport. Plots of shear velocity, calculated by applying the log law using the mean streamwise velocity and an estimate of bed roughness, correlated well with apparent bed velocity plots. The biggest inconsistency between the two plots, where the calculated shear velocity was low and the apparent bed velocity was high, occurred at the plunging flow along the left bank of the upstream scour hole where strong upwards vertical velocity existed.

It is recommended that a river morphodynamics study include a direct measure of the bed-load transport, such as aDcp apparent bed velocity. Physical bed-load transport measurement is subject to significant measurement errors and is often not safe to conduct at high channel-forming discharges in large rivers. The shear forces applied

by the fluid to the bed can be calculated from flow velocities, however sediment transport is also dependent on the available sediment supply and the state of the bed, such as armouring of the bed surface. Bed-load transport formulae are based on the bed shear, and lift forces on bed particles are considered to scale with the drag forces applied by the flow. The existence of significant upwards vertical velocities can locally increase bed-load transport. The bed shear is usually calculated from applying the law of the wall to the log layer, and a determination of the bed roughness or characteristic bed particle size is required. Determination of the surface and subsurface sediment size distribution of the river bed would be ideal, however this analysis is not often conducted due to physical and time constraints. An estimate of the bed roughness can be calculated from applying the law of the wall to the log layer in the flow, but stationary high-frequency measurement is required to accurately determine the average streamwise velocity. In order to analyse the interactions of the fluid dynamics, the sediment transport and changes in bed morphology, it is very beneficial to have a spatial measure of all three.

Three representative vertical primary velocity profiles were examined and the lowest 20% of the flow was determined to be log-linear for the majority of the confluence. The profile for the entire flow depth was log-linear at the riffle point, the plunging flow was log-linear for the lowest 20% only, and flow was not log-linear where strong upwards velocity existed. Shear velocity reached a maximum of 0.2 m/s, corresponding to a bed shear of 40 N/m^2, with highest values in the main channel thalweg and in the deepest part of the scour under the mixing interface. Assessement of how much of the vertical streamwise velocity profile can be considered log-linear, when using the law of the wall to determine the shear force, is recommended for confluence studies.

Shear velocity plots were also calculated using the unconstrained two parameter log-fit, and showed the same general patterns, though having much more variability. Bed roughness estimates calculated by applying the unconstrained two parameter log-fit to the full flow depth in the main channel upstream of the confluence yielded mean

D84 values similar to those obtained from pebble counts of the bar tops exposed at low flows (Sime et al, 2007). Plots of the bed roughness estimate showed patterns of bed armouring at thalweg bends in the main channel and Minto side channel, with the finer subsurface evident in the confluence where erosion along the steep bed step occurred.

For single transect moving boat aDcp measurement, more consistent shear velocity plots were obtained by applying the log law using the mean streamwise velocity and an estimate of bed roughness, but where no bed roughness estimate is available, patterns of shear velocity are evident in plots calculated by using the unconstrained two parameter log-fit. For confluence studies where only the lowest 20% of the depth can be considered log-linear, it is recommended that the mean streamwise velocity and an estimate of bed roughness be used to determine the bed shear when single transect moving boat aDcp measurement is employed.

The study of confluences of large rivers at high discharges has recently been made possible by moving boat aDcp measurement. Several confluences along the sand-bed Parana River, in Argentina, have been studied for flows ranging from 12, 000 to 15, 000 m^3/s (Lane et al, 2008, Szupiany et al, 2009, and Parsons et al, 2007). This study of the confluence of the Fraser River main channel with Minto side channel, BC, is the first study of a large gravel-bed river confluence at channel forming flow, with a discharge of 7, 500 m^3/s. The pattern of full and partial helical cells, limited in both downstream and cross-stream extent to the scour zone, identified in the confluence studies of the high width to depth ratio Parana River, were also found to exist in this Fraser River confluence. The width to depth ratio for the Parana River confluences ranged from 100 to 200, and was 70 for the Fraser River confluence. In gravel-bed rivers, bed-load is transported on or near the bed. Riffles, point bars, and mid-channel islands form in the channel bed where the bed-load is deposited; in an aggrading river these deposits can cause a sudden change in the direction of the flow, termed an avulsion. Flow can then impinge on channel banks at a steep angle, causing significant erosion and rapid bank recession. The deep scour and bank erosion measured at this confluence is

characteristic of alluvial gravel-bed rivers and constitutes a major difference from sand-bed confluences.

A standardized method of moving boat aDcp measurement has not yet been developed. Many researchers have used repeated transects at several pre-determined cross-sections of the three-dimensional flow volume to be studied (Dinehart and Burau, 2005, Sime et al, 2007, and Szupiany et al, 2009) or single transects at pre-determined cross-sections (Parsons et al (2005, 2007), Lane et al (2008). An alternate method, using single zig-zag transects to yield measurements more widely spaced through the flow volume, was used in this study, by Rennie and Millar (2004) and Rennie and Church (2010. The measurements obtained by using single zig-zag transects are then kriged to reproduce the three-dimensional flow volume. Cross-sections can be investigated by taking vertical slices throughout the flow volume, and the ones of greatest interest chosen post-measurement to best represent the flow dynamics. Proposed future work for this reach includes an analysis of the tradeoff between the greater spatial resolution of the flow from this zig-zag approach, albeit with larger error in the velocities, as compared to the lower error within the repeated transects at the pre-determined cross-sections but much lower 3D spatial resolution.

References

Andrews, E.D., and Parker, G. (1987) 'Formation of a coarse surface layer as the response to gravel mobility.' In *Sediment Transport in Gravel-bed Rivers*, Thorne, C.R., Bathurst, J.C., Hey, R.D. (eds). John Wiley and Sons Ltd; p269-300.

Ashmore, P., and Parker, G. (1983), 'Confluence scour in coarse braided streams', *Water Resources Res.*, **19**(2), p392-402.

Best, J. L. (1988), 'Sediment transport and bed morphology at river channel confluences.' *Sedimentology*, **35**, p481–498.

Best, J.L., and Reid, I. (1984), 'Separation zone at open channel junctions.' *J. Hydr. Eng.*, **110**(11), p1588-1594.

Best, J.L., and Roy, A.G. (1991) 'Mixing-layer distortion at the confluence of channels of different depth.' *Nature*, **350**, p411–413.

Biron, P., Best, J.L., and Roy, A.G. (1996 a) 'Effects of bed discordance on flow dynamics at river channel confluences.' *Journal of Hydraulic Engineering*, **122**(12), p676–682.

Biron, P., Lane, S.N., Roy, A.G., Bradbrook, K.F., Richards, K.S. (1998) 'Sensitivity of bed shear stress estimated from vertical velocity profiles: the problem of sampling resolution.' *Earth Surf. Processes Landforms*, **23**, p133– 139.

Biron, P., Roy, A.G., and Best, J.L. (1996 b) 'Turbulent flow structure at concordant and discordant open-channel confluences.' *Experiments in Fluids*, **21**, p437–446.

Biron, P.M., Richer, A., Kirkbride, A.D., Roy, A.G., and Han, S. (2002) 'Spatial patterns of water surface topography at a river confluence.' *Earth Surf. Processes Landforms*, **27**, p913– 928.

Biron, P., Roy, A.G., Best, J.L., and Boyer, C.J. (1993) 'Bed morphology and sedimentology at the confluence of unequal depth channels.' *Geomorphology*, **8**, p115–129.

Boyer, C., Roy, A.G., and Best, J.L. (2006) 'Dynamics of a river channel confluence with discordant beds: Flow turbulence, bed-load sediment transport, and bed morphology.' *J. Geophys. Res.*, **111**, F04007, doi:10.1029/2005JF000458.

Bradbrook, K. F., Biron, P., Lane, S.N., Richards, K.S., and Roy, A.G. (1998) 'Investigation of controls on secondary circulation and mixing processes in a simple confluence geometry using a three-dimensional numerical model.' *Hydrol. Processes*, **12**, p1371 – 1396.

Bradbrook, K. F., Lane, S.N., and Richards, K.S. (2000 a) 'Numerical simulation of three-dimensional time-averaged flow structure at river channel confluences.' *Water Resour. Res.*, **36**, p2731 – 2746.

Bradbrook, K. F., Lane, S.N., Richards, K.S., Biron, P.M., and Roy, A.G. (2000 b) 'Large eddy simulation of periodic flow characteristics at river channel confluences.' *J. Hydraul. Res.*, **38**, p207-215.

Bradbrook, K. F., Lane, S.N., Richards, K.S., Biron, P., and Roy, A.G. (2001) 'Role of bed discordance at asymmetrical open-channel confluences.' *J. Hydraul. Eng.*, **127**, p351 – 368.

Bray, D.I., and Davar, K.S. (1987) 'Resistance to flow in gravel-bed rivers.' *Can J Civ. Eng*, **14**, p77-86.

Bridge, J.S., and Gabel, S.L. (1992) 'Flow and sediment dynamics in a low sinuosity, braided river: Calamus River, Nebraska Sandhills.' *Sedimentology*, **39**, p125–142.

Church, M.A. (1987) Discussion of 'Formation of a coarse surface layer as the response to gravel mobility.' In *Sediment Transport in Gravel-bed Rivers*, Thorne, C.R., Bathurst, J.C., Hey, R.D. (eds). John Wiley and Sons Ltd; p314-322.

Church, M. (2001) 'River science and Fraser River: Who controls the river?' *Proceedings Gravel Bed Rivers V, New Zealand Hydrological Society*, p607-631.

Church, M., and Ham, D. (2004) 'Atlas of the alluvial gravel-bed reach of Fraser River in the Lower Mainland, showing channel changes in the period 1928-1999.' Online at http://www.geog.ubc.ca/fraserriver/publications.html.

Church, M., and Weatherly, H. (1998) 'Historical changes of Minto channel during the twentieth century.' Online at http://www.geog.ubc.ca/fraserriver/publications.html.

De Serres, B., Roy, A.G., Biron, P.M., and Best, J.L. (1999) 'Three-dimensional structure of flow at a confluence of river channels with discordant beds.' *Geomorphology*, **26**, p313–335.

Gaeuman, D., and Jacobson, R. B. (2006) 'Acoustic bed velocity and bed-load dynamics in a large sand-bed river.' *J. Geophys. Res.*, 111, F02005.

Gaeuman, D., and Jacobson, R. B. (2007) 'Field Assessment of Alternative Bed-Load Transport Estimators.' *J. Hydraul. Eng.*, 133(12), 1319-1328.

Huang, J., Weber, L.J., and Lai, Y.G. (2002) 'Three-dimensional numerical study of flows in open-channel junctions.' *Journal of Hydraulic Engineering*, **128**(3), p268-280.

Kostaschuk, R., Best, J., Villard, P., Peakall, J., and Franklin, M. (2005) 'Measuring flow velocity and sediment transport with an acoustic Doppler current profiler.' *Geomorphology*, **68**, p25-37.

Lane, S. N., Bradbrook, K.F., Richards, K.S., Biron, P.M., and Roy, A.G. (2000) 'Secondary circulation cells in river channel confluences: Measurement artefacts or coherent flow structures?' *Hydrol. Processes*, **14**, p2047 – 2071.

Lane, S.N., Parsons, D.R., Best, J.L., Orfeo, O., Kostaschuk, R.A., and Hardy, R.J. (2008), 'Causes of rapid mixing at a junction of two large rivers: Rio Parana and Rio Paraguay, Argentina.' *J. Geophysical. Res.*, **113**, F02019, doi:10.1029/2006JF000745.

Mosley, M. P. (1976), 'An experimental study of channel confluences.' *J. Geol.*, **84**, p535–562.

Nezu, I., and Nakagawa, H. (1993). *Turbulence in Open-Channel Flows*, IAHR Monograph Series, A. A. Balkema, Rotterdam.

Parsons, D.R., Best, J.L, Lane, S.N., Orfeo, O., Hardy, R.J., and Kostaschuk, R. (2007) 'Form roughness and the absence of secondary flow in a large confluence-diffluence, Rio Parana, Argentina.' *J. Geophysical Research*, **110**, F04S03, doi:10.1029/2004JF000231.

Parsons, D.R., Best, J.L, Orfeo, O., Hardy, R.J., Kostaschuk, R, and Lane, S.N. (2005) 'Morphology and flow fields of three-dimensional dunes, Rio Parana, Argentina: results from simultaneous multibeam echo sounding and acoustic Doppler current profiling.' *Earth Surf. Processes Landforms*, **32**, 155-162.

Ramooz, R., and Rennie, C. D. (in press). "Laboratory measurement of bed-load with an ADCP," in Bed-load-Surrogate Monitoring, eds. J. Gray and J. Laronne. United States Geological Survey Scientific Investigations Report.

Rennie, C. D., and Church, M. (2007) ' ADCP shear stress and bed-load transport in a large wandering gravel-bed river.' *32nd IAHR Congress*, Venice, 10p.

Rennie, C.D., Church, M. (2010) 'Mapping spatial distributions and uncertainty of water and sediment flux in a large gravel-bed river reach using an aDcp.' *J. Geophysical Research – Earth Surface*, in second review, February 2010.

Rennie, C. D., and Millar, R. G. (2004). "Measurement of the spatial distribution of fluvial bed-load transport velocity in both sand and gravel." *Earth Surf. Processes Landforms*, 29(10), 1173–1193.

Rennie, C. D., and Millar, R. G. (2007). "Deconvolution technique to separate signal from noise in gravel bed-load velocity data." *J Hydraul. Eng.*, 133(8), 845-856.

Rennie, C. D., Millar, R. G., and Church, M. A. (2002). "Measurement of bed-load velocity using an acoustic Doppler current profiler." *J. Hydraul. Eng.*, 128(5), 473–483.

Rennie, C.D., and Rainville, F. (2006) 'Case study of precision of GPS differential correction strategies:Influence on aDcp velocity and discharge estimates.' *J. Hydraulic Engineering (ASCE)*, **132**(3), p225-234.

Rennie, C. D., and Villard, P. V. (2004). "Site specificity of bed-load measurement using an acoustic Doppler current profiler." *J. Geophys. Res., [Earth Surface]*, 109, F03003.

Rhoads, B. L., and Kenworthy, S.T. (1995), 'Flow structure at an asymmetrical stream confluence.' *Geomorphology*, **11**, p273–293.

Rhoads, B. L., and Kenworthy, S.T. (1998), 'Time-averaged flow structure in the central region of a stream confluence.' *Earth Surf. Processes Landforms*, **23**, p171–191.

Rhoads, B. L., and Sukhodolov, A.N. (2001), 'Field investigation of three-dimensional flow structure at stream confluences: 1. Thermal mixing and time-averaged velocities.' *Water Resour. Res.*, **37**, p2393–2410.

Rhoads, B. L., and Sukhodolov, A.N. (2004), 'Spatial and temporal structure of shear layer turbulence at a stream confluence.' *Water Resources Res.*, **40**, W06304, doi:10.1029/2003WR002811.

Roy, A. G., and Bergeron, N. (1990) 'Flow and particle paths at a natural river confluence with coarse bed material.' *Geomorphology*, **3**(2), p99-112.

Roy, A. G., Roy, R. and Bergeron, N. (1988) 'Hydraulic geometry and changes in flow velocity at a river confluence with coarse bed material.' *Earth Surf Process Landforms*, **13**(7), p583-598.

Sukhodolov, A., and Rhoads, B. L. (2001) 'Field investigation of three dimensional flow structure at stream confluences: 2. Turbulence.' *Water Resour. Res.*, **37**, p2411 -2424.

Szupiany, R.N., Amsler, M.L., Best, J.L., and Parsons, D.R. (2007) 'Comparison of fixed- and moving-vessel flow measurements with an aDp in a large river.' *J. Hydraulic Eng.*, **133**(12), p1299-1309.

Szupiany, R.N., Amsler, M.L., Parsons, D.R., and Best, J.L. (2009) 'Morphology, flow structure, and suspended bed sediment transport at two large braid-bar confluences.' *Water Resour. Res.*, **45**, W05415, doi:10.1029/2008WR007428.

Thorne, P. D., Waters, K. R., and Brudner, T. I. (1995). "Acoustic measurements of scattering by objects of irregular shape." *J. Acoust. Soc. Am.*, 97(1), 242-251.

van Rijn, L. C. (1984). "Sediment Transport, Part I: Bed-Load Transport." *J. Hydraul. Eng.*, 110(10), 1431-1456.

Weerakoon, S.B., Kawahana, Y., and Tamai, N. (1991) 'Three dimensional flow structure in channel confluence of rectangular section.' *Proceedings XXIV Congress, International Association for Hydraulic Research*, A373–380.

'Workhorse Commands and Output Data Format' (2002), RD Instruments Acoustic Doppler Solutions, P/N 957-6156-00.